University of Tennessee, Knoxville
TRACE: Tennessee Research and Creative Exchange

Doctoral Dissertations | Graduate School

5-2024

Novel energy scale calibration strategies for the PROSPECT-II experiment

Xiaobin Lu
University of Tennessee, Knoxville, xlu21@vols.utk.edu

Follow this and additional works at: https://trace.tennessee.edu/utk_graddiss

 Part of the Elementary Particles and Fields and String Theory Commons, and the Nuclear Commons

Recommended Citation

Lu, Xiaobin, "Novel energy scale calibration strategies for the PROSPECT-II experiment. " PhD diss., University of Tennessee, 2024.
https://trace.tennessee.edu/utk_graddiss/10072

This Dissertation is brought to you for free and open access by the Graduate School at TRACE: Tennessee Research and Creative Exchange. It has been accepted for inclusion in Doctoral Dissertations by an authorized administrator of TRACE: Tennessee Research and Creative Exchange. For more information, please contact trace@utk.edu.

To the Graduate Council:

I am submitting herewith a dissertation written by Xiaobin Lu entitled "Novel energy scale calibration strategies for the PROSPECT-II experiment." I have examined the final electronic copy of this dissertation for form and content and recommend that it be accepted in partial fulfillment of the requirements for the degree of Doctor of Philosophy, with a major in Physics.

Alfredo Galindo-Uribarri, Major Professor

We have read this dissertation and recommend its acceptance:

Stefan Spanier, Eric Lukosi, AndrewW. Steiner, Soren P. Sorensen

Accepted for the Council:

Dixie L. Thompson

Vice Provost and Dean of the Graduate School

(Original signatures are on file with official student records.)

To the Graduate Council:
I am submitting herewith a thesis written by Xiaobin Lu entitled "Novel energy scale calibration strategies for the PROSPECT-II experiment." I have examined the final paper copy of this thesis for form and content and recommend that it be accepted in partial fulfillment of the requirements for the degree of Doctor of Philosophy, with a major in Physics.

Alfredo Galindo-Uribarri, Major Professor

We have read this thesis
and recommend its acceptance:

Eric D. Lukosi

Soren Sorensen

Stefan Spanier

Andrew W. Steiner

Accepted for the Council:

Dixie L. Thompson
Vice Provost and Dean of the Graduate School

To the Graduate Council:
I am submitting herewith a thesis written by Xiaobin Lu entitled "Novel energy scale calibration strategies for the PROSPECT-II experiment." I have examined the final electronic copy of this thesis for form and content and recommend that it be accepted in partial fulfillment of the requirements for the degree of Doctor of Philosophy, with a major in Physics.

Alfredo Galindo-Uribarri, Major Professor

We have read this thesis
and recommend its acceptance:

Eric D. Lukosi

Soren Sorensen

Stefan Spanier

Andrew W. Steiner

Accepted for the Council:

Dixie L. Thompson

Vice Provost and Dean of the Graduate School

(Original signatures are on file with official student records.)

Novel energy scale calibration strategies for the PROSPECT-II experiment

A Dissertation Presented for the

Doctor of Philosophy

Degree

The University of Tennessee, Knoxville

Xiaobin Lu

May 2024

© by Xiaobin Lu, 2024
All Rights Reserved.

I dedicate all my achievements to my parents who had continuously supported and inspired me.

Acknowledgements

First and foremost, I would like to thank my advisor Alfredo for his guidance on the accomplishment of my graduate work. Not only did he offer great opportunities for my academic work and share his extensive physics knowledge with me, but also he has been a great mentor of my life.

Throughout my graduate life at UTK and ORNL, I would also like to thank Elisa for her help on my early work at ORNL and PROSPECT collaboration, Corey, Blaine, Diego for their roles as both colleagues and friends, Robert Varner for his support on computing needs for my work. I would also like to thank Anne Gladman, Sherry Lamb, Jessica Rose, Chrisanne Romeo for helping me out on administrative matters at UTK and ORNL.

During my academic career, I would like to thank PROSPECT collaborators Tom Lanford, Xianyi Zhang, Pranava Teja Surukuchi, Jeremy Gaison, Danielle Norcini, Ben Foust, Olga Kyzylova for sharing their great skill and knowledge with me. I would also like to thank Bryce Littlejohn, Nathaniel Bowden, Pieter Mumm for their roles as professional researchers and providing academic advice on my research.

Most of all, I owe so much to my parents and brother for supporting my selfish decision to pursuit PhD work abroad. All my work would not exist without your support and love.

Abstract

Nuclear reactors contributed to the first discovery of the elusive neutrino particle and continue to play a significant role in our understanding of neutrino masses and oscillations. The PROSPECT reactor neutrino experiment, the Precision Reactor Oscillation and SPECTrum Experiment, took data at the High Flux Isotope Reactor (HFIR) at Oak Ridge National Laboratory. This work discusses calibration procedures and the establishment of an energy scale model, and details the development of efficient analysis cuts and subsequent selection cut optimization. The precise energy scale calibration and efficient analysis cuts produced a high quality dataset of neutrino interactions of more than 50,000 within a year's data-taking. New limits on the oscillation of sterile neutrinos were set and no statistically significant indication of a potential sterile neutrino was found. The Reactor Antineutrino Anomaly best-fit point was disfavored at 2.5σ confidence level. The high precision ^{235}U neutrino spectrum exhibited a spectral deviation with 2.2σ confidence level around 5 MeV region in comparison to the Huber-Mueller model prediction, and the hypothesis that ^{235}U neutrinos are solely responsible for spectrum discrepancies between model and data obtained at commercial reactor cores was disfavored at 2.4σ confidence level.

Given the success of PROSPECT the collaboration is currently in preparation for an upgraded detector, PROSPECT-II, to further expand the physics goals of the program. The new design optimizes the fiducial volume by elimination of dead space previously occupied by internal calibration channels, which in turn necessitates the

external deployment. In this dissertation we developed a novel external calibration scheme. We evaluated the expected performance of externally deployed calibration sources using PROSPECT-I data and a well-benchmarked simulation package. The proposed external calibration scheme delivers a compatible energy scale model and achieves comparable performance with the inclusion of an additional AmBe neutron source, in comparison to the previous internal arrangement of PROSPECT-I. Most importantly, the estimated uncertainty contribution from the external energy scale calibration model meets the precision requirements of the PROSPECT-II experiment. This work also investigates the application of a DT neutron generator as a complementary method for liquid scintillator calibration.

Table of Contents

1 Thesis outline and my contributions **1**

1.1 Outline 1

1.2 My contributions 2

2 Introduction to neutrino physics **4**

2.1 The hypothesis of the neutrino particle 4

2.2 Discovery of neutrinos 6

2.3 Neutrino mass 7

2.4 Discovery of neutrino oscillations 10

2.5 Neutrino oscillation theory 12

3 Reactors as a source of antineutrinos and related anomalies **16**

3.1 Reactor antineutrino production in nuclear reactors 17

3.2 Reactor antineutrino detection via the Inverse Beta Decay process . . 22

3.3 Reactor antineutrino experiment development 25

3.4 Reactor antineutrino anomaly 26

3.5 Current short baseline antineutrino experiment 31

4 PROSPECT experiment **33**

4.1 HFIR reactor experimental site 33

4.2 Detector design 35

4.2.1 Liquid scintillator 37

4.2.2 Optical grid . . . 38
4.2.3 PMT modules . . . 42
4.2.4 Optical and radioactive calibration systems . . . 45
4.2.5 Detector passive shielding . . . 48
4.2.6 Detector control and monitoring . . . 48
4.2.7 Data acquisition system . . . 50
4.3 Detector construction and commissioning timeline . . . 52

5 Neutrino detection physics and detector calibration 55
5.1 Neutrino detection . . . 56
5.2 Mechanism of liquid scintillation . . . 58
5.3 Low-level calibration . . . 62
5.3.1 PMT timing offset . . . 63
5.3.2 Map PMT timing to z-position along the segment . . . 64
5.3.3 Combined PSD parameter for each segment . . . 64
5.3.4 ADC to energy conversion . . . 67
5.3.5 Low level calibration performance . . . 69
5.3.6 Clustering segment pulses to physics quantities . . . 72
5.4 Detector energy response . . . 72

6 Optimization of neutrino event reconstruction and PROSPECT-I physics results 82
6.1 IBD event selection cuts . . . 83
6.2 IBD cut optimization . . . 87
6.3 IBD prompt energy spectrum and cross-checks . . . 98
6.4 Results from PROSPECT-I and ongoing analysis . . . 108
6.4.1 Modeling HFIR neutrino spectrum . . . 108
6.4.2 Spectrum analysis . . . 110
6.4.3 Oscillation analysis . . . 113
6.4.4 Reactor neutrino anomaly discussion . . . 117

6.4.5 Ongoing and future analysis . . . 119

7 PROSPECT-II program 120

7.1 Physics goals of PROSPECT-II . . . 120

7.2 PROSPECT-II detector . . . 129

8 Alternative energy scale calibration strategy for PROSPECT-II 134

8.1 Setup for external energy calibration . . . 136

8.1.1 Calibration data . . . 138

8.1.2 Parameterization of the energy scale model . . . 141

8.1.3 χ^2-based energy scale model determination . . . 142

8.2 Performance evaluation . . . 145

8.2.1 Energy scale model compatibility . . . 145

8.2.2 Benefits of inclusion of AmBe source . . . 147

8.2.3 Energy scale model systematic uncertainty contribution . . . 151

8.3 Discussion on specific concerns related to the upgrades . . . 152

9 Liquid scintillator calibration using DT generators 162

9.1 Physics of DT neutron generator . . . 164

9.2 Complementary calibration using external DT generators . . . 166

9.3 MC simulation results and future works . . . 168

10 Conclusion 173

Vita 190

Chapter 1

Thesis outline and my contributions

1.1 Outline

Chapter 1 gives an outline of the thesis and states my contributions to the PROSPECT experiment.

Chapter 2 provides an historical overview of neutrino physics in both experimental and theoretical point of view. Neutrino oscillation theory is also described.

Chapter 3 presents a detailed overview of the reactor antineutrino physics, including reactor antineutrino production and detection, current reactor neutrino experiment development and anomalies in the community.

Chapter 4 describes the PROSPECT experiment, including a detailed description of the experimental site and detector component.

Chapter 5 goes over the physics of liquid scintillator, a deep look at the calibration of the detector and overall detector energy response.

Chapter 6 describes the antineutrino event detection via the IBD process and the event selection optimization process. The event selection and the selection optimization leads to the final prompt energy spectrum.

Chapter 7 summarizes the physics results from PROSPECT and outlines ongoing analysis efforts. The PROSPECT-II detector upgrades and the expected physics goals are also described.

Chapter 8 proposes an alternative calibration strategy for the upgraded PROSPECT-II detector. The performance of such external calibration scheme is evaluated. Specific challenges introduced in the new PROSPECT-II detector upgrades are also discussed, such as external source location precision and inter-segment crosstalk.

Chapter 9 proposes a complementary calibration scheme using an external portable neutron DT generator. The benefits of the inclusion of 14 MeV mono-energetic neutron source are described and the characterization of the neutron response of the liquid scintillator is studied using existing PROSPECT simulation packages.

Chapter 10 summarizes and concludes the work of this dissertation.

1.2 My contributions

The PROSPECT experiment was a short baseline reactor-based neutrino experiment designed to make precision measurements of the ^{235}U neutrino energy spectrum and search for sterile neutrino oscillations. The PROSPECT detector operated between March and October in 2018, collecting five reactor-on cycles of neutrino signals and the backgrounds during reactor-off cycles.

I joined the PROSPECT collaboration on my 2nd year of graduate study. Therefore, I was able to get involved in various hardware and data analysis activities as the PROSPECT collaboration was in the early preparation stage for the detector

assembly and commissioning. I also contributed in activities including the detector assembly, operation and calibration campaigns. I also played leading roles in various analyses of the early neutrino dataset. After the detector was disassembled, I actively contributed to the development of an upgraded detector.

I had hands-on experience with photomultiplier tubes (PMT) housing preparation and assembly in a clean room environment. I also contributed testing the PMT base before the detector was assembled and shipped to ORNL. I made UV-Vis measurements of the liquid scintillator used for the PROSPECT program for quality control. I co-led one of the calibration campaigns, which included operations of the calibration motor drive system and handling of the calibration sources. I actively participated in HFIR neutron and gamma background measurements and magnetic field mapping around the PROSPECT detector.

In terms of data analysis, my first major contribution was co-leading the Inverse Beta Decay (IBD) selection optimization analysis, leading to the first neutrino energy spectrum and oscillation physics result in two publications in the journal Physical Review Letters. Later, I was the leading analyzer for selection cuts re-optimization, neutrino energy spectrum generation and validations for the whole PROSPECT dataset in a more detailed paper in Physical Review D. I was the leading analyzer for detector systematics covariance generations for an improved final spectrum analysis of the same dataset, which was just recent accepted for Physical Review Letters publication. Lastly, I worked on developing and validating an external calibration scheme for the upgraded PROSPECT-II detector. I wrote a peer-reviewed paper for the work on behalf of the collaboration that was published on Journal of Instrumentation [1].

Chapter 2

Introduction to neutrino physics

In this chapter, I briefly introduce the neutrino particle, from the postulation of the elusive particle to the recent development of neutrino flavor oscillation phenomenon. I give an overview of the experimental efforts leading to the neutrino oscillation discovery, and also briefly describe the theoretical framework of the neutrino oscillation.

2.1 The hypothesis of the neutrino particle

The birth of the neutrino particle originated from the early studies of β decay of nuclei. The β decay at the time was commonly believed to be a two-body reaction. The β emitted from the decay was believed to be mono-energetic under the conservation law of energy and momentum. However, this contradicted the smooth and continuous spectrum observed in Chadwick's experiment in 1914 [2], instead of the expected distinctive discrete energy lines in the spectrum. This was further confirmed by Ellis and Wooster's spectrum measurement of ^{210}Bi [3] in 1927, as shown in Figure 2.1.

To preserve the energy and momentum conservation law, Niels Bohr proposed that the conservation law holds only in a statistical sense to explain the observed continuous β radiation energy spectrum. Meanwhile, Pauli proposed a new hypothetical particle in the β decay process to save the conservation law.

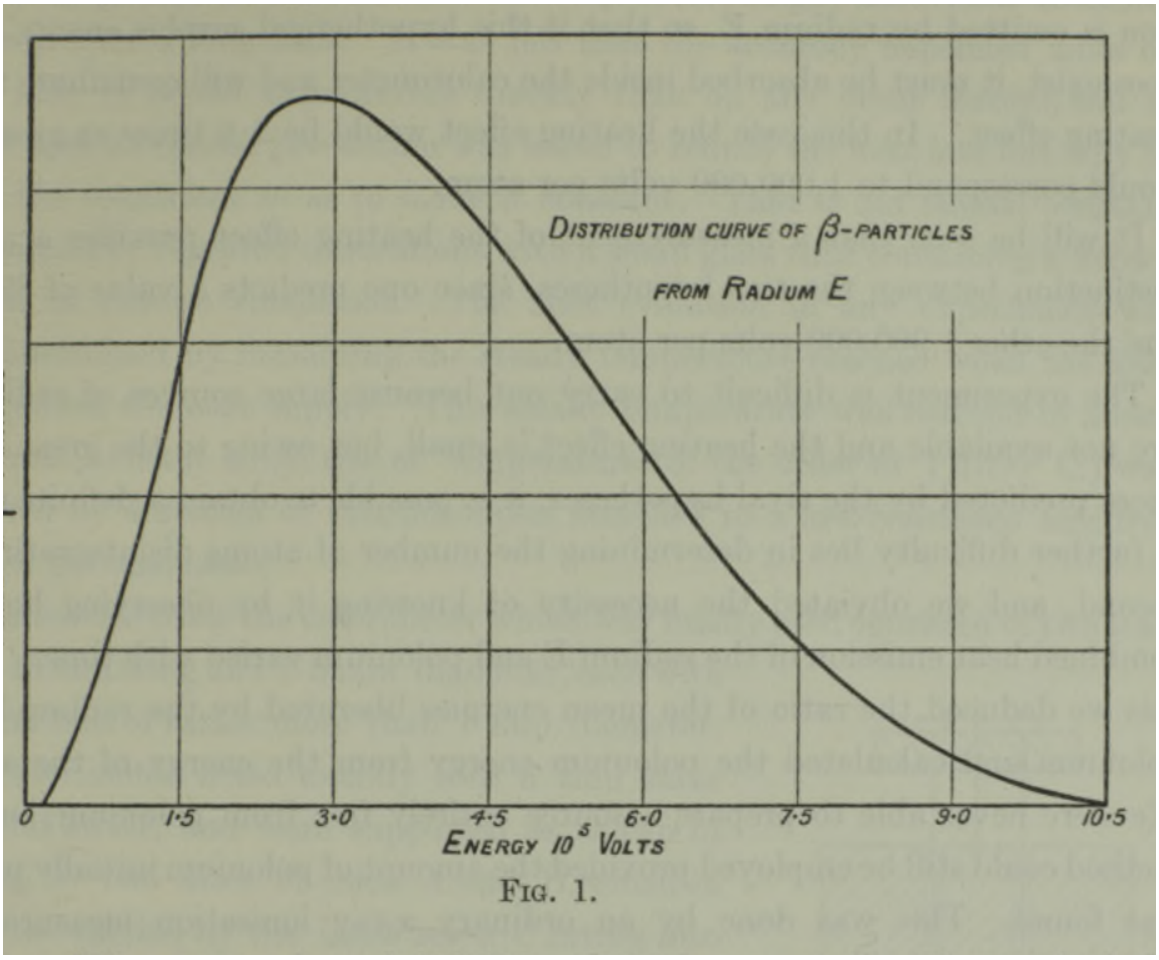


Figure 2.1: β spectral measurement of the Radium-E(^{210}Bi) by Ellis and Wooster in 1927. Source: [3]

At the time it was called a "neutron" but later renamed to neutrino ("the little neutral one" in Italian) by Fermi [4]. The introduction of this additional electrically neutral particle in the β decay process conserved the energy and momentum of the three-body decay process among the recoiling nucleus, the electron and the neutrino,

$$n \to p + e^- + \bar{\nu}_e. \tag{2.1}$$

In the theoretical framework of Fermi's beta decay theory, the neutrino (later found to be electron antineutrino $\bar{\nu}_e$) is an electrical neutral and massless spin 1/2 particle. When Pauli postulated the particle, he called the neutrino "a particle that cannot be detected". The search of such particles took almost twenty years since the its postulation.

2.2 Discovery of neutrinos

The first direct proof of the existence of neutrino particles was via the so-called Inverse Beta Decay (IBD) process,

$$\bar{\nu}_e + p \to e^+ + n. \tag{2.2}$$

The detected neutrino particle is the electron antineutrino $\bar{\nu}_e$, the antiparticle of one of the three neutrino flavors as we know now.

The cross-section of the inverse beta decay interaction was estimated to be extremely small, on the order of $\mathcal{O}(10^{-44}\text{cm}^2)$ [5]. To detect such rare events with sufficient statistics, either enormous amount of neutrinos or large target proton density in the detector was required, or both. Before the first direct neutrino detection experiment, now also known as the Cowan–Reines experiment, Cowan and Reines proposed neutrino detection from a nuclear weapon test explosion, which was surprisingly granted approval by the Los Alamos National Laboratory director Norris Bradbury. However, the propose never took place. Later, the idea of using neutrinos from nuclear reactors, i.e. from the beta decays of fission daughter isotopes at the

Savannah River reactor was reviewed by Cowan and Reines as an alternative feasible way that provides better background shielding, longer and consistent measurements. The detector consisted of two target tanks filled with water, and sandwiched between three large scintillation detectors, as shown in Figure 2.2. The water in the target tanks provided protons for the inverse beta decay reaction, and cadmium chloride dissolved in the water provided targets for neutron capture. The sandwich configured detector, in the case of a neutrino-induced event, would produce two pairs of event pulses separated about 3 to 10 microseconds. The first pair of the event pulse came from the positron annihilation and the second pair from the neutron capture. The detector was located in a small basement in the reactor building with about 12 meters of overburden against cosmic ray induced neutron and gamma background, and about 11 meters of concrete as a shield against reactor related neutrons. Cowan and Reines reported a cross section of $(12^{+7}_{-4}) \times 10^{-44}\text{cm}^2$ in [6] in 1960, in agreement with predictions, thus confirming the existence of neutrinos.

The Cowan-Reines experiment was awarded the Nobel prize in 1995 almost forty years later for their discovery of the neutrino, or more specifically the electron antineutrino. The second flavor of neutrino, the muon neutrino, was discovered in 1962 by Leon Lederman, Melvin Schwartz and Jack Steinberger in an experiment [7] at the Brookhaven National Laboratory, earning them the Nobel prize in 1988. The last flavor of neutrino, the tau neutrino, was discovered in the DONUT experiment [8] from Fermilab, which was built during the 1990s to specifically detect the tau neutrino.

2.3 Neutrino mass

The Standard Model (SM) is the fundamental framework that describes the nature of three elemental interactions in the universe: electromagnetic, weak and strong forces. The framework has proven to be one of the successful theoretical tools in particle physics. The framework assumes neutrinos are neutral fermions with spin 1/2. There are three neutrino flavors and each corresponds to one of the three charged leptons

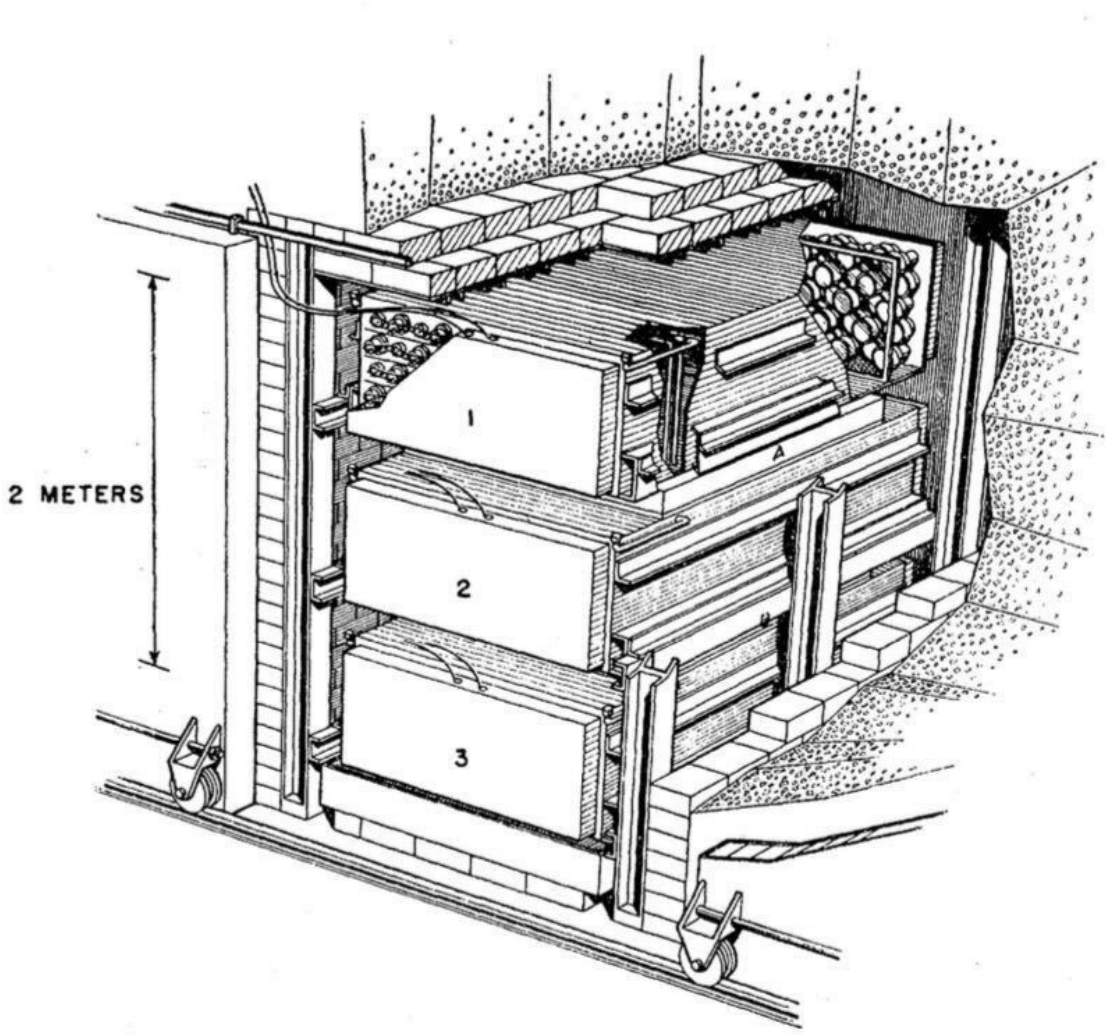


Figure 2.2: Schematic of the neutrino detector in Cowan–Reines neutrino experiment. A and B are plastic tanks filled with water for the inverse beta decay interaction. They are sandwiched by three scintillation detectors (labeled as 1, 2 and 3), each containing liquid scintillator and photomultiplier tubes (PMTs) on both ends. Source:[6]

$(\nu_e, \nu_\mu, \nu_\tau)$. These fermions can be described by the Dirac equation,

$$(i\partial\!\!\!/ - m)\psi(x) = 0 \tag{2.3}$$

where $\psi(x)$ is a 4-component spinor field consisting of both right- and left-chiral field ψ_R and ψ_L. In the SM, neutrinos are always left-handed (left chirality) and antineutrinos are always right-handed (right chirality), causing the neutrino mass term to vanish.

Despite the success of the SM, the observation of neutrino flavor oscillation [9, 10], indicating non-vanishing neutrino masses, opens windows for new physics (NP) beyond the Standard Model (BSM). One straightforward way to add mass to neutrinos is the introduction of right-handed neutrinos, by coupling with the left-handed neutrinos via the Dirac mass term in the Lagrangian,

$$\mathcal{L} = -m_D(\bar{\nu}_L\nu_R + \bar{\nu}_R\nu_L) \tag{2.4}$$

via Yukawa coupling to the Higgs field, similar to how other fermions obtain mass. Similarly, a Majorana (particle and antiparticle are the same) mass term is allowed as well,

$$\mathcal{L} = -\frac{1}{2}m_M(\bar{\nu}^c_L\nu_L + \bar{\nu}^c_R\nu_R) \tag{2.5}$$

where $\nu^c_L = C\bar{\psi}^T_R$ and C represents the charge conjugation operator. The right-handed neutrinos and Majorana neutrinos are not theoretically forbidden, thus a more general Lagrangian can be expressed in the matrix form,

$$\mathcal{L} \sim \begin{pmatrix} \bar{\nu}^c_L & \bar{\nu}^c_R \end{pmatrix} \begin{pmatrix} m_L & m_D \\ m_D & m_R \end{pmatrix} \begin{pmatrix} \nu_L \\ \nu_R \end{pmatrix} \tag{2.6}$$

where $m_L(m_R)$ is the left-(right-) handed Majorana mass, respectively, and m_D is the Dirac mass. In the limit of $m_L = 0$ and $m_D \ll m_R$, the eigenvalues of the mass

matrix are approximately,

$$m_1 = \frac{m_D^2}{m_R} \tag{2.7}$$

$$m_2 = m_R \tag{2.8}$$

where m_1 can represent the left-handed light neutrinos, and m_2 represents the counterpart heavy right-handed sterile neutrinos, which are yet to be observed. This method is commonly described as the type-I see-saw mechanism [11]. Neutrinoless double beta decay is an experimentally proposed hypothetical process that, if observed, would indicate the Majorana nature of the neutrino particle and set limits on the absolute scale of neutrino masses and the mass hierarchy [12, 13].

2.4 Discovery of neutrino oscillations

The study of neutrino oscillations started with the solar neutrino anomaly. The solar neutrino anomaly was first reported by the Homestake experiment [14], where the observed electron neutrino rates were only about 1/3 of what the standard solar model predicted. The Homestake experiment measured the electron neutrinos coming from nuclear fusion reactions in the Sun, mainly the proton-proton chain reactions, via the radiochemical reaction $^{37}\mathrm{Cl}(\nu_e,e^-)^{37}\mathrm{Ar}$. More solar neutrino flux experiments, such as GALLEX [15], SAGE [16], and Kamiokande [17] confirmed fewer detected solar neutrino events than expected. Atmospheric neutrinos from the decays from mesons produced by interactions of the cosmic rays with Earth's atmosphere also showed a deficit in measured rates compared to the model, as reported by experiments from Kamiokande [18] and IMB [19]. The deficit in detected atmospheric muon neutrino was often referred as the atmospheric neutrino anomaly.

The confirmation of neutrino oscillation was first observed by the Super-Kamiokande experiment [9] in 1998. In the experiment, no disagreement was found for electron-like events, while muon-like events saw oscillation patterns into the third

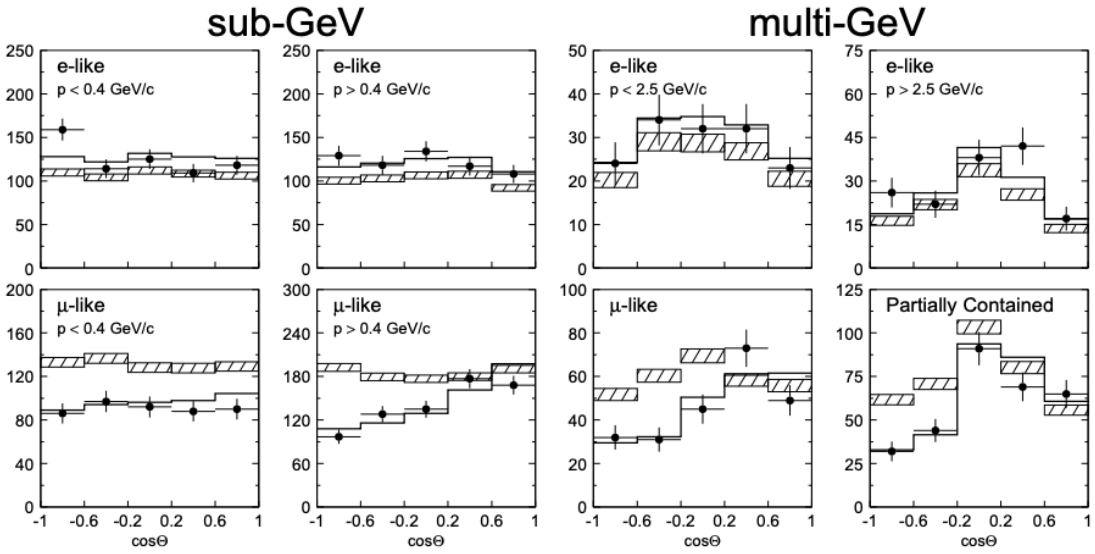


Figure 2.3: Super-Kamiokande event distribution (black dots) for sub-GeV and multi-GeV category as a function of $\cos\theta$. $\cos\theta = -1$ represents upward-going events and $\cos\theta = 1$ represents downward-going events. Electron-like events in the top panel showed agreement with the MC expectation (shaded areas). However, muon-like events deviated from the non-oscillated MC simulations (shaded regions) and can be best-fitted for $\nu_\mu \leftrightarrow \nu_\tau$ as highlighted in solid lines. Source:[9]

flavor, as illustrated in Figure 2.3. The Sudbury Neutrino Observatory (SNO) experiment [10] expanded the detection channel to include elastic scattering (ES), neutral current (NC), and charged current (CC) to measure the flux of all neutrino flavors.

The solar and atmospheric neutrino anomaly led to the discovery of neutrino oscillations and earned both Super-K and SNO collaborations Nobel prize in 2015 "for the discovery of neutrino oscillations, which shows that neutrinos have mass".

2.5 Neutrino oscillation theory

The neutrino oscillation theory was originally inspired by the kaon-antikaon oscillations. Later around the time when muon neutrinos were discovered, the neutrino flavor mixing emerged in a paper written by Maki, Nakagawa and Sakata [20], and was presented in modern formalism by Gribov and Pontecorvo [21] in 1969. The mixing of neutrino flavors can be described by the Pontecorvo–Maki–Nakagawa–Sakata matrix U (also called the PMNS matrix), analogous to the Cabibbo–Kobayashi–Maskawa (CKM) matrix describing the mixing of quarks. The unitary transformation matrix U connects the neutrino flavor states to the mass eigenstates.

$$\begin{pmatrix} \nu_e \\ \nu_\mu \\ \nu_\tau \end{pmatrix} = U \begin{pmatrix} \nu_1 \\ \nu_2 \\ \nu_3 \end{pmatrix} = \begin{pmatrix} U_{e1} & U_{e2} & U_{e3} \\ U_{\mu 1} & U_{\mu 2} & U_{\mu 3} \\ U_{\tau 1} & U_{\tau 2} & U_{\tau 3} \end{pmatrix} \begin{pmatrix} \nu_1 \\ \nu_2 \\ \nu_3 \end{pmatrix} \tag{2.9}$$

The unitary PMNS matrix satisfies unitary relations $U^\dagger U = UU^\dagger = 1$. The PMNS matrix can also be expressed as the product of three independent rotations along the angles θ_{23}, θ_{13}, and θ_{12} without loss of generality.

$$U = \begin{pmatrix} 1 & 0 & 0 \\ 0 & c_{23} & s_{23} \\ 0 & -s_{23} & c_{23} \end{pmatrix} \begin{pmatrix} c_{13} & 0 & s_{13}e^{-i\delta_{\mathrm{CP}}} \\ 0 & 1 & 0 \\ -s_{13}e^{i\delta_{\mathrm{CP}}} & 0 & c_{13} \end{pmatrix} \begin{pmatrix} c_{12} & s_{12} & 0 \\ -s_{12} & c_{12} & 0 \\ 0 & 0 & 1 \end{pmatrix} P \tag{2.10}$$

where $c_{ij} = \cos\theta_{ij}$, $s_{ij} = \sin\theta_{ij}$, and P is a unit matrix in the case of Dirac particles or a diagonal form the two phases in the case of Majorana particles, $\theta_{ij} \in [0, \pi/2]$ and $\delta_{\mathrm{CP}} \in [0.2\pi[$.

Quantum mechanical oscillations of the neutrino flavor state can be calculated by starting with the initial state

$$|\nu(t=0)\rangle = |\nu_\alpha\rangle = \sum_i U^*_{\alpha i}|\nu_i\rangle \tag{2.11}$$

The oscillated neutrino states at time t follow the time-dependent Schrödinger equation,

$$|\nu(t)\rangle = \sum_i U^*_{\alpha i} e^{-iE_i t}|\nu_i\rangle \tag{2.12}$$

where $E_i = \sqrt{p^2 + m_i^2}$. The oscillation probability thus can be expressed as,

$$P(\nu_\alpha \to \nu_\beta) = |\langle\nu_\beta|\nu(t)\rangle|^2 = |\sum_i U_{\beta i} U^*_{\alpha i} e^{-iE_i t}|^2 \tag{2.13}$$

By approximating $E_i = \sqrt{p^2 + m_i^2} \simeq p + m_i^2/(2E)$, the neutrino oscillation probability is,

$$\begin{aligned} P(\nu_\alpha \to \nu_\beta) = \delta_{\alpha\beta} &- 4\sum_{i<j} \mathrm{Re}[U_{\alpha i} U^*_{\beta i} U^*_{\alpha j} U_{\beta j}] \sin^2\left(\frac{\Delta m^2_{ji} L}{4E}\right) \\ &+ 2\sum_{i<j} \mathrm{Im}[U_{\alpha i} U^*_{\beta i} U^*_{\alpha j} U_{\beta j}] \sin\left(\frac{\Delta m^2_{ji} L}{2E}\right) \end{aligned} \tag{2.14}$$

where $\Delta m^2_{ji} = m_j^2 - m_i^2$ and $L \simeq ct$ is the distance the neutrino travelled. This oscillation probability only depends on θ_{23}, θ_{13}, θ_{12}, and, without loss of generality, two independent mass squared differences. The common chosen ones are Δm^2_{21} and Δm^2_{31}, which are usually called mass splittings. Also the oscillation depends on the Dirac CP phase δ_{CP}, not on the Majorana phases. In the case of a simple two neutrino

oscillation case, the probability can be simplified as,

$$P(\nu_\alpha \to \nu_\beta) = \sin^2 2\theta \sin^2 \left(\frac{\Delta m^2 L}{4E} \right) \tag{2.15}$$

where $\alpha \neq \beta$. The determination of the mixing parameters of the neutrino oscillation was performed by experiments from combinations of nuclear reactors, the Sun, atmosphere, and accelerators. The accepted measured values of the mixing parameters [22] are summarized in Table 2.1.

Hypothetical sterile neutrinos, which only interact with other particles via gravity, were proposed to explain the flux anomaly in reactor neutrino experiments. In this case of searches for such sterile neutrinos with mass splitting Δm^2_{41} and mixing angle θ_{14} in reactor experiments, the electron antineutrino survival probability reads,

$$P(\overline{\nu}_e \to \overline{\nu}_e) = 1 - \sin^2 2\theta_{14} \sin^2 \left(1.27 \frac{\Delta m^2_{41}[\mathrm{eV}^2] L[\mathrm{m}]}{E[\mathrm{MeV}]} \right) \tag{2.16}$$

The term $\sin^2 2\theta_{14}$ represents the oscillation magnitude and the ratio of the mass splitting Δm^2_{41} over the neutrino energy is closely related to the oscillation frequency, thus making the baseline sensitive to specific ranges. For example, in order to probe high mass splitting sterile neutrinos, very short baseline neutrino experiments with point-like reactor cores, such as PROSPECT [23] and STEREO [24], would have high sensitivities.

Table 2.1: Best-fit oscillation parameters according to 2022 Particle Data Group neutrino review [22]. NO stands for normal ordering and refers to $m_3 > m_2 > m_1$, while IO stand for inverted ordering and refers to $m_3 < m_1 < m_2$.

Parameter	**Value**	**Source**
$\Delta m^2_{21}(10^{-5}\text{eV}^2)$	7.53	solar
$\Delta m^2_{32}(10^{-3}\text{eV}^2)$(NO)	2.453	atmospheric
$\Delta m^2_{32}(10^{-3}\text{eV}^2)$(IO)	-2.536	atmospheric
$\sin^2\theta_{12}$	0.307	solar + reactor + accelerator
$\sin^2\theta_{23}$ (NO)	0.546	atmospheric
$\sin^2\theta_{23}$ (IO)	0.539	atmospheric
$\sin^2\theta_{13}$	0.0220	reactor

Chapter 3

Reactors as a source of antineutrinos and related anomalies

Reactor is one of the abundant neutrino sources either man-made or natural, and has played a crucial role in the development of our understanding of neutrino physics. The other four sources of neutrinos are:

- atmospheric neutrinos (ν_e, ν_μ, $\bar{\nu}_\mu$, and $\bar{\nu}_e$) from the decays of mesons produced by interactions of cosmic rays with atmosphere
- solar neutrinos (ν_e) from the nuclear fusions in the Sun
- supernova neutrinos (all flavors)
- accelerator neutrinos (ν_e, ν_μ, $\bar{\nu}_\mu$, and $\bar{\nu}_e$) from the decays of mesons produced from proton beams

The reactor neutrinos are of particular interest to us, because they are almost purely electron antineutrinos $\overline{\nu}_e$ with energy up to $\sim$ 10 MeV and have controllable large flux based on the location of the detector. The common detection method of reactor

neutrinos, namely the IBD reaction described previously, is well understood and thus allows for precision measurements.

3.1 Reactor antineutrino production in nuclear reactors

Nuclear reactors are typically in the form of either commercial nuclear power plants for electricity generation or relatively small size reactors mainly used for research, material testing or production of radioisotopes for industry. Nuclear reactions are driven by neutron-induced fission chain reaction of uranium and plutonium isotopes in a controlled way, in which a neutron rich nucleus splits into two or more smaller nuclei along with more subsequent neutrons inducing the chain reaction. For example, the average number of emitted neutrons is about 2.4 for each ^{235}U fission, and only one neutron on average will induce a new chain reaction in a controlled nuclear reactor. The smaller nuclei produced in the fission are mostly unstable and will subsequently beta decay into stable isotopes, producing pure electron antineutrinos. Typically, nuclear reactor emits about $\sim 6 \times 10^{20} \bar{\nu}_e/\mathrm{GW}_{\mathrm{thermal}}$, with essentially no mixing from other flavors of neutrinos.

The fuel used in commercial nuclear power plants, mostly low-enriched uranium (LEU) reactors, consists of mixtures of the actinides ^{235}U (3-5% concentration), ^{238}U, ^{239}Pu, ^{241}Pu. In research nuclear reactors, highly enriched uranium (HEU) fuel (>20% ^{235}U concentration) is used and ^{235}U fission is the dominant process. Fissions of ^{235}U, ^{239}Pu, and ^{241}Pu are induced by thermal neutrons with $\sim$ 0.025 eV kinetic energies. Fissions of ^{238}U can only be induced by fast neutrons ($\sim$1 MeV kinetic energy). The average number of emitted neutrons from these four main fissile isotopes are 2.88, 2.95, and 2.82 for ^{239}Pu, ^{241}Pu, and ^{238}U, respectively. The reactor neutrinos produced in the nuclear reactors are mainly from the beta decays of unstable fission daughters of these four isotopes. The total expected $\overline{\nu}_e$ spectrum is then obtained by adding the

neutrino spectrum originated from each contributing actinides,

$$S(E_\nu) = \sum_i \frac{\mathrm{W_{th}}}{(f_i/F)e_i} \frac{f_i}{F} \left(\frac{dN_i}{dE_\nu}\right) \tag{3.1}$$

where $\mathrm{W_{th}}$ represents the thermal power of the reactor, (f_i/F) is the fission fraction of each actinide i, dN_i/dE_ν is the $\overline{\nu}_e$ spectrum of i's daughter isotope, and e_i is the effective energy of the fission process. The expected $\overline{\nu}_e$ energy spectra are shown below in Figure 3.1. The thermal power of the nuclear reactor can be estimated from reactor heat generation, which typically can be measured from the temperature of the coolant flow [25]. The fission fraction is dynamic and depends on the operation status of the reactor. For example, in a LEU commercial power reactor, the typical values of the fission fraction on average are approximately 58%, 29%, 8%, and 5% for ^{235}U, ^{238}U, ^{239}Pu, and ^{241}Pu, respectively.

There are two primary approaches for calculating the spectrum and flux of reactor neutrinos. The first approach, *ab initio* approach, calculates the spectrum by breaking down dN_i/dE_ν as following,

$$\frac{dN_i}{dE_\nu} = \sum_n Y_n(t) \Big(\sum_j b_{n,j} P(dE_\nu, E_0^{n,j}) \Big) \tag{3.2}$$

where $Y_n(t)$ is the cumulative fission yield at time t for the fission product nucleus n, $b_{n,j}$ is the branching ratio of beta-decay branch i with energy point $E_0^{n,j}$, and $P(dE_\nu, E_0^{n,j})$ is the energy spectra of each beta decay. Despite being straightforward, this method faces several challenges that lead to large uncertainties in the predicted spectrum and flux. These challenges are primary due to the input of the method, i.e. the commonly used experimental nuclear database for fission yields ENDF/B-VIII.0 [26], branching ratios, and the endpoint energies of the beta decay provided in ENSDF [27]. In general, this method would yield a relative uncertainty about 10-20% in the antineutrino energy spectrum. The second method takes advantage of the energy conservation of the beta decay and converts electron spectra from the

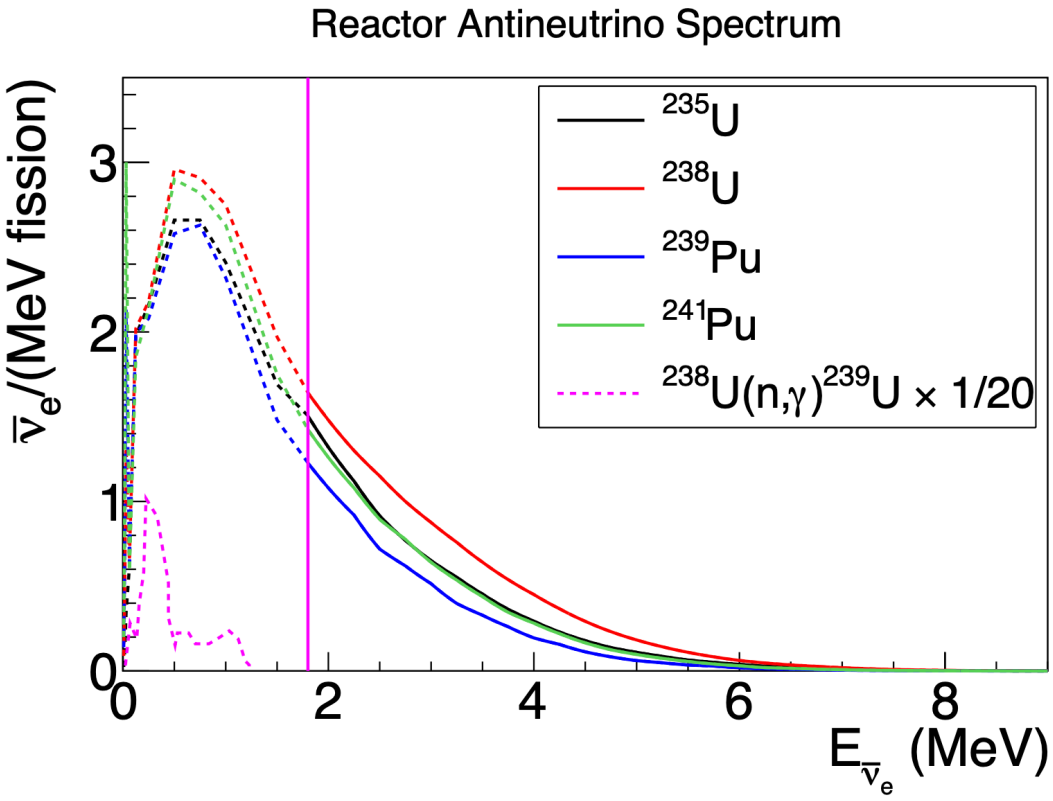


Figure 3.1: Neutrino energy distributions from the main four fissile isotopes, ^{235}U, ^{238}U, ^{239}Pu, ^{241}Pu. The vertical pink line represents the energy threshold of IBD detection. The antineutrino spectrum from fissions induced by fast neutron captures on ^{238}U are below the IBD energy threshold and scaled by a factor of 20, which is not interesting from a IBD detection perspective. Source:[28]

four main fission isotopes to neutrino spectra. The electron spectra of the thermal neutron induced fission of ^{235}U, ^{239}Pu, and ^{241}Pu have been measured at the Institut Laue–Langevin (ILL) research reactor in Grenoble, France [29, 30, 31]. The electron energy spectrum associated with fast neutron induced fission of ^{238}U has been measured in Garching, Germany [32]. Since the electron and the antineutrino share the total energy of the each beta decay branch, the antineutrino spectrum can be calculated from the measured electron spectra by converting the kinematics of the reaction and ignoring the negligible nuclear recoil energy. The conversion process involves fittings of a set of virtual hypothetical beta decay branches to the measured beta spectrum, illustrated in Figure 3.2.

The best-fit virtual branching ratios are then used to convert each virtual beta decay branch to antineutrino spectrum to get the final aggregate neutrino spectrum. The conversion method seems to trivialize the complicated contributions from the nuclear database in *ab initio* method. However, in addition to the uncertainties with the electron spectrum measurements, the conversion method has its own complications such as its dependence on forbidden transitions, uncertainties from the spectrum shape, and beta decay related correction like radiative correction, weak magnetism, and finite nuclear size. With the inclusion of first forbidden beta decays, the uncertainties of the flux can be around $\sim 5\%$ [33].

Current predictions of the antineutrino spectrum for modern LEU fueled reactor neutrino experiments are produced via the so-called Huber-Mueller model, which consisted of the conversion method by Huber [34] and Mueller's ^{238}U spectrum [35] based on *ab initio* method. The estimated uncertainty on the flux is about $\sim 2\%$. For HEU fueled reactor spectrum predictions, which don't need to account for the all fission isotopes except ^{235}U, Huber HEU ^{235}U model is often used as the reference model.

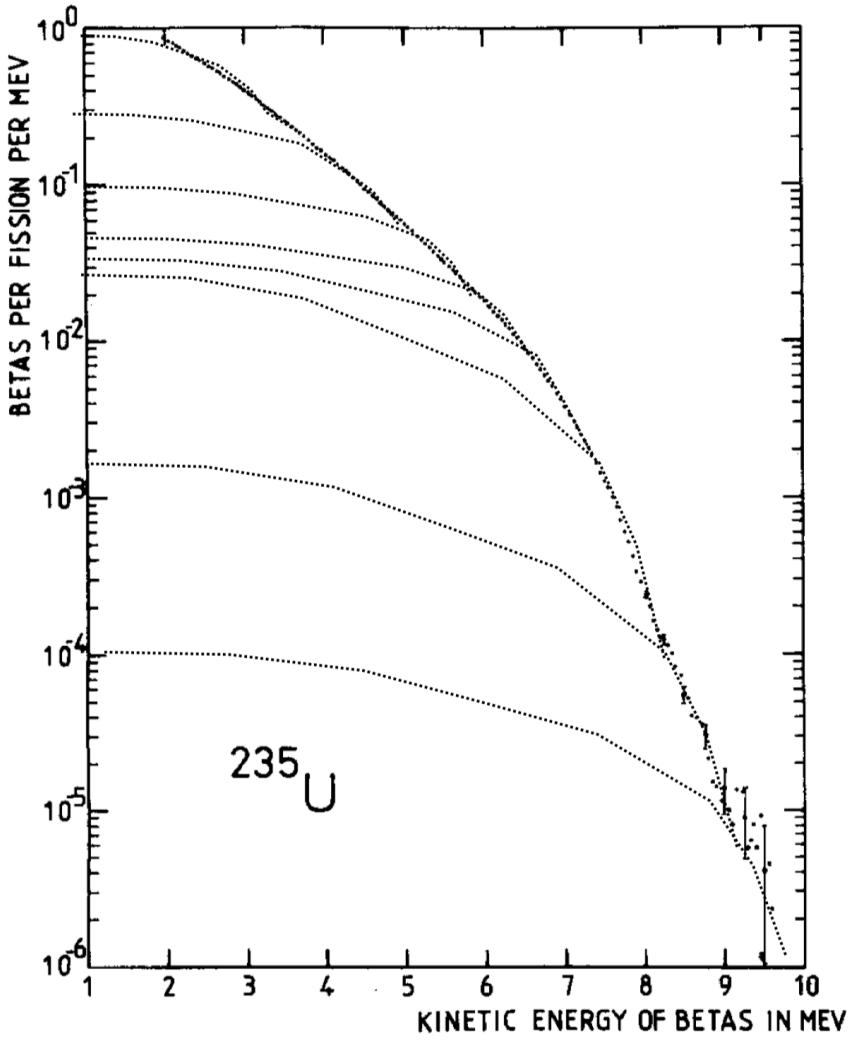


Figure 3.2: Illustration of virtual beta decay branch fitting for ^{235}U beta spectrum, reported from [30]. The dotted lines are the fitted virtual beta branches for the final conversion of the neutrino spectrum.

3.2 Reactor antineutrino detection via the Inverse Beta Decay process

The reactor neutrinos from the nuclear fission reactors, either the commercial LEU reactors or research based HEU fueled reactors, are electron-type antineutrinos. The commonly used detection method is the inverse beta decay reaction (IBD), as used in the Cowan-Reines experiment described in Chapter 2. The IBD reaction, described by the equation below and Feynman diagram in Figure 3.3,

$$\overline{\nu}_e + p \rightarrow e^+ + n, \tag{3.3}$$

features a pair of space- and temporal- correlated positron and neutron, in which the positron carries most of the incident neutrino energy and the neutron provides a handle for distinguishing the signal from the backgrounds. The energy threshold for the IBD reaction to happen can be calculated via the energy conservation as follows,

$$E_\nu > m_n + m_e - m_p \simeq 1.806 \text{ MeV} \tag{3.4}$$

which corresponds to the vertical line outlined in Figure 3.1. The cross section of the IBD interaction is expressed as a function of the energy of incident neutrino, and in the zeroth order [36] is approximately as follows,

$$\sigma_{\text{IBD}} \simeq \frac{2\pi^2/m_e^5}{f_{p.s}^{\text{R}}\tau_n} E_e^{(0)} p_e^{(0)} \tag{3.5}$$

where m_e is the electron mass, $f_{p.s}^{\text{R}} = 1.7152$ represents the phase space factor (including the Coulomb, weak magnetism, recoil, and outer radiative corrections), τ_n is the measured neutron lifetime. The final antineutrino spectrum detected in a IBD-based detector is a combination of the IBD cross section and the neutrino flux and typically resembles what is shown in Figure 3.4.

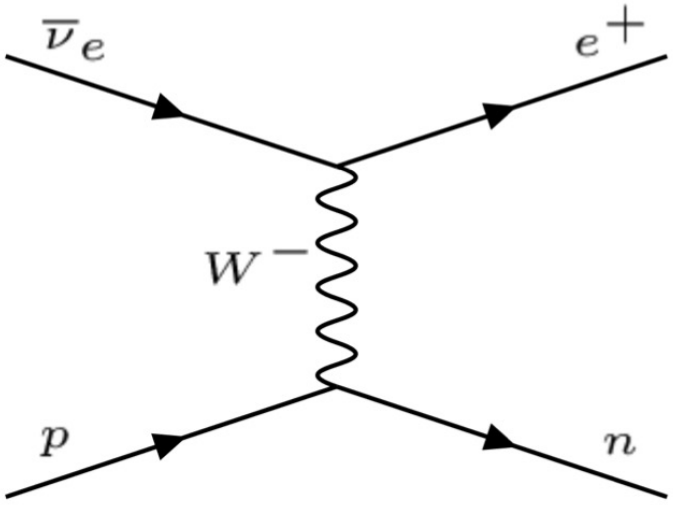


Figure 3.3: Feynman diagram of the Inverse Beta Decay process

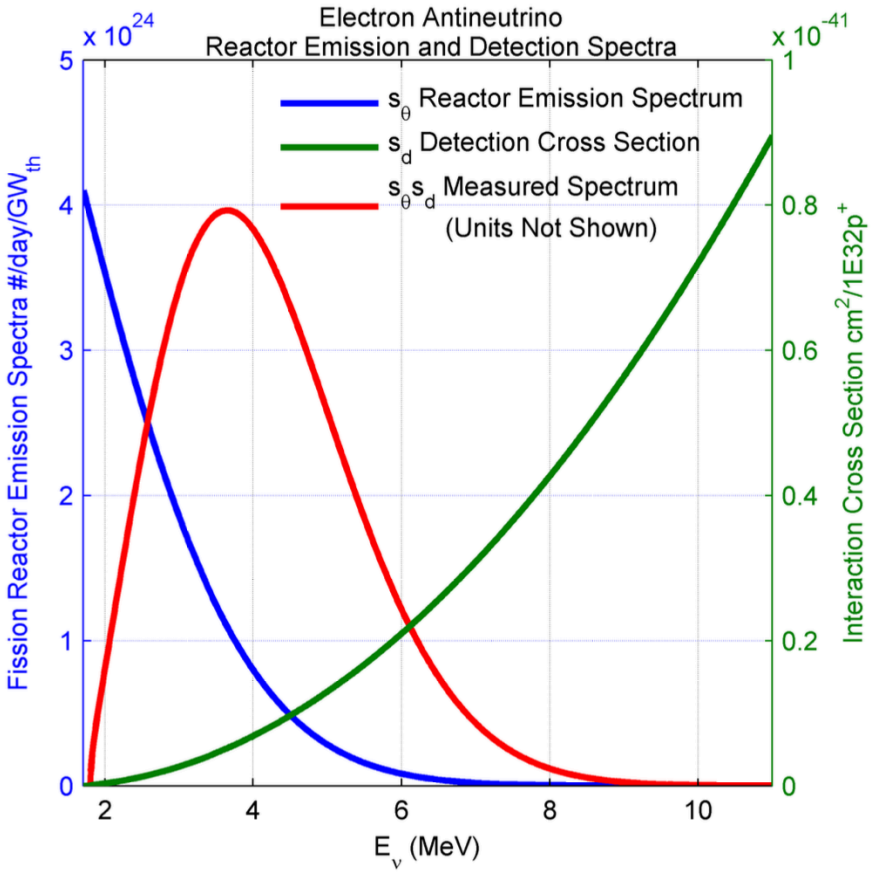


Figure 3.4: Illustration of a typical reactor neutrino spectrum using detector techniques based on the IBD interaction. Note the neutrino energy starts from the IBD threshold described in Equation 3.4. Source:[37]

3.3 Reactor antineutrino experiment development

Since the first detection of $\overline{\nu}_e$ at reactor conducted by Cowan and Reines, the reactor neutrino physics studies mainstreamed the detection method that utilizes the correlation of prompt and delayed events, i.e. neutrino detection via the IBD reaction. More reactor neutrino detection methods were studied using heavy water (D_2O) via the charged current (CC, Equation 3.6) and neutral current (NC, Equation 3.7),

$$\overline{\nu}_e + d \rightarrow n + n + e^+ \tag{3.6}$$

$$\overline{\nu}_e + d \rightarrow n + p + \overline{\nu}_e \tag{3.7}$$

The observed ratio of the CC and NC event rates falls short of the prediction, leading to possible antineutrino oscillation into other flavors at a mass splitting level of order of eV^2 [38].

After the hints of antineutrino oscillation at high mass splitting region, several experiments were performed to look for such signatures. The search for high neutrino mass splitting requires short baselines from the reactor core and involves either comparing measured spectrum to the prediction or relative comparisons at different baselines. The ILL experiment [39] reported null two neutrino oscillation result, ruling out the high mass splitting suggested by Reines. Further experiments like Bugey [40, 41], Goesgen [42, 43, 44], Rovno [45, 46, 47], and Krasnoyarsk [48] all confirmed the null oscillation results. In the late 1980s, underground detectors such as Kamiokande [49, 50] and Super-Kamiokande [9] had reported hints of neutrino oscillation of primarily electron and muon neutrinos, originating from decays of mesons produced in Earth's atmosphere. These results pushed forward reactor experiments at long baselines ($\sim$ 1km), enabling high precision investigation of $\overline{\nu}_e \rightarrow \bar{\nu}_x$ neutrino oscillations. The Chooz [51, 52, 53] and Palo Verde [54, 55, 56] experiment, although found no evidence of neutrino oscillation, excluded the possibilities of interpreting the atmospheric neutrino anomaly by $\nu_\mu \leftrightarrow \nu_e$ oscillations. The

atmospheric neutrino anomaly is the observation of a ν_μ/ν_e ratio being half of the expected, due to either oscillation of $\nu_\mu \leftrightarrow \nu_\tau$ or $\nu_\mu \leftrightarrow \nu_e$. The former oscillation channel, $\nu_\mu \leftrightarrow \nu_\tau$, is favored by Super-Kamiokande [9]. These oscillation experiments indicated a very small value for the mixing angle θ_{13}. In 2002, the Kamioka Liquid Scintillator Anti-Neutrino Detector (KamLAND) observed fewer $\overline{\nu}_e$ events than expected at the 99.95% CL [57],

$$\frac{N_{\text{obs}}}{N_{\text{expected}}} = 0.611 \pm 0.085(\text{stat}) \pm 0.041(\text{syst}) \tag{3.8}$$

Around 2006, several world-class reactor neutrino experiments, including Daya Bay [58], Double CHOOZ [59], and RENO [60], were proposed to measure θ_{13} with high precision. As one of the mixing angles describing neutrino oscillations, θ_{13} is also relevant to the CP violation in the neutrino sector. Despite being the smallest mixing angles, θ_{13} is the most precisely measured to date. The discovery of non-zero θ_{13} also inspired further exploration in neutrino physics using reactor neutrinos, such as searches for sterile neutrinos and neutrino mass hierarchy.

To summarize, the confirmation of the neutrino particle in Cowan-Reines experiment motivated a global effort in searching for neutrino oscillations. The KamLAND experiment confirmed the reactor neutrino deficit corresponding to a small mixing angle θ_{13}. The reactor provided controllable and large neutrino flux, leading to the most precision measurement of the mixing angle θ_{13} despite the smallest.

3.4 Reactor antineutrino anomaly

The θ_{13} reactor based neutrino oscillation experiment mentioned above also made measurements of the spectrum and flux of the reactor neutrinos. A reevaluation of reactor neutrino flux and spectrum was performed using a combination of the *ab initio* and electron conversion approach, as described in Section 3.1. This reevaluation using previous reactor neutrino experiment with baseline < 100 m shifted the global ratio

of observed event rate to predicted rates of 0.976±0.024 to 0.943±0.023, leading to a deficit of 6% from unity [61], also known as the "Reactor Antineutrino Anomaly" (RAA). This is illustrated in Figure 3.5.

One possible explanation to the deficit is a fourth hypothetical sterile neutrino that does not interact but can participate in the three-flavor neutrino oscillation. The mass splitting of such heavy sterile neutrino to the first mass eigenstate Δm^2_{41} is of order of eV^2. Several experiments outside the reactor neutrino physics also hinted at a fourth sterile neutrino with similar mass splitting of eV^2. The accelerator based experiments LSND [62] and MiniBooNE [63] reported excess events. Radiochemical experiments GALLEX [64] and SAGE [65] (also referred as the gallium experiments) observed a deficit in neutrino rate when calibrating using ^{51}Cr and ^{31}Ar. The search of the fourth neutrino (hypothetical sterile neutrino) is well-motivated from the experimental data and the discovery of such particle would indicate new physics outside the Standard Model.

In addition to the flux deficit anomaly described previously, neutrino spectral disagreement between the measurement and the prediction is observed by reactor experiments Daya Bay [58], Double CHOOZ [59], and RENO [60], as shown respectively in Figure 3.6, 3.7, and 3.8. In the prompt visible energy region of 4 to 6 MeV (or equivalently in the 5-7 MeV neutrino energy region), a prominent excess of about $\sim$ 10% is observed. This excess or the bump in the high energy regions of the neutrino spectrum does not depend on the reactor-detector baseline, reactor power and configuration.

In addition to the anomalies we discussed, the flux and spectrum anomalies could depend on the isotopic composition of the fuel evolution. For example, RENO and Daya Bay collaboration reported the dependence of flux and spectrum on the fission isotopes and hinted ^{235}U may be the primary contributor of the reactor antineutrino anomaly [66] and a correlation between the bump change and reactor fuel isotope fraction of ^{235}U [67]. Therefore, very short baseline, HEU ^{235}U-only reactor neutrino experiments are of significant interests.

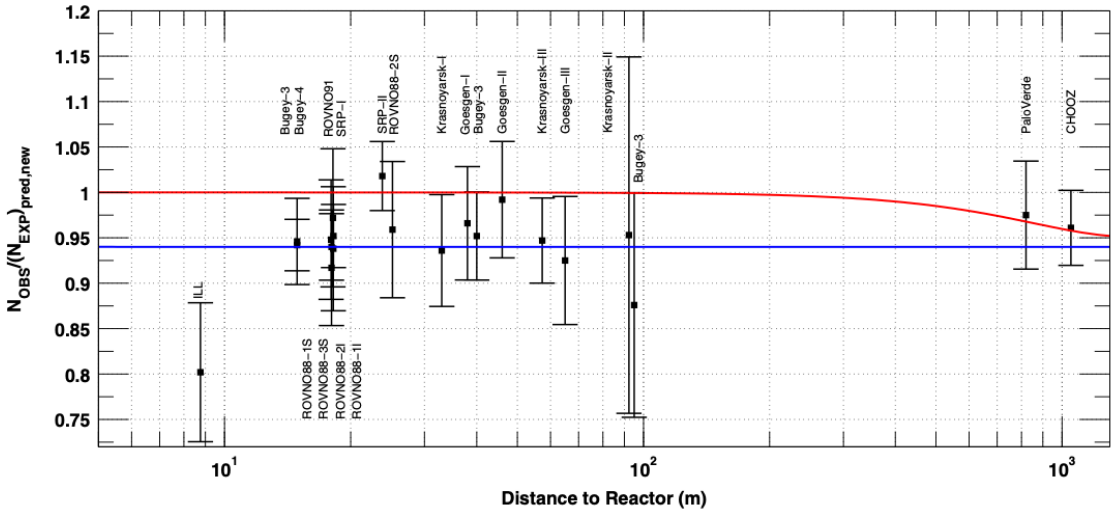


Figure 3.5: Ratio of measured $\overline{\nu}_e$ flux to the new reevaluated model prediction. The global average in blue line indicated a $\sim 6\%$ deficit, the so-called Reactor Antineutrino Anomaly (RAA). A possible explanation is the inclusion of a fourth sterile neutrino in the three neutrino paradigm, with mixing parameters $|\Delta m^2_{41}| \gg 1$ eV^2 and $\sin^2 2\theta_{14} = 0.12$. Source:[61]

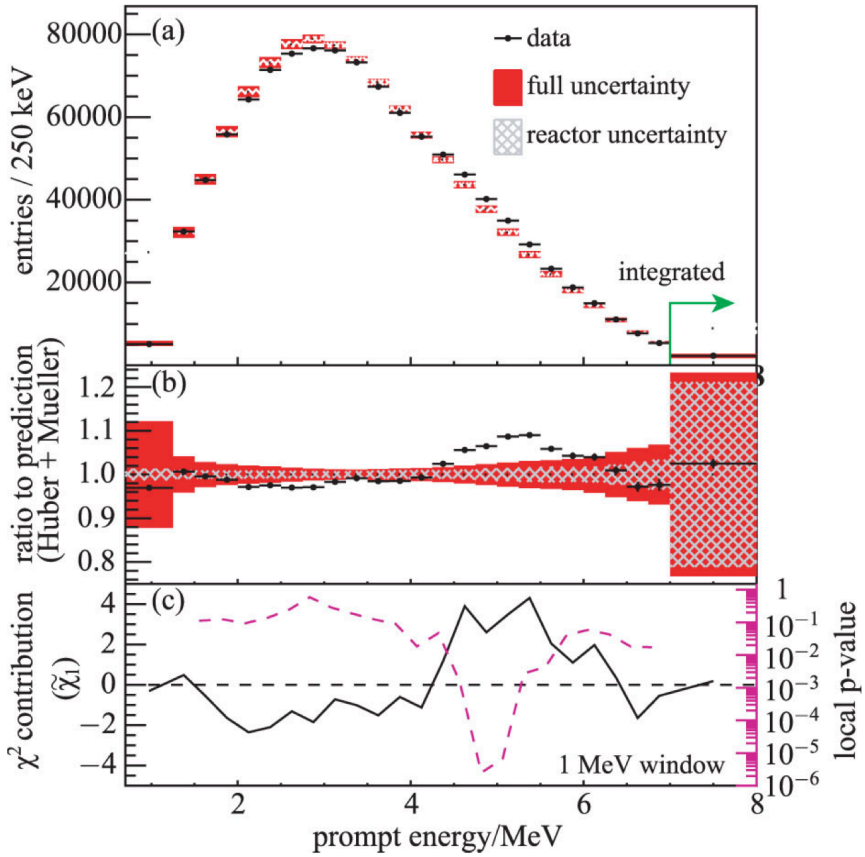


Figure 3.6: Visible spectrum reported by Daya Bay experiment. The ratio of measurement to the Huber-Mueller model prediction is shown in the middle panel. Source:[58]

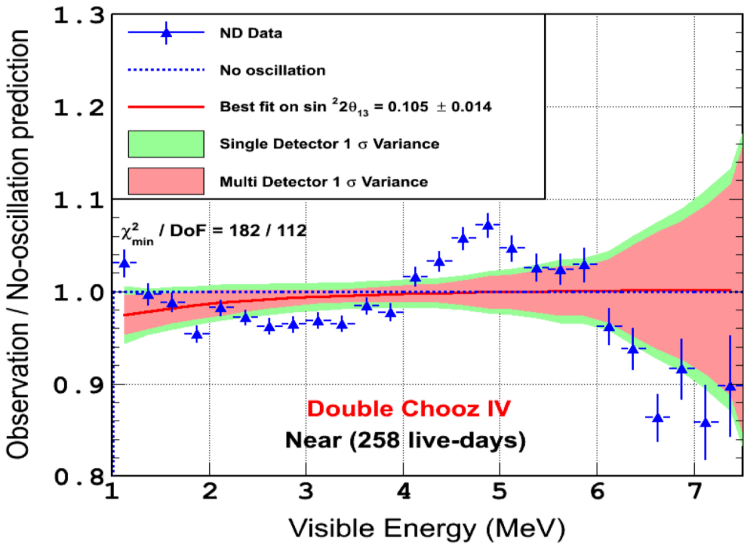


Figure 3.7: Visible energy spectrum reported by Double Chooz experiment. The ratio of measurement to the Huber-Mueller model prediction is shown. Source:[59]

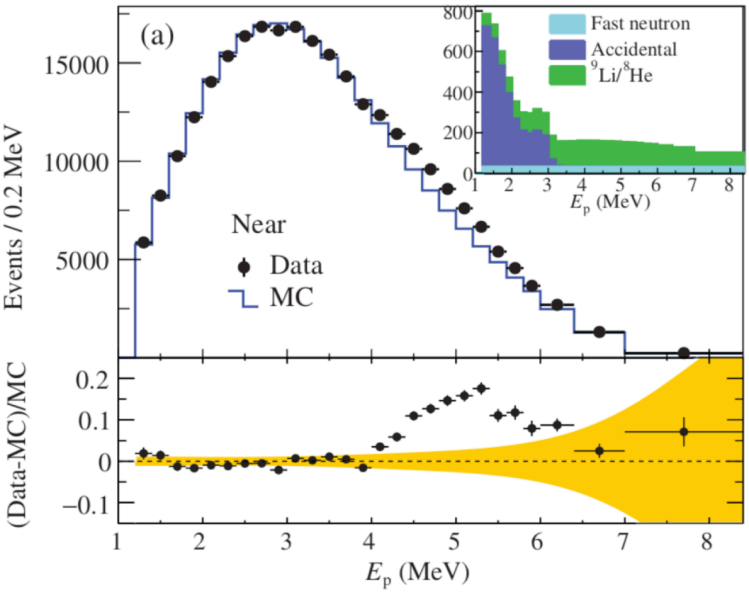


Figure 3.8: Visible energy spectrum reported by RENO experiment. The ratio of measurement to the Huber-Mueller model prediction is shown. Source:[60]

3.5 Current short baseline antineutrino experiment

As discussed in the previous section, new generations of very short baseline reactor neutrino experiment are of particular interest to search for large mass scale sterile neutrinos and explore possible isotopic origin of the bump. The sensitivity of these experiments depends on the distance between the reactor core and the detector, the reactor power, the size of the detector and reactor core, energy resolution of the detector, statistics of the measurements. The primary challenges are limited overburden against cosmogenic background and reactor-related backgrounds. In general, a segmented detector and good pulse shape discrimination (PSD) based particle identification capability is used to achieve good signal-to-noise ratio. A list of short baseline reactor neutrino experiment with key parameters are listed in Table 3.1.

Table 3.1: Key parameters of current short baseline reactor neutrino experiments around the globe.

Experiment	**Reactor**	**Distance**	**Mass**	**Resolution**	**Segment**
DANSS [68, 69]	LEU 3.1GW	10.7-12.7 m	1.1 ton	17%	2D
NEOS [70]	LEU 2.5GW	24 m	1.0 ton	5%	1D
Neutrino-4 [71, 72]	HEU 100MW	6-12 m	0.3 ton	-	2D
Nucifer [73, 74]	HEU 70MW	7.2 m	0.6 ton	10%	1D
PROSPECT [75, 76]	HEU 85MW	7-12 m	1.5 ton	4.5%	2D
STEREO [77, 24]	HEU 58MW	8.9-11.1 m	1.6 ton	8%	2D
SOLID [78, 79]	HEU 75MW	6-9 m	1.6 ton	14%	3D

Chapter 4

PROSPECT experiment

As pointed out at the end of Chapter 3, very short baseline reactor neutrino experiments are sensitive to the search for eV-scale sterile neutrinos and isotopic origin of the bump. A ton-scale, segmented, and IBD-detection-based detector filled with liquid scintillator placed at a very short baseline near a HEU ^{235}U point-like reactor core was proposed to directly tackle the RAA, i.e. the Precision Reactor Oscillation and SPECTrum experiment (PROSPECT). PROSPECT was designed to directly search for eV-scale sterile neutrino oscillation by relative spectrum comparisons between baselines and make precision spectrum measurements of the reactor neutrinos produced by ^{235}U.

4.1 HFIR reactor experimental site

PROSPECT antineutrino detector (AD) operated at the experimental hall in High Flux Isotope Reactor (HFIR) at a baseline about $\sim$ 7 m. HFIR is a research-focused fission reactor completed in 1965, and it had the strongest reactor-based steady-state neutron beam in the United States for neutron science. HFIR uses $\sim$ 93% highly enriched ^{235}U fuel in a compact cylindrical core, with a diameter of 43.5 cm and a height of 50.8 cm [76], as shown in Figure 4.1. The reactor operates at a nominal thermal power of 85 MW for each reactor cycle of typically 24 days. Since the reactor

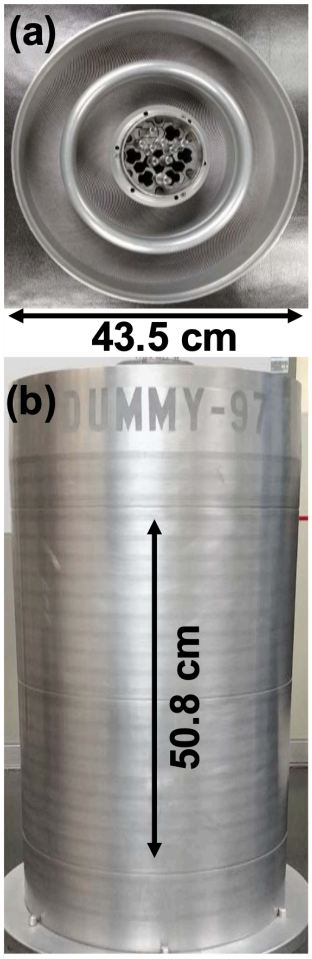


Figure 4.1: Photographs of a dummy HFIR reactor core showing (a) the diameter and (b) the height. Source:[76]

cycle is relatively short and the fuel assembly is completely replaced after the reactor cycle, the fuel evolution effects from the other three fission isotopes can be completely neglected. During the 24 days' reactor-on cycle, $> 99.9\%$ of the $\overline{\nu}_e$ are emitted from the fissions of ^{235}U isotope.

The experimental hall is at the ground level of the reactor building and offers minimal overburden for the PROSPECT AD. The AD sits at an average baseline of ~ 7 m from the reactor core in the pool, shown in Figure 4.2. The lack of overburden at the experiment site and the close proximity to the reactor core pose challenging background mitigation from cosmic rays related fast neutrons and reactor related gammas and neutrons. Comprehensive background characterizations were previously performed [80, 81]. Figure 4.2 shows the AD position relative to the reactor core and proper radiation shielding packages deployed against reactor related backgrounds.

4.2 Detector design

The PROSPECT AD consists of an inner detector filled with $\sim$4 ton ^{6}Li-doped liquid scintillator (LiLS), inner acrylic vessel and outer Aluminum tank, attached shielding packages, and data acquisition (DAQ) and slow control electronics housed in electronic racks on the side, shown in Figure 4.2 and Figure 4.3. The PROSPECT AD design was optimized to offer the best sensitivities to IBD event detections and reduction of backgrounds via the passive shielding packages and active analysis cuts. The PROSPECT AD mainly consists of the following components, from the inner to the outer side, lithium doped liquid scintillator, inner detector containment, shielding packages, and side electronics racks.

Filled with lithium doped liquid scintillator made of organic liquid scintillator based on EJ-309 [82], the inner acrylic tank is contained in outer aluminum tank and further shielded by water bricks, lead, and borated polyethylene from the top and side to mitigate the cosmic rays induced fast neutron backgrounds and reactor related

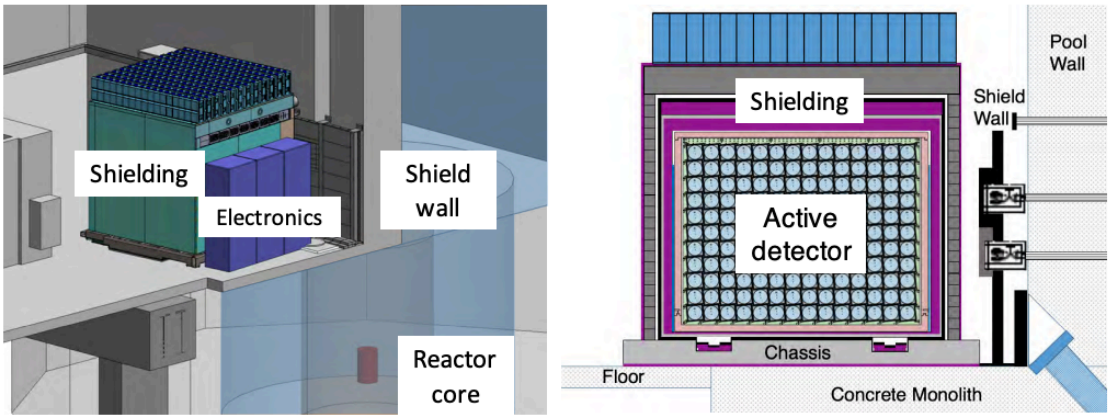


Figure 4.2: Left: schematic of the AD in the experimental hall relative to the reactor core, with an average baseline of 7 m. Right: schematic sideview of the AD shielding against reactor related background. Source:[76]

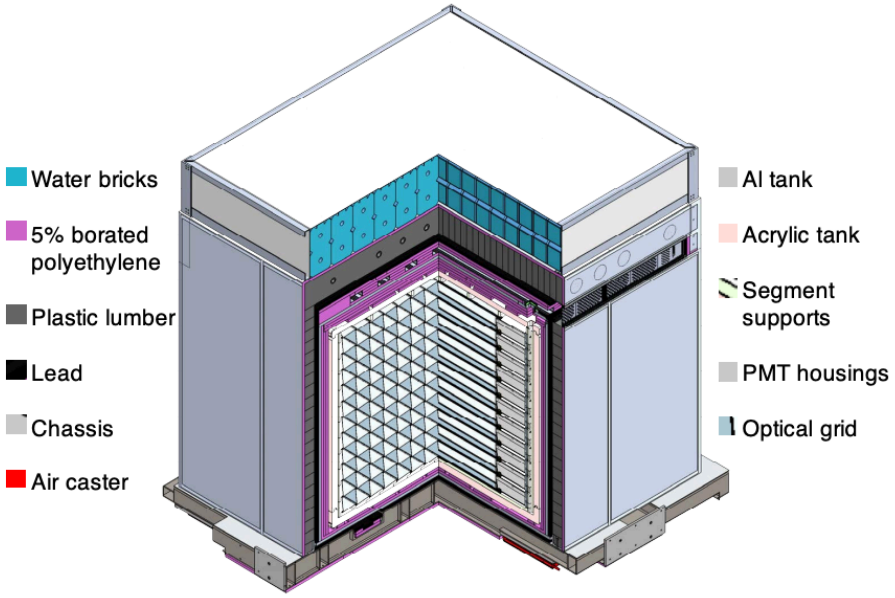


Figure 4.3: A cutaway view of the detector and shielding assembly. Top water bricks shields the cosmic ray related backgrounds. Lead and borated polyethylene in purple shields the inner acrylic vessel from the reactor related backgrounds. The active detector volume is optically segmented by reflective grids into 14×11 uniform segments. Source:[76]

backgrounds. The design of the organic ^{6}Li-doped liquid scintillator was optimized to achieve 4.5% energy resolution of the neutrino spectrum and at the same time to offer pulse shape discrimination (PSD) capability for particle identification. The doped ^{6}Li acts as the main neutron capture isotope for tagging neutrons from the IBD process. The key detector parameters are summarized in Table 4.1. The following section will describe each subsystem of the detector packages in details.

4.2.1 Liquid scintillator

Based on extensive R&D studies, the PROSPECT collaboration developed a novel liquid scintillator loaded with ^{6}Li based on commercially available EJ-309 solvent (di-isopropylnapthalene) [83] with added wavelength shifter of 2,5-diphenyloxazole (PPO) and 1,4-bis(2-methylstyryl)benzene (bis-MSB). The wavelength shifter re-emits light from the liquid scintillator to the wavelength sensitive to PMT light collection. The loading of ^{6}Li isotope was done with a 95%-enriched ^{6}LiCl aqueous solution. The process reduces the light yield of the liquid scintillator by ∼30% to 8200±200 photons/MeV. The liquid scintillator was also spiked with ^{227}Ac (with a half-life of 22 years) uniformly to monitor the relative segment volume variation and position reconstruction resolution [82].

The PROSPECT ^{6}LiLS performs really well in light production and excellent PSD capabilities, thus achieving a final 4.5% relative energy resolution and clear separation of electronic (such as γ-rays and electrons) and nuclear (such as proton elastic scattering) events. A pulse shape discrimination parameter PSD can be established by [82],

$$PSD = (q_{tot} - q_f)/q_{tot}, \tag{4.1}$$

where the total charge q_{tot} is computed from a time interval of 170 ns of the negative signal waveform, and q_f is the charge in a 30 ns interval. The typical PSD distributions are illustrated in Figure 4.4.

The figure-of-merit (FOM) can be defined using the PSD distributions,

$$FOM = (\mu_n - \mu_e)/\sqrt{(FWHM_n + FWHM_e)}, \tag{4.2}$$

where $\mu_{n(e)}$ and $FWHM_{n(e)}$ are the mean and full width at half maximum of the Gaussians corresponding to nuclear (electronic) recoils. Final ^{6}LiLS product underwent quality assurance (QA) checks, shown in Figure 4.5 and the performance of ^{6}LiLS was better than the prototype PROSPECT-50 requirements [84].

Depending on the type materials in contact with, liquid scintillators could exhibit degraded light yield and performance of the scintillator. Extensive material compatibility tests were performed [76], and the following materials were found to be compatible with ^{6}LiLS: fluorinated ethylene propylene (FEP), polytetrafluoroethylene (PTFE), polylactic acid plastic (PLA). Oxygen quenching is also known to reduce the light yield of the liquid scintillator. A cover nitrogen gas was constantly maintained to keep the exposure of oxygen minimal over time.

4.2.2 Optical grid

The active target volume is divided optically into a 14×11 grid, configured in a total of 154 segments. The dimension of each segment is 1.176 m in length by a 14.5×14.5 cm^2 square, rotated by 5.5° to leave space for calibration channels. The optical grid is made up of two major components: reflective separators and polylactic acid (PLA) rods. An interlock mechanism between the PLA rods and separators was designed to form a structural robust optical grid with external acrylic supports on both ends. Figure 4.6 depicts the schematics of the optical grid system. The separators are made of, from the inside to the outside, a carbon fiber backbone providing structural support, reflector layers made of DF2000MA [85], adhesive layers and protective Fluorinated Ethylene Propylene (FEP) films. The separators are fully laminated as shown in Figure 4.7. The FEP films are then sealed and fully surround the separator to avoid the inner material in direct contact with ^{6}LiLS. The reflective layers were

Table 4.1: The PROSPECT antineutrino detector specification

Parameter	Value
Target mass	3.7 tons
Target dimension	1.2 m x 2.0 m x 1.6 m
Target material	Custom LS with 0.08% ^{6}Li doping
Baseline range	7-12 m
Energy resolution	5% at 1 MeV
Optical Segmentation	14 x 11
Segment dimension	117.6 cm x 14.5 cm x 14.5 cm
PMT	5 inch in diameter

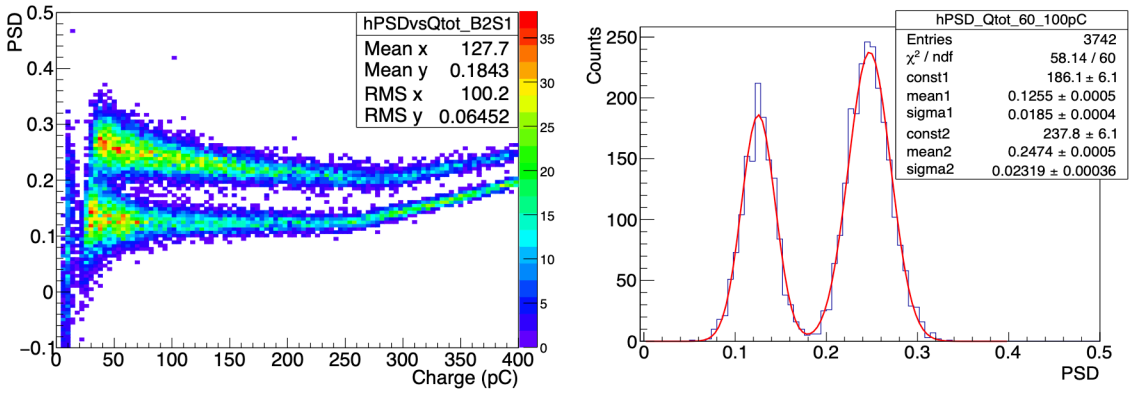


Figure 4.4: PSD distributions of the PROSPECT ^{6}LiLS. Right: PSD distribution fit to Figure of Merit (FOM) at 540 keV visible energy. Source:[82]

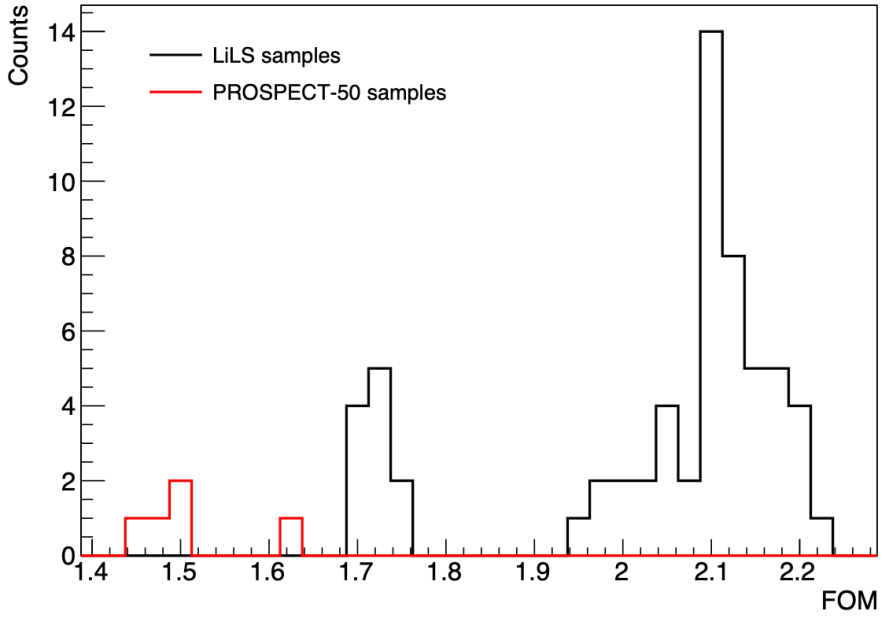


Figure 4.5: QA measurements of the figure of merit of the produced ^{6}LiLS compared to the prototype PROSPECT-50 requirement. Source:[84]

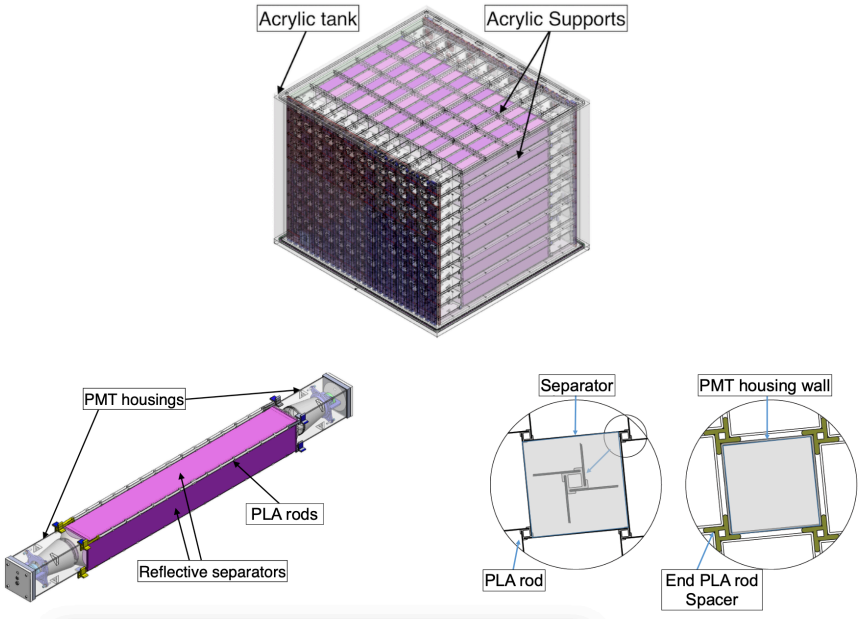


Figure 4.6: Schematics of the PROSPECT optical grid. The top panel shows the optical grid system inside the inner acrylic tank. The left panel shows the individual optical segment, enclosed by double PMTs on the ends. The right panel shows the interlock mechanism between the specular reflective separators and PLA rods. The hollow PLA rods allow for the calibration tube access. Source:[86]

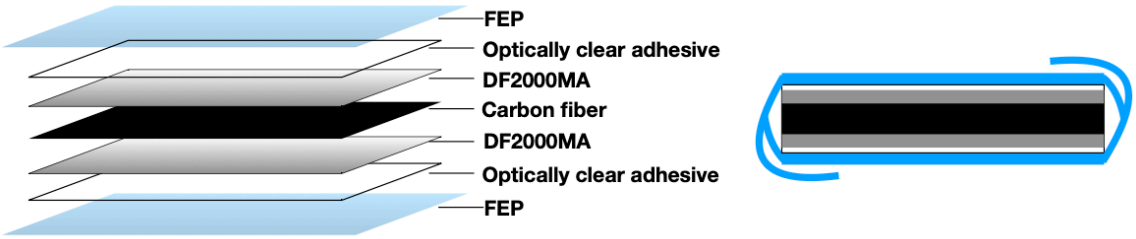


Figure 4.7: Left: The sandwich structure of a separator; Right: heat sealed folded FEP films. Source:[86]

shown high specular reflectance in the wavelength range between 400 nm and 550 nm, where the scintillation light resides. The performance of DF2000MA is shown in Figure 4.8. The reflector FEP film has an index of refraction of 1.33 and is much lower than that of the ^{6}LiLS ($\sim$1.55), providing total internal reflection with high incident angles and minimizing optical cross-talk between segments. During production in a clean room in Illinois Institute of Technology, careful consideration were taken into account to avoid possible scratches, residual dust particle or punctures of FEP film, since they will lead to leakages of the ^{6}LiLS into inner separator materials.

The PLA rods were 3D-printed using white-dyed 100μm PLA, providing a low mass and volume structure for separators. Multiple types of support PLA rods were produced, shown in Figure 4.9. The PLA rods and separators underwent extensive QC examinations during production and assembly.

4.2.3 PMT modules

Scintillation light is collected by a pair of PMT modules in each segment in the PROSPECT AD. The target volume is optically divided into a 14 by 11 grid of 154 segments.

Each segment has double light readout by two PMTs with diameter of 5 inches from each end. Details of the PROSPECT AD and PMTs are shown in Figure 4.10. Two types of PMTs with the same diameters and similar characteristics were used in the AD, 240 PMTs from Hamamatsu and 68 PMTs from ElectronTubes.

The PMT and its base are contained in a housing that's material-compatible with the scintillator, filled with mineral oil, and then submerged in ^{6}LiLS volume. The housing modules consist of the front window made of acrylic for efficient light transport towards the PMT, the sidewalls made of white acrylic, and back plug made of black acrylic supported by a second clear back plug. The cables were fed through the back plug, illustrated in Figure 4.11. The back plug supports offers the ability to stack PMT housing in a grid.

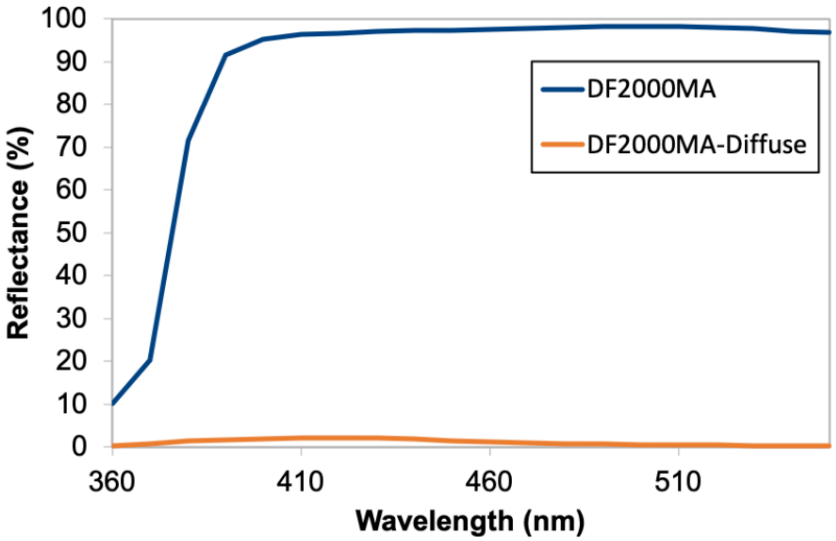


Figure 4.8: Total and diffuse reflectance of DF2000MA in the wavelength range above 360 nm. Source:[86]

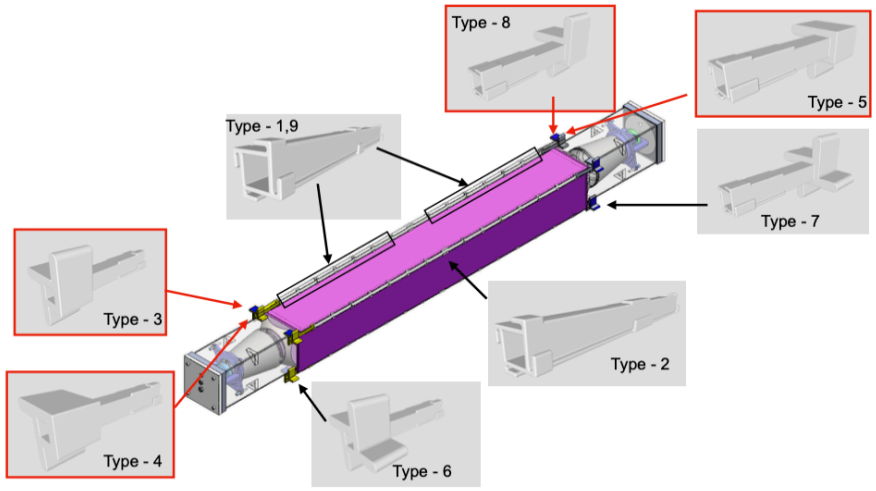


Figure 4.9: Various types of support PLA rods and their assembly location along the segments. Center rods, such as 1,2,9, are used to seal the segments. The end rods, such as 3-8 are used support thick and rigid spacing between PMT housings and center rods [86].

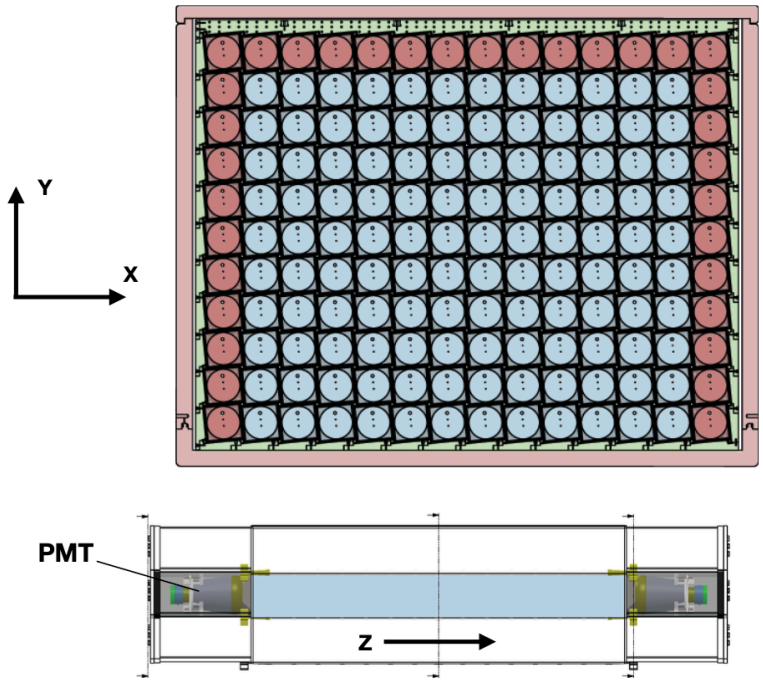


Figure 4.10: Schematics of the PROSPECT AD and PMTs. The red represents the installation of 68 ET PMTs and the blue for the 240 Hamamatsu PMTs. Source:[76]

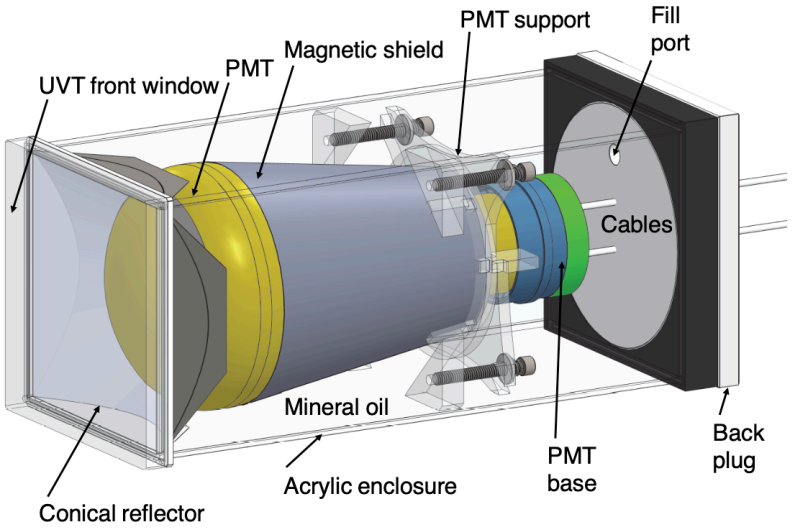


Figure 4.11: Schematic of the PMT module. Source:[76]

Extensive quality check (QC) measurements were performed on all PMT modules under the requirement of structural tolerance and light-tightness. The assembly process of the PMT modules were performed in a cleanroom at Yale Wright Lab. PMT modules underwent PMT base resistance and functionality test before assembled into the PROSPECT AD.

4.2.4 Optical and radioactive calibration systems

The PROSPECT AD achieves percent level precision, requiring accurate determination of the ^{6}LiLS detector response to various particle interactions and precise reconstructions of energy scale and positions of the events. The segmentation nature of the detector allows for *in-situ* calibration schemes. A variety of neutron and γ-ray sources were deployed for energy reconstruction, position reconstruction, and detector resolutions and non-linearity response. Additionally, optical fiber laser system offers measurements of the timing differences and single photoelectron (SPE) response of the PMTs. Both optical calibration system and radioactive calibration system are demonstrated in Figure 4.12.

The radioactive source calibration consists of 3×5 independent stepper motor drive units to move the calibration sources to the designated locations inside the active volume. The absolute position accuracy of the source deployment along each segment is about 1 cm. Sealed capsules of radioactive sources are attached to a toothed drive belt. Stepper motors were used to push the belt along the calibration tubes made of polytetrafluoroethylene (PTFE) in the 7×5 PLA rods for calibration. Table 4.2 lists the deployed radioactive sources used in PROSPECT AD. The drive (timing) belt and the stepper motor are shown in Figure 4.13.

The PTFE calibration tubes also separates the calibration system from the ^{6}LiLS. The motors are located outside the shielded detector and are controlled with Arduino micro-controllers [87], allowing for remote operation via a slow-control interface. The calibration sources were retracted to the home positions outside the detector during

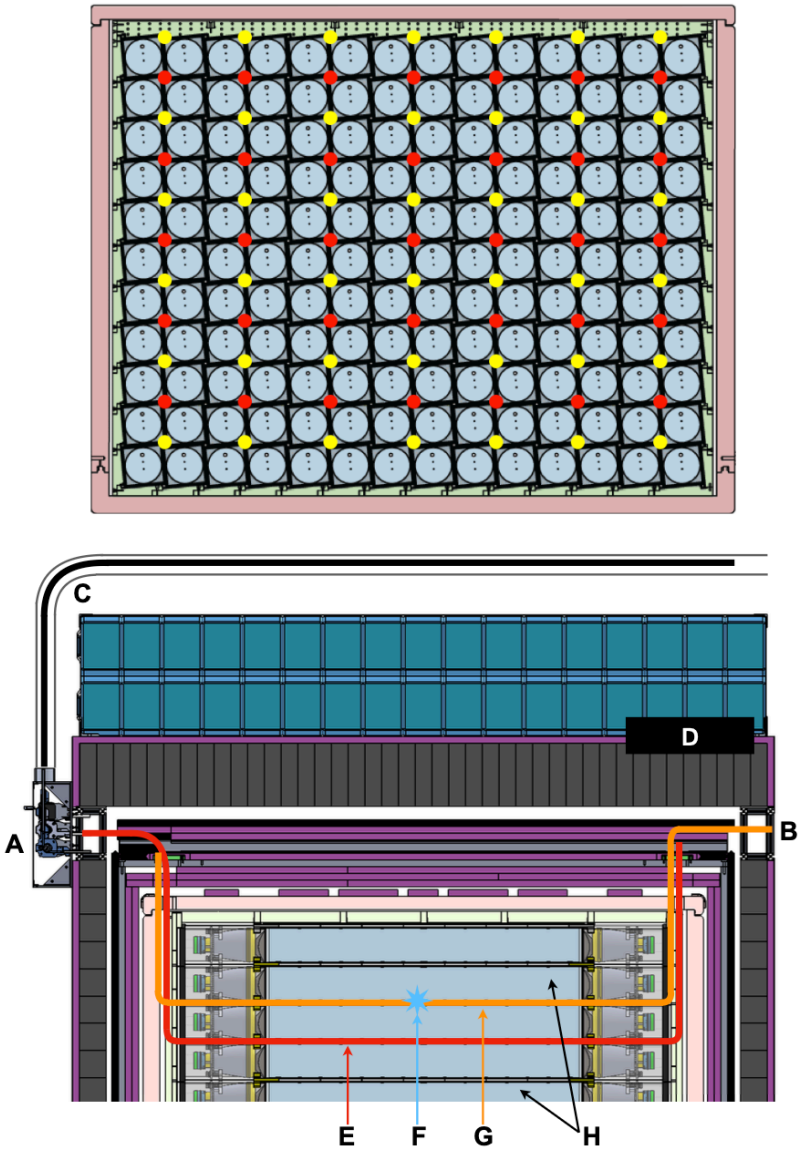


Figure 4.12: The sideview of the PROSPECT AD calibration system. Top: the optical calibration system inserts shown in yellow dots and the radioactive source calibration inserts shown in red. Bottom: AD calibration system details along the axial direction of segments. (A) source drive motors, (B) optical fiber connector panel, (C) belt storage tube,(D) shielding, (E) source deployment tube, (F) light injection point, (G) fiber tube, (H) detector segments. Source:[76]

Table 4.2: Calibration sources and their primary purposes. The AmBe source was acquired near the end of data-taking period and was only used for data-MC validation purposes.

Source	Type	Primary Purpose	Activity
^{137}Cs	γ-ray	segment comparison	0.1 μCi
^{22}Na	γ-ray	positron, edge effects	0.1 μCi
^{60}Co	γ-ray	energy scale	0.1 μCi
^{252}Cf	neutron	neutron response	866 n/s
AmBe	neutron	neutron response	70 n/s

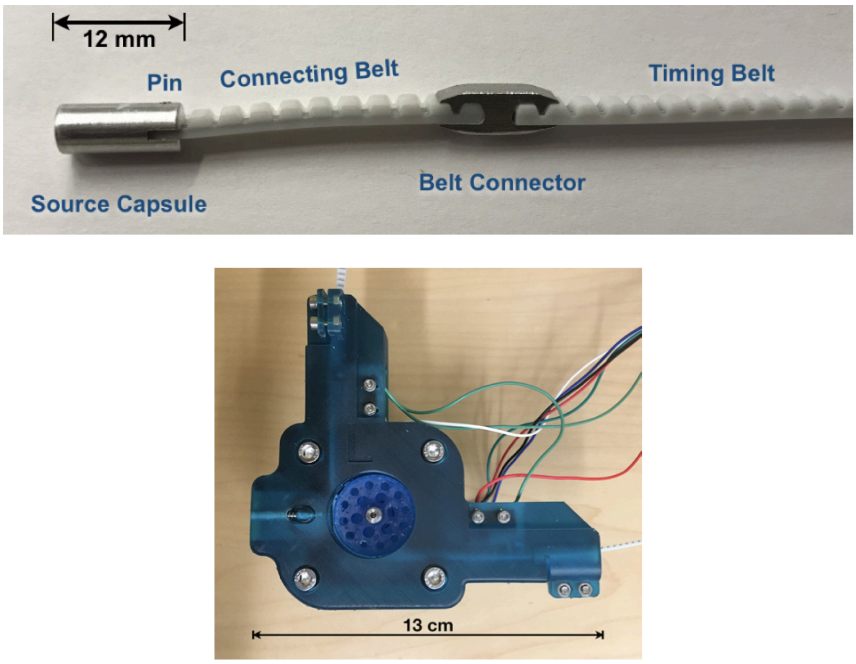


Figure 4.13: Pictures of drive belt (top) and stepper motor(bottom). Source:[88]

detector operation. During detector calibrations, one or multiple sources were driven out by stepper motors to a given position along the length of the tube for a typical calibration acquisition time of 5 or 10 minutes. The radioactive sources were returned back to storage cabinet after each comprehensive calibration campaign. Fully installed radioactive source calibration system is depicted in Figure 4.14.

4.2.5 Detector passive shielding

The design of the passive shielding was informed by HFIR background measurements and consists of layers of shielding packages against reactor-related γ-rays and fast neutron flux originated from the cosmic rays. From outside to the active LS volume of the detector, the shielding packages include a array of water bricks serving as additional overburden to mitigate the cosmogenic fast neutron backgrounds, a layer of 5% borated polyethylene shielding for neutron captures, a layer of lead to shield the neutron capture γ-ray, and a mix of water or borated polyethylene shielding outside the acrylic tank containing ^{6}LiLS target volume. This is also illustrated in Figure 4.3.

A lead shielding wall of 0.1 m thickness was installed between the detector and the concrete pool wall, providing shielding against direct reactor related γ-rays, as illustrated in Figure 4.15.

4.2.6 Detector control and monitoring

High voltage modules All 156×2 PMTs modules are biased by high voltages. The gain of the PMT modules are typically set at 5×10^5 to ensure a linear energy response up to ∼10 MeV during normal data taking. HV cards can be communicated over a local DAQ network. Voltages and currents are monitored during operation.

Cover gas control Nitrogen gas is constantly maintained and form a blanket gap between the air and the active ^{6}LiLS volume to reduces the oxygen quenching of the liquid scintillator, known to degrade the light yield over time. Input flow rate is

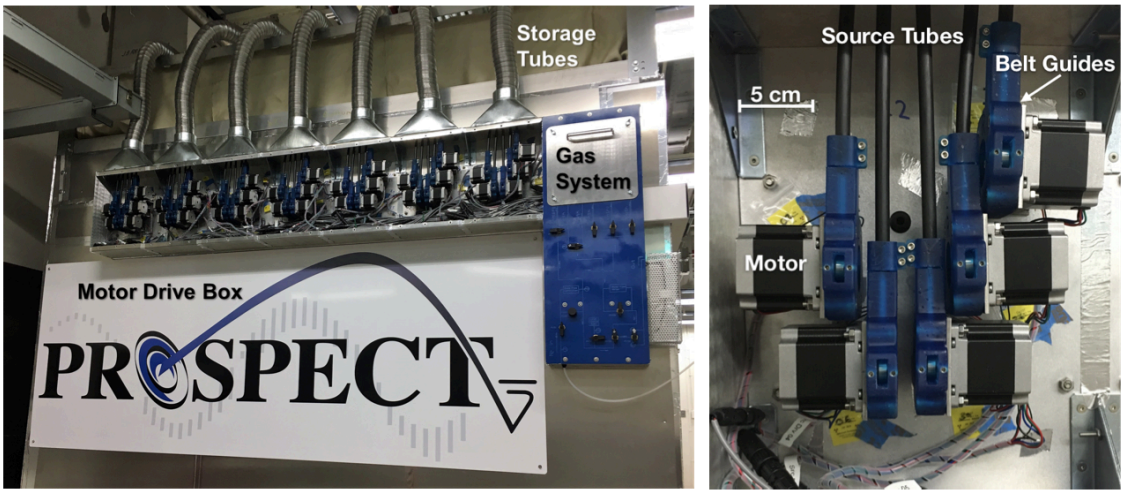


Figure 4.14: Pictures of fully installed radioactive source calibration system, mounted on the side of the detector exterior. The right picture shows a close-up view of the stepper motor modules and calibration tubes. Source:[88]

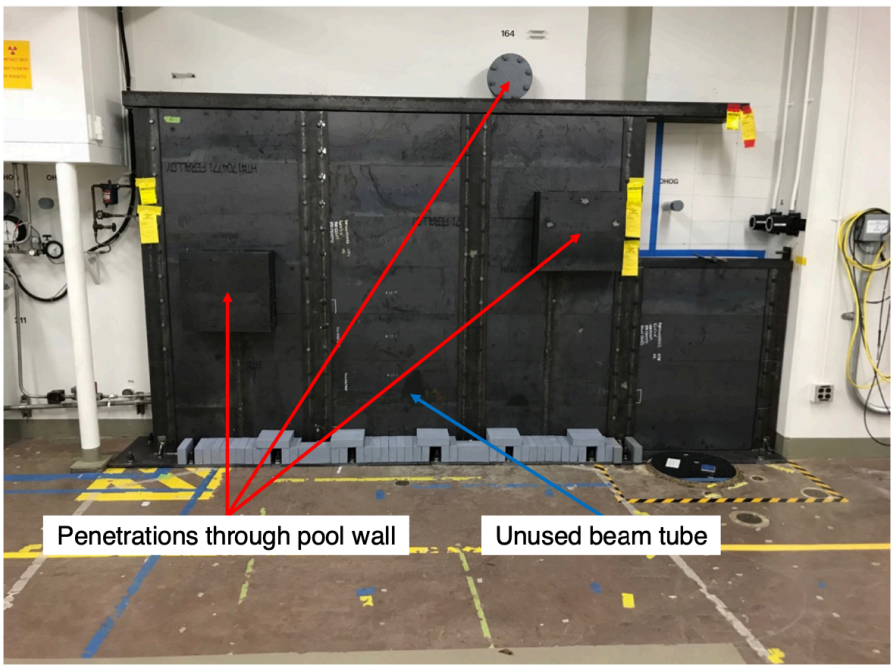


Figure 4.15: Photograph of the lead wall between the detector and reactor pool. Source:[76]

monitored and can be adjusted according to the flow feedback monitored by a flow meter, also shown the left picture in Figure 4.14.

Temperature and liquid level monitoring The temperature of ^{6}LiLS are monitored by resistance temperature detectors (RTDs) at 11 locations in the active volume. The environment temperature can fluctuate and rises up to 28 ℃ in the case of AC power outage at HFIR. The temperature of the water in the aluminum tank is also monitored by a RTD. Ultrasonic sensors are deployed to measure the ^{6}LiLS and water levels. Figure 4.16 shows the temperature fluctuations during detector operation.

4.2.7 Data acquisition system

The data acquisition system of the PROSPECT experiment is composed of two Weiner VME crates housing 21 CAEN Waveform Digitizers (WFD) [89], a Phillips Scientific NIM crate [90], two DAQ PCs, storage array, and a run control computer. The schematics of the PROSPECT DAQ system is illustrated in Figure 4.17.

The DAQ system is capable of a wide dynamic range of energy measurement up to 15 MeV by adjusting the HV gains of the PMTs. The wide dynamic range also covers not only the full IBD prompt energy range, but also the electron spectrum produced from the cosmogenically produced ^{12}B up to 15 MeV, which is the only source for constraining the energy scale model at high energy regions.

The detector triggers data collection when both PMTs received a signal above a trigger threshold of 50 ADC channels ($\sim$100 keV) within 64 ns time window. The acquisition window is 148 samples in 592 ns. The pulses from both PMTs are only recorded if their height exceeds a zero length encoding (ZLE) threshold of 20 ADC channels. The implementation of zero length encoding significantly reduces the large data streams during reactor-on operation. The post-ZLE waveforms are transferred from the WFDs to the optical fiber cards in separate DAQ computers via the CAEN

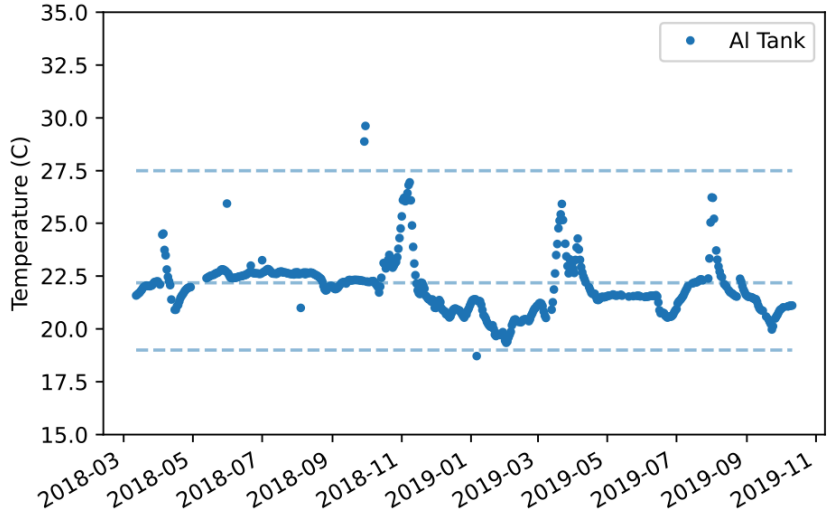


Figure 4.16: Environment temperature fluctuations. The spikes are caused by temporary shut down of AC at the experimental hall at HFIR. Source:[91]

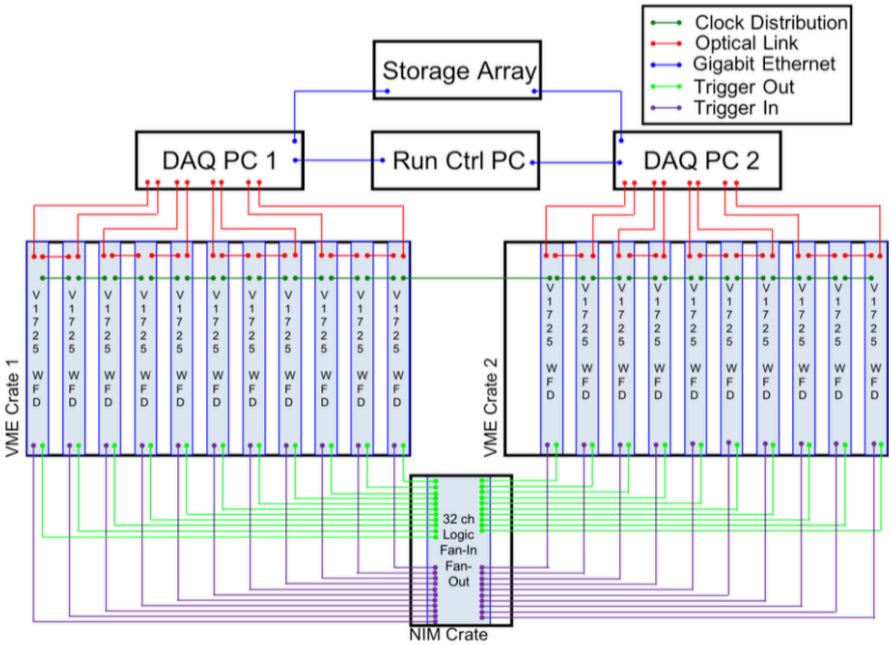


Figure 4.17: Schematics of the PROSPECT DAQ system. Source:[76]

CONET2 optical fiber. The DAQ computers send the data streams to a local 20TB RAID-6 disk array over the local ethernet network. The data are then transferred to Oak Ridge and Livermore National Laboratory computer clusters, with a storage buffer more than two weeks' capacity in case of network outages.

4.3 Detector construction and commissioning timeline

The PROSPECT program started with intensive R&D studies and several prototyping, followed by key component fabrication completed and delivered to Yale University in 2017, including the PLA support rods, reflective separators, PMT Modules, ^{6}LiLS. The inner detector assembly took place in a cleanroom at Yale.

The assembled inner detector was then moved to a transparent acrylic tank, and later moved to the secondary light-tight aluminum tank, The gap in between two tanks was installed with borated polyethylene boards. The assembled PROSPECT AD was then tested without liquid scintillator (dry commissioning) locally, checking the electronics and DAQ system. Afterwards, the detector was transported in an air-ride trailer to the HFIR maintenance facility at ORNL in February 2018. Shocker sensors capable of recording acceleration, GPS, humidity, and temperature were deployed to monitor potential damage caused during shipping.

The ^{6}LiLS was shipped from Brookhaven National Laboratory in multi-drums with nitrogen cover gas inside temperature-controlled trucks. Then the ^{6}LiLS was transferred from the drums into a 20-ton Teflon lined shipping container (ISO tank). The ^{227}Ac-spiked drum was mixed in the ISO tank to ensure uniform distribution. The ORNL/UTK group performed UV-vis measurements on samples of each drums for quality control. Consistent UV-vis spectra were found between the ISO tank and the average of the drums. After ^{6}LiLS mixing in ISO tank and moved to outside the

HFIR building, a total of 4340 kg ^{6}LiLS filled to the detector from the ISO tank, with a controlled filling rate of 3 liter/minute.

A wet commissioning test was performed after completing the external shielding and calibration system assembly to check the electronics. Initial calibration was used to determine the high voltages for PMTs to achieve the desired gain. In March 2018, the first measurement was taken with the reactor on, confirming neutrino detection at 5σ statistical significance within two hours' on-surface reactor-on data-taking .



Figure 4.18: Photograph of the assembly process of 154 segments.

Chapter 5

Neutrino detection physics and detector calibration

The PROSPECT AD makes precision measurements of the ^{235}U neutrino spectrum by not only accurately reconstructing the energy of the incident neutrinos, but also being able to distinguish different particle types. The ^{6}LiLS provides great particle identification capability as well as high scintillation light yield, thus is an excellent material for detecting neutrinos. Neutrinos from the reactor fission process interact with the ^{6}LiLS and create ionizing particles traversing the detector target volume, generating scintillation light along the path. The scintillation light is then collected by the PMTs of PROSPECT AD. The light yield of ^{6}LiLS in response the incident particles is not straightforward proportional to the incident energy, and undergoes a so-called quenching effect causing nonlinear energy response. Thus, understanding of the nonlinearity of light yield of the PROSPECT ^{6}LiLS plays a crucial role in precise energy reconstruction of the neutrino spectrum.

I will start the section discussing the neutrino detection principle in PROSPECT experiment. Then I go over the underlying physics governing the particle interactions with the liquid scintillator. Lastly, results of Monte Carlo simulations and calibrations of PROSPECT AD detector response are presented.

5.1 Neutrino detection

Antineutrinos from the reactor with energy ≥1.8 MeV are detected via the identification of the positron and neutron in the IBD interaction,

$$\overline{\nu}_e + p \rightarrow e^+ + n, \tag{5.1}$$

The positron deposits most of its kinetic energy immediately in the ^{6}LiLS by converting its kinetic energy to LS scintillation light, which we will discuss in detail in Section 5.2. Subsequently, the positron will annihilate with an electron and produce two opposite 0.511 MeV γ-rays. The annihilation γ-rays interact with the ^{6}LiLS via Compton scattering.

In PROSPECT AD, the neutron capture isotopes are primarily hydrogen and ^{6}Li, with $\sim$ 80% fraction of the captures happen on ^{6}Li,

$$n + {}^6\mathrm{Li} \rightarrow \alpha + {}^3\mathrm{H}, \tag{5.2}$$

The heavy charged particles α and ^{3}H with high ionization density travel a short distance on the scale of mm inside ^{6}LiLS, leaving the neutron signal localized and detected in the same segment where the IBD takes place. Neutrons can also capture on the hydrogen, which is abundant in the scintillator, emitting a 2.22 MeV γ-ray. The schematics of the IBD process and particle interactions in the ^{6}LiLS are illustrated in Figure 5.1.

The prompt positron signal and delayed neutron capture signal form a unique correlation in space and time. In addition, the scintillator is capable of particle discrimination via the pulse shape discrimination (PSD),

$$PSD = \frac{Q_{tail}}{Q_{full}}, \tag{5.3}$$

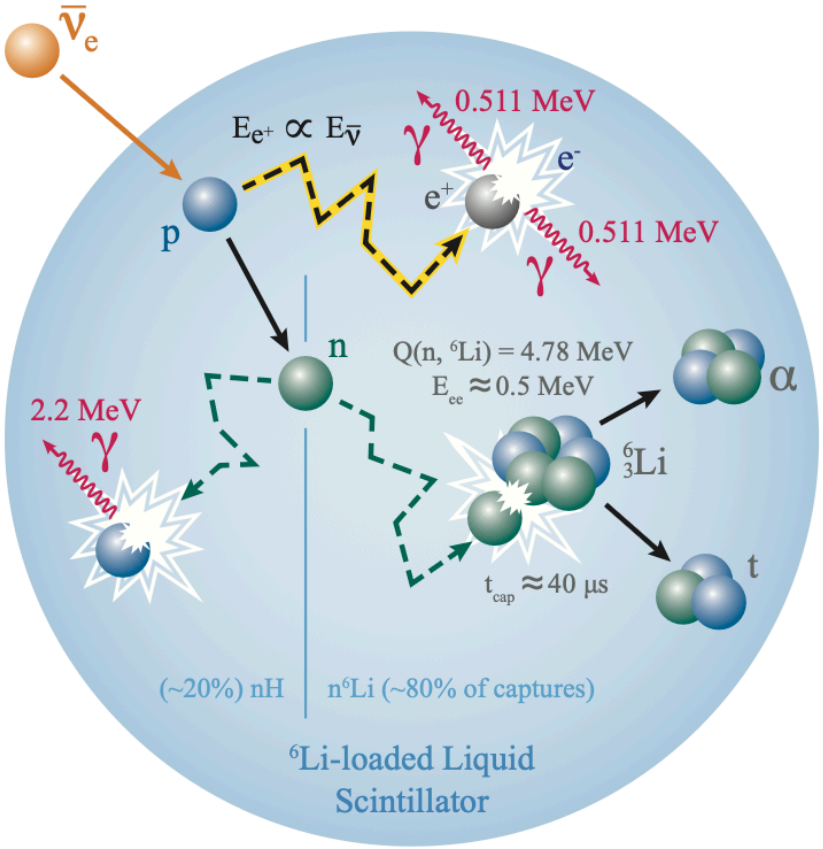


Figure 5.1: The schematics of the IBD process and particle interactions in the ^{6}LiLS. An IBD interaction consists of an energetic prompt positron signal and a delayed neutron capture on ^{6}Li within 50 μs, generating $\sim$ 0.55 MeV electron equivalent.

where Q_{tail} is the amount of charge of the PMT pulse tails, and Q_{full} is the total charge, as shown in Figure 5.2. The combination of the unique correlation in the IBD process and the PSD particle discrimination of the liquid scintillator offers a distinct handle for neutrino signal identification.

5.2 Mechanism of liquid scintillation

The ^{6}LiLS used in the PROSPECT AD converts the kinetic energy of the products of the IBD process into scintillation light. The scintillation light is then collected by PMTs and calibrated to reconstruct the energy of the incident particle. The cause of the scintillation light is the ionization of the scintillator molecules by the incident particle. The energy of the incident particle is transferred to conjugated phenyl groups. The phenyl groups contain delocalized electrons in their π-bonds, thus allowing an emission of light in the blue or visible energy range.

The scintillation photons released from the excited states per incident particle energy is often referred as the scintillation efficiency. The overall signal detection efficiency, however, also depends on the quantum efficiency of the PMTs (typically 30% at peak), and the efficiency of the light transport and collection (which depends on, in the case of the PROSPECT AD, the properties of the reflective panels, and any light absorption/attenuation). A typical light output in PROSPECT AD segments is shown in Figure 5.3. The efficiency can be also affected by non-fluorescent impurities and thermal motion of the molecules.

The phenyl groups electronic structure allows for excitations into singlet states (S_i) or triplet states (T_i). The time scale of the de-excitation of the electronic state to the ground state depends on whether it is a singlet state or triplet state. Singlet states typically decay over a few to tens of nanosecond (fluorescence), and triplet states typically decay over milliseconds or longer (phosphorescence) since the transition is suppressed due to selection rules (requiring additional spin flips). The decay of the

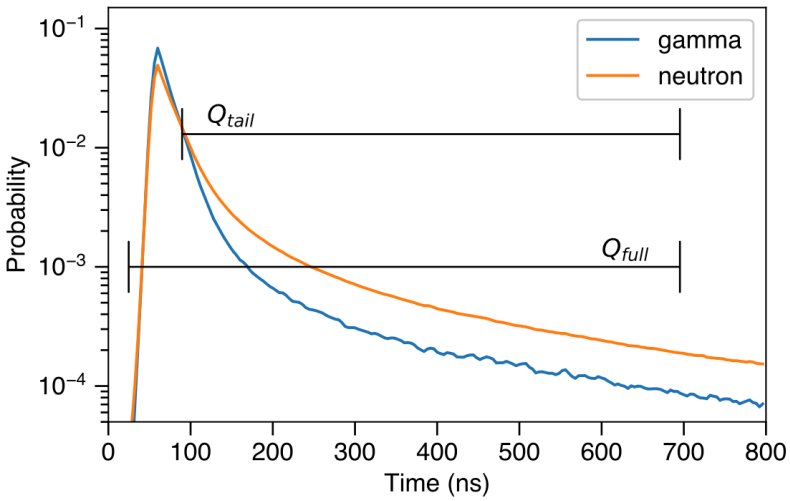


Figure 5.2: Example pulse shapes for electronic recoils and nuclear recoils. The total and tail fraction of the pulse integral are also illustrated.

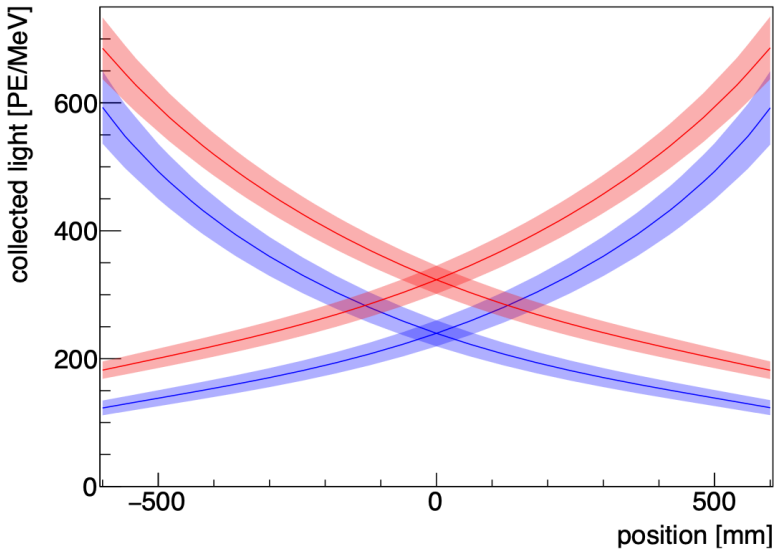


Figure 5.3: Position dependence of light collection in the PROSPECT AD segment. The blue and red band indicates the RMS spread between segments and the performance of the liquid scintillator at the beginning (red) and end (blue). Source:[92]

excited electronic states in a scintillator can be expressed in a double-exponential relation,

$$N(t) = A_f \exp(-\frac{t}{t_f}) + A_s \exp(-\frac{t}{t_s}), \tag{5.4}$$

where t denotes time, N is the number of photons emitted, and A_f and A_s are the weight factor for the fast and slow decays, and t_f and t_s are the time constants of the fast and slow decays. The ratio of the fast and slow component of the decay process is purely determined by the stoping power of the traveling ionizing particle, enabling particle identification capability of the liquid scintillator via the PSD technique in Equation 5.3.

The fluorescent radiation in a scintillator with just one solvent are mostly self-absorbed because the absorption and emission spectra are highly overlapped. To avoid the self-absorption loss of scintillation light, more types of fluorescence molecules are typically introduced in the solvent, called fluors (primary type) or wavelength shifters (secondary type). The absorption spectrum of the primary fluor overlaps with the emission spectrum of the solvent, and the shifted wavelength of the scintillation light is then better matched to the PMT photocathode response.

In the perfect light conversion case, the light yield can be expressed linearly as a function of the stopping power, where the excited and ionized scintillator molecules are well separated along the path of incident particle and their interactions can be neglected,

$$\frac{dL}{dx} = S\frac{dE}{dx}, \tag{5.5}$$

where S is the scintillation efficiency. In reality, the loss of the scintillation light can occur because high densities of the excited and ionized scintillator molecules. This leads to non-linear relation in the scintillation response, called ionization quenching. The quenching effect highly depends on $\frac{dE}{dx}$, causing it to be particle and energy dependent. The quenching effect also gets stronger when the energy loss per path length $\frac{dE}{dx}$ is large, especially at the low energies, e.g., near the end of a particle track. Heavier particles experience a stronger quenching effect, due to its high densities of

the excitation and ionization. For example, the light yield of an α particle can be more than a factor of 10 lower compared to an electron of the same energy. In addition, the strong quenching effect is often accompanied by more triplet state excitations, causing the larger PSD values in terms of decay time.

A semi-empirical equation describing ionization quenched light yield per path length as a function of the energy loss per path length is based on Birks' law [93],

$$\frac{dL}{dx} = \frac{S\frac{dE}{dx}}{1 + k_{B1}\frac{dE}{dx}}, \tag{5.6}$$

where dL is the scintillation light per length dx along the path of the incident particle, S is the scintillation effieciency, and k_B is Birks' quenching factor. For electrons, the typical value of k_{B1} is 0.01–0.03 cm/MeV [94]. A more generalized form Chou's Equation [95] takes the form,

$$\frac{dL}{dx} = \frac{S\frac{dE}{dx}}{1 + k_{B1}\frac{dE}{dx} + k_{B2}(\frac{dE}{dx})^2}, \tag{5.7}$$

where k_{B1} and k_{B2} are the first and second order approximation constants. The values of k_{B1} and k_{B2} are uniquely determined by scintillator materials. Several models have been developed to describe the quenching mechanisms [96, 97]. The light yield of heavier particles are lower than those of electrons and gammas, causing the reconstructed energy in scintillator detector quite different from the actual deposited energy of the incident particles.

Each scintillator has its unique values of the Birks' quenching factors k_{B1} and k_{B2}. The PROSPECT AD detector response (See Section 5.4) includes the Birks' quenching factor and the determination of the values requires a comprehensive calibration campaign and well benchmarked Monte-Carlo simulation packages.

The scintillation light is emitted isotropically from the decay location of the excited molecules. There is another source of light in the PROSPECT AD that's directional, produced via Cherenkov radiation [98]. Cherenkov light is emitted when the speed of

the particle exceeds the speed of light in a medium. The total energy of Cherenkov light produced can be expressed as,

$$E_c = k_C \int_\lambda \frac{2\pi\alpha z^2}{\lambda}\Big(1 - \frac{1}{\beta^2 n^2(\lambda)}\Big) E_\lambda d\lambda, \tag{5.8}$$

where the integrand is the number of Cherenkov photons emitted per unit wavelength, α is the fine structure constant, z is the particle's electric charge, β is the speed of the particle, $n(\lambda)$ is the index of refraction of the medium, E_λ is the energy of those Cherenkov photons, and k_C is an effective normalization parameter (an estimate of additional 30-40% scintillation photons) that scales Cherenkov light production with respect to a default estimate based on constant scintillator refractive index assumptions for wavelengths in the 200-700 nm range.

5.3 Low-level calibration

With the overview of the physics mechanism of the liquid scintillation and the neutrino detection method described in Section 5.2 and 5.1, we are ready to discuss the details of calibrating the detector response, reconstructing the physical quantities, such as the energy, position, and time of the events from raw data of digitizer readout.

The conversion of the raw data to the physics quantities in PROSPECT experiment is performed within the analysis framework **PROSPECT2x_Analysis** [99], which also provides a plugin-based platform for other high level analyses.

Raw data recorded by the WFD modules were stored on local disks in a binary format, and consisted of the waveform information as well as run metadata provided by digitizer. The program **Unpack** produces converted waveform information in **ROOT TTree** format from all WFD modules. The unpacked **TTree** contains the event ID, PMT channel ID, sample number and the waveforms of the samples. The unpacked data is then fed into the **PulseCruncher** program, and converted to **DetPulse** data. The **DetPulse** files contains a summarized information of

the waveform pulse, with added attributes such as arrival time, pulse integral, height, baseline, leading-edge rise-time and PSD parameter. Then calibrations were performed on **DetPulse** data to generate physics quantities stored in **PhysPulse** data. The physics quantities were extracted by combining and matching **DetPulse** from both PMTs in the same segment, with some of the key attributes such as event number, segment number, event time, pulse time difference, z position of the pulse, reconstructed energy, combined PSD value, and particle ID.

The low level calibrations applied to **DetPulse** are described next:

5.3.1 PMT timing offset

Ideally, the scintillation light coming from the center of the segment should produce no PMT time difference between the pair of PMTs. However, variations in PMTs electronics, cable length variations, and WFD board clock can cause a non-zero timing offset. The offset can be calibrated out by traversing cosmogenic muon tracks. The normal muon tracks would deposit energies outside the range of WFDs, thus only the shorter muon tracks around the segment corners (corner-clipping) track were selected. The muon track statistics is sufficient for a hour-by-hour run analysis. They provide signal coincidences across multiple segments. Two timing matrices T_i and dT_i can be generated for each segment i in the (x,y) coordinate, and their matrix element is defined below,

$$t_i = \frac{t_i^0 + t_i^1}{2}, \tag{5.9}$$

where t_i^0 and t_i^1 are the arrival time of PMT 0 and PMT 1 in the same segment i, and the second matrix is the differential time,

$$dt_i = t_i^0 - t_i^1, \tag{5.10}$$

These two matrices can be solved to find the set of $\bar{t}_i$ and $d\bar{t}_i$ values via the information provided by the muon track timing information across the detector segments, as shown in Figure 5.4.

5.3.2 Map PMT timing to z-position along the segment

The PMT timing differential can provide information on determining the absolute z-position of the event along the segment. The PROSPECT PLA mechanical support tabs along the edge of the segments provide a natural ruler for such calibrations. Using a subset of the same corner-clipping muon tracks, the PLA rod tabs causes distortions to the light and timing information collected by the PMT, referred as the "Hobbes effect". Such effects are illustrated in Figure 5.5.

The dt distribution is fitted with the "M shaped" function form $M(dt)$ below,

$$n(dt) = M(dt)[1 + k\cos(\frac{2\pi}{\delta}(adt + bdt^2))], \tag{5.11}$$

where δ = 78.5mm represents the distance between the tabs, and k,b,a are fit parameters. The reconstructed $z(dt)$ is expressed as,

$$z(dt) = adt + bdt^2, \tag{5.12}$$

An example of the dt distribution in segment 49 is shown in the left of Figure 5.6. The model was validated by z-position scans of the radioactive γ-ray calibration along the length of the segment, confirming $z(dt)$ precision of $\pm$1 cm across all the segments.

5.3.3 Combined PSD parameter for each segment

To produce a single PSD value for the event in a segment, PSD values from the two PMTs in a segment are position-dependence corrected and then statistically combined. The position dependence of PSD values are mapped out by the use of

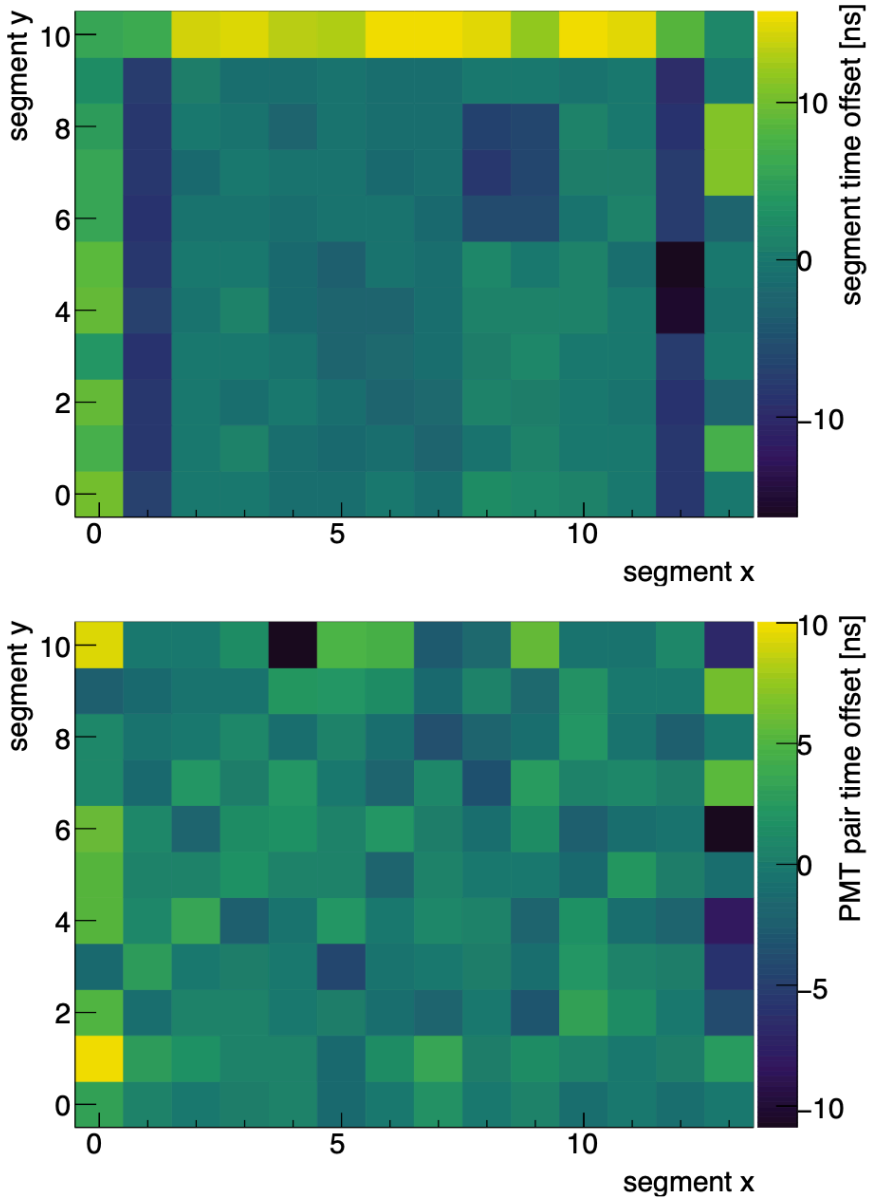


Figure 5.4: PMT timing calibration constants from one of March 2018 physics run. Top: $\bar{t}_i$ segment map; clear features visible between ET and Hamamatsu PMTs, originating from the clock offsets and systematic differences. Bottom; $d\bar{t}_i$ segment map. Source:[92]

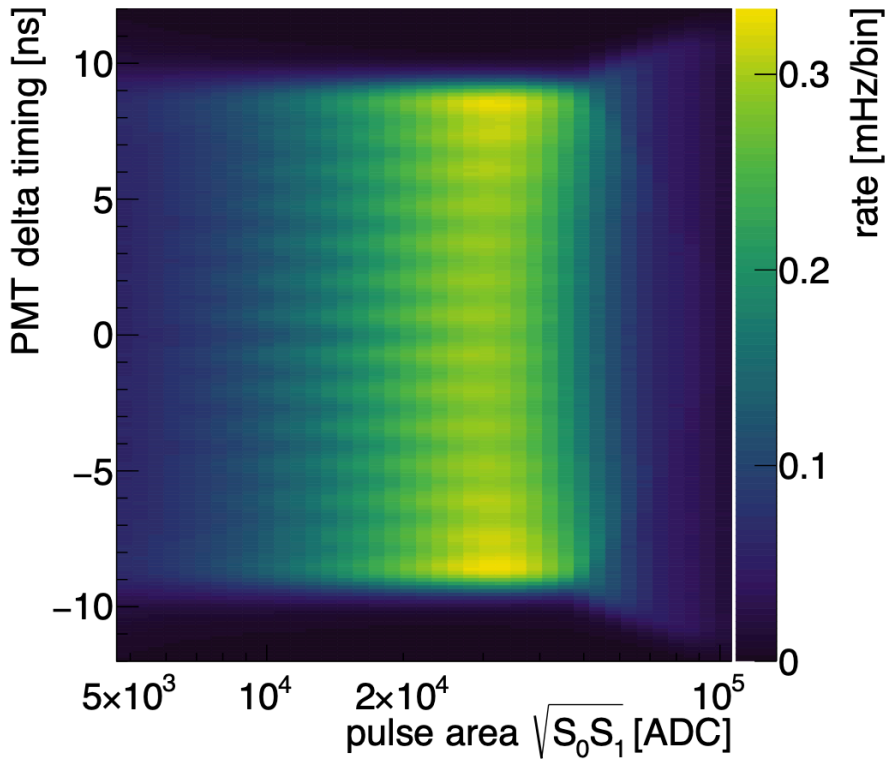


Figure 5.5: The "Hobbes effect" from corner clipping muons for z-position calibration. The map shows the PMT timing differential dt distribution. Source:[92]

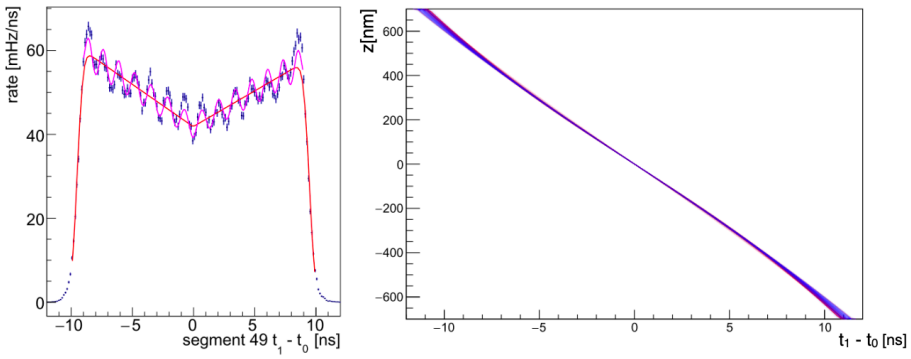


Figure 5.6: Left: fitted results of the dt data for segment 49. Right: $z(dt)$ data from 154 segments, blue (red) for Hamamatsu (ET) PMTs. Source:[100]

the corner-clipping muon hits, with the PSD tail fraction increasing with distance from the PMT. The observed distribution is empirically fit as a three-parameter function of dt for each segment,

$$PSD(dt) = p(1 + d[1 - \exp kdt]), \tag{5.13}$$

Figure 5.7 shows PSD position dependence and position dependence corrected PSD distribution. The position dependent part of the PSD component is subtracted off from each pulse, removing the position dependence. The two position-independent PSD values from each pulse are then statistically averaged, weighted by the estimated number of photoelectrons in each pulse, producing a single PSD value. Figure 5.8 shows the calibrated PSD values for a large number of ^{6}Li-captured spallation neutrons following a candidate muon track.

5.3.4 ADC to energy conversion

The neutron captures on ^{6}Li events can be used to convert the ADC to energy since the neutron captures on ^{6}Li events have very localized PSD and energy, as shown in Figure 5.8. These neutron captures on ^{6}Li are selected in time coincidence with cosmic muon signals.

The light collection is also known to depend on the distance from the PMTs, mainly due to a combination of light attenuation and leakage before reaching the PMTs on the ends. In order the quantify the light collection attenuation and the z-dependence, we can define the following two variables,

$$R(dt) = \frac{S_1}{S_0}, \tag{5.14}$$

$$S(dt) = \sqrt{S_1 S_0}, \tag{5.15}$$

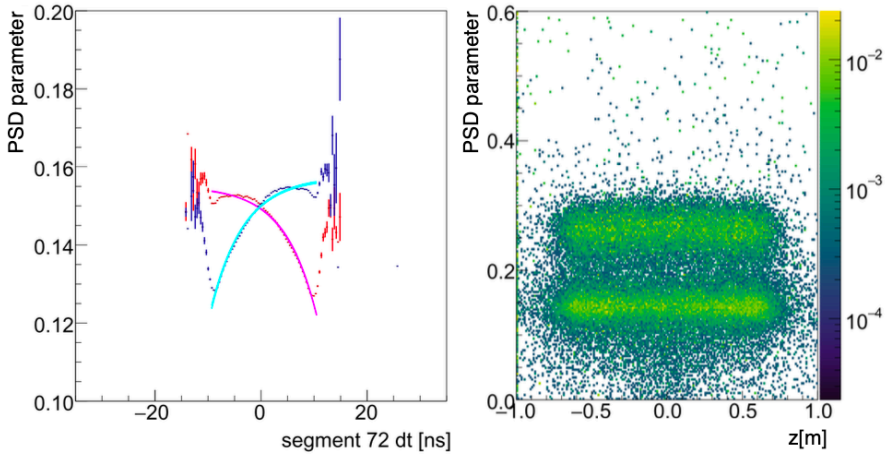


Figure 5.7: Left: Position dependent PSD vs *dt* for a particular segment. The blue and red are PSD data. Cyan and magenta represents the fits described in Equation 5.13. Right: PSD values after the position correction. Source:[101]

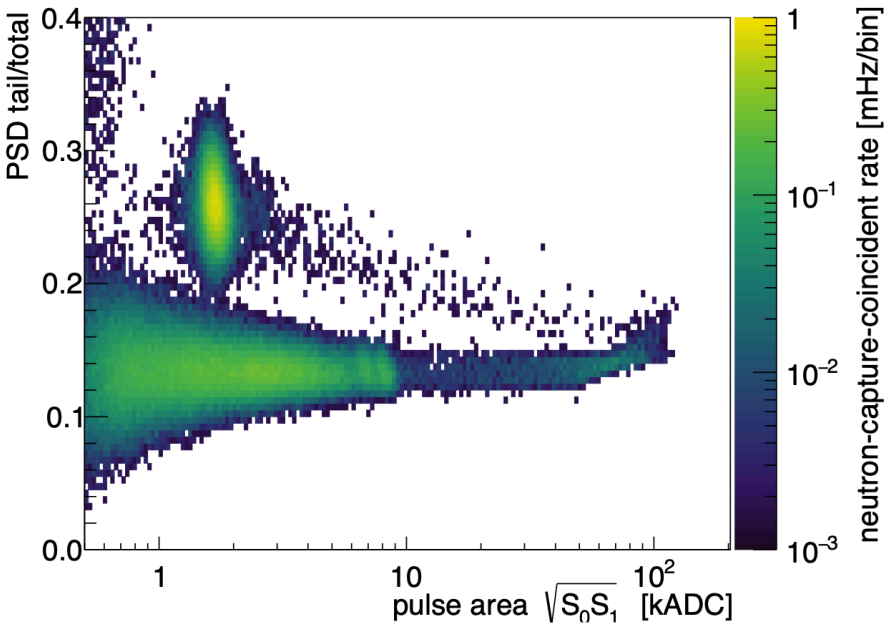


Figure 5.8: Calibrated pulse PSD for ^{6}Li-captured spallation neutrons vs signal amplitude in time coincidence with cosmic muon signals. Neutron captures on ^{6}Li are clearly visible and localized above the gamma band. Source:[92]

where S_0 and S_1 are the ADC integrals of two PMTs. $R(dt)$ should not depend on the total charge, and was shown to have a cubic polynomial fit to dt in Figure 5.9. The geometric mean signal S depends on the total charge of the event, which can be tracked by the neutron captures on ^{6}Li, as shown in the same Figure 5.9. A quadratic polynomial fits well the peak of the distributions of these events.

A relative light collection efficiency to each PMT can be defined as,

$$\eta_0(dt) = \frac{S(dt)\sqrt{R(dt)}}{S(0)\sqrt{R(0)}}, \tag{5.16}$$

$$\eta_1(dt) = \frac{S(dt)\sqrt{R(0)}}{S(0)\sqrt{R(dt)}}, \tag{5.17}$$

with the normalization condition that $\eta_i(0) = 1$. The $\eta(dt)$ can be converted to $\eta(z)$ via the Equation 5.12. An example is also shown in Figure 5.10.

The statistically optimal way to combine into a single E_{vis} is to sum the estimated total number of PE counted by both PMTs, and divided by position-dependent light collection factor,

$$E_{vis} = \frac{S_0 n_0/g_0 + S_1 n_1/g_1}{n_0\eta_0(z_{rec}) + n_1\eta_1(z_{rec})}, \tag{5.18}$$

where S_i is the pulse area from PMT i, g_i is the pulse area signal per E_{vis} deposited at segment center, and n_i is the estimated number of photoelectrons collected per E_{vis} at segment center, and $\eta_i(z)$ is the position-dependent light collection efficiency to each PMT i, and z_{rec} is the reconstructed z-position. The reconstructed position z_{rec} is formed by statistically weighted average of dt and $\ln R(dt)$, which was shown to have degraded position resolution if either information is removed.

5.3.5 Low level calibration performance

Having calibrated the energy, position and PSD, we need to evaluate the stability of these metrics as a function of time. The stability was monitored via a variety of background events present in the physics data-taking runs.

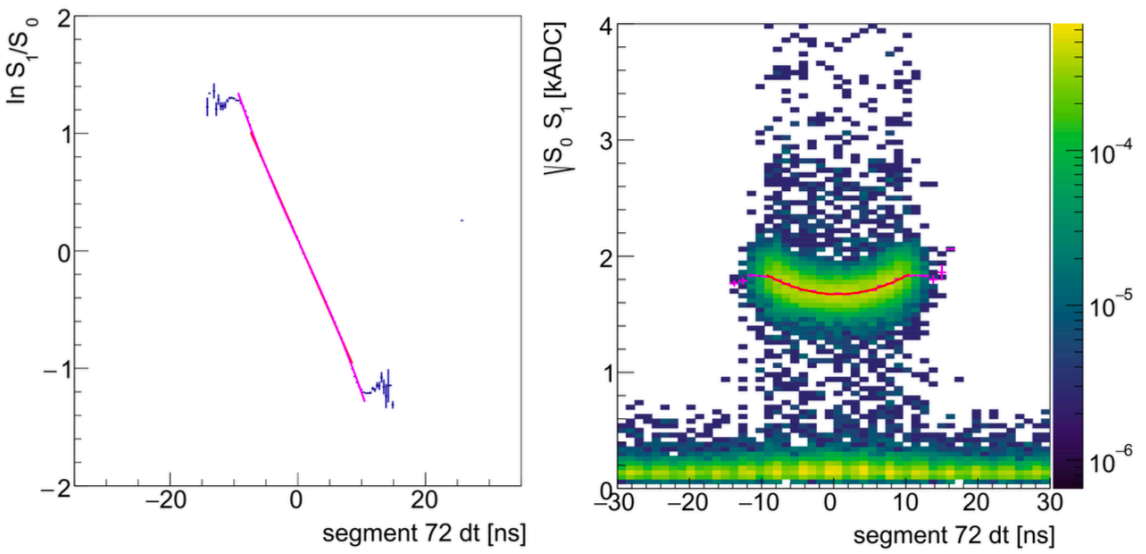


Figure 5.9: Examples of $R(dt)$ and $S(dt)$. Left: $\ln R(dt)$ was fitted to dt in a cubic polynomial fit (magenta), better than a linear fit (red). The data is in blue. Right: S(dt) distribution from neutron captures on ^{6}Li with a quadratic polynomial fit in magenta. Source:[100]

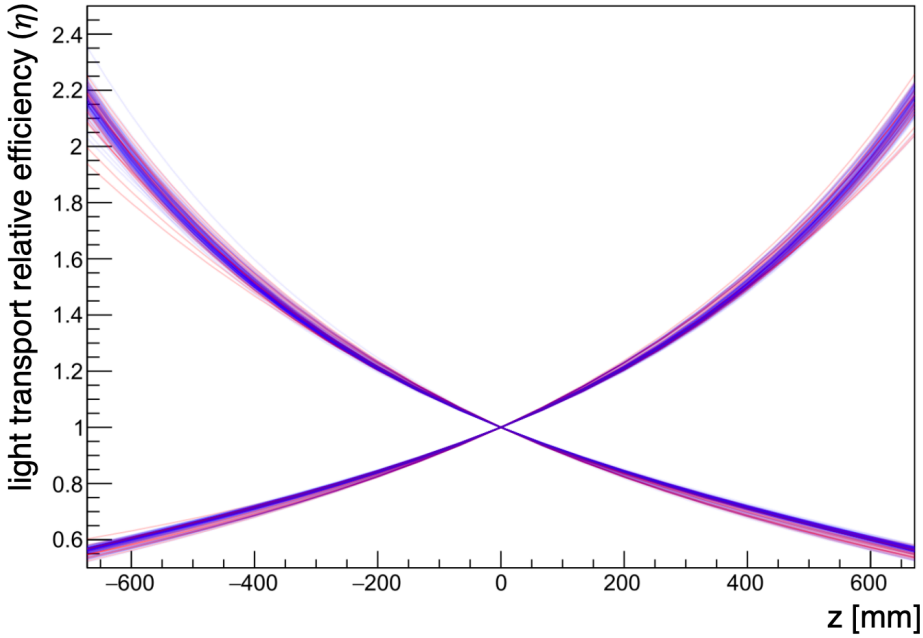


Figure 5.10: An example of z-dependence of light collection efficiency from all Hamamatsu (blue) and ET PMTs (red). Source:[100]

RnPo The PROSPECT ^{6}LiLS was doped with ^{227}Ac, the decay of which contains two successive α-particles,

$$^{219}\text{Rn} \rightarrow^{215} \text{Po} + \alpha \tag{5.19}$$

$$^{215}\text{Po} \rightarrow^{211} \text{Pb} + \alpha \tag{5.20}$$

The α-α coincidence RnPo events are separated by a half life of 1.78 ms. The α-particles are highly quenched and localized. RnPo events are selected by a pair of prompt nuclear recoil of $0.19 < \text{PSD} < 0.36$ and $0.57\ \text{MeV} < E_{rec} < 1.15\ \text{MeV}$ and a delayed nuclear recoil of $0.19 < \text{PSD} < 0.36$ and $0.66\ \text{MeV} < E_{rec} < 1.15\ \text{MeV}$, with a time difference of 5 ms and position distance of 20 cm.

BiPo The decays of ^{214}Bi and ^{212}Bi produce a β followed by an α particle, from the ^{238}U and ^{232}Th decay chains due to natural radioactive contamination in the inner detector.

$$^{214}\text{Bi} \rightarrow^{214} \text{Po} + \beta \tag{5.21}$$

$$^{214}\text{Po} \rightarrow^{210} \text{Pb} + \alpha \tag{5.22}$$

$$^{212}\text{Bi} \rightarrow^{212} \text{Po} + \beta \tag{5.23}$$

$$^{212}\text{Po} \rightarrow^{208} \text{Pb} + \alpha \tag{5.24}$$

^{214}BiPo events are selected by pairs of a prompt electronic recoils of $0.05 < \text{PSD} < 0.22$ and $0.0\ \text{MeV} < E_{rec} < 4.00\ \text{MeV}$ and a delayed nuclear recoils of $0.17 < \text{PSD} < 0.34$ and $0.72\ \text{MeV} < E_{rec} < 1.00\ \text{MeV}$, with a time difference of 0.7 ms and position difference of 20 cm.

^{212}BiPo events are selected by pairs of a prompt electronic recoils of $0.05 < \text{PSD} < 0.22$ and $0.0\ \text{MeV} < E_{rec} < 3.00\ \text{MeV}$ and a delayed nuclear recoils of $0.17 < \text{PSD} < 0.34$ and $0.95\ \text{MeV} < E_{rec} < 1.27\ \text{MeV}$, with a time difference of 1 μs and position difference of 20 cm.

Various clean γ-rays can also be used to monitor the stability. For example, the n-H capture following cosmogenic muon signal emits mono-energetic 2.22 MeV γ-rays. Prominent single γ-ray peaks are also visible in the spectrum, from intrinsic ^{208}Tl contamination in the detector and reactor generated neutron captures of metal in the HFIR complex and the PROSPECT shielding packages.

The time stability of the energy and z-position reconstruction are depicted in Figure 5.11.

5.3.6 Clustering segment pulses to physics quantities

PhysPulse data contains calibrated information such as z position, visible energy, PSD value, timing difference dt, as clearly discussed in the above paragraphs. Physical pulses are scanned and combined into physical clusters if within 20 ns of each other. The prompt and delayed events are identified via a coincidence analysis. Energy and PSD based analysis can identify the particle type, such as electrons, neutron captures, fast neutron recoils.

5.4 Detector energy response

Before we can proceed to real physics cluster event analysis, we need to validate the energy scale model by comparing the simulations of the PROSPECT AD to the calibration data. **PROSPECT-G4** is a GEANT4-based Monte Carlo simulation package specifically programmed for PROSPECT AD [102]. The simulation package contains core properties of the PROSPECT AD, such as detector geometry, particle interaction types and material properties with adjustable parameters. It allows for proper energy scale calibration, characterization of PROSPECT AD performance, determination of detector responses to various particle interactions and detector systematic uncertainties. The calibrations we performed in the previous section was done on a relative energy scale via the measurements of the neutron captures on ^{6}Li

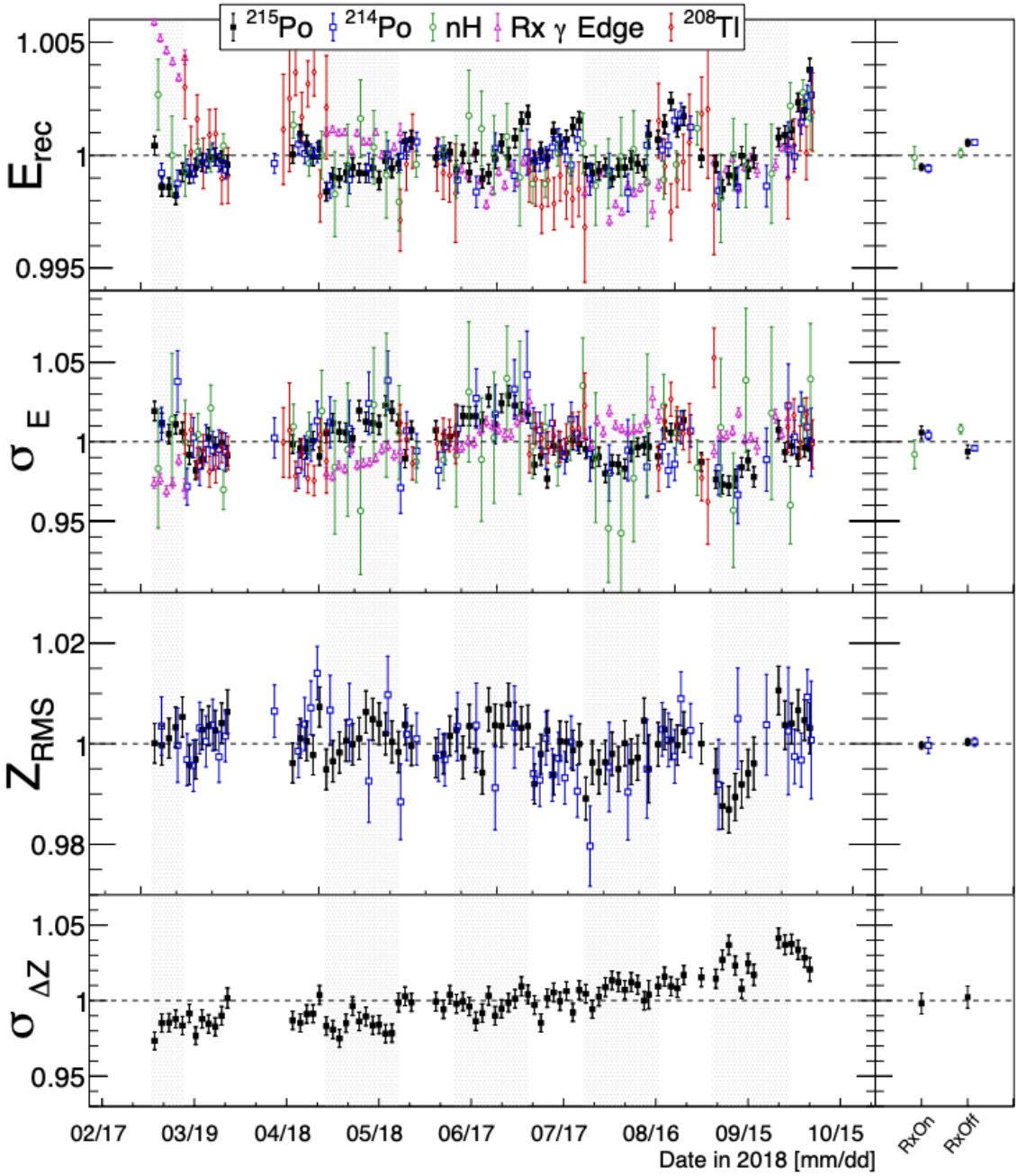


Figure 5.11: Time stability of energy, position and PSD calibration using various background events. Stability over time for both reactor-on and reactor-off. RnPo events in black, ^{214}BiPo events in blue, n-H capture γ-rays in green, reactor neutron capture on metal in pink and ^{208}Tl decay γ-rays in red. Source:[92]

events. An absolute energy scale should be corrected via the calibration of various γ-ray sources and a high energy electron spectrum above 10 MeV. Furthermore, the reconstructed energy spectrum highly depends on effects such as event energy loss, properties of the liquid scintillator, the materials and geometry of the detector. It is thus absolutely necessary to understand the impact of all these factor on the detector energy response via a data-constrained calibration.

In the following paragraphs, we will discuss the procedure and performance of the absolute energy scale calibration. Additional information and discussions are also available in Chapter 8, where a novel external calibration approach is proposed and benchmarked. We start with descriptions of the calibration source used in PROSPECT calibration campaigns, followed by a χ^2-based determination of the detector response model via data-MC comparison, and lastly show the performance of the absolute energy scale calibration.

The PROSPECT experiment had four calibration campaigns since the first detector commissioning in March 2018. The four calibration campaigns were performed in April, August, and December 2018, and in February 2019. The list of calibration sources are shown in Table 5.1.

Typically, the calibration sources were placed at 7 available z-positions along the segment in one of 7×5 calibration source tubes for 5 or 10 minutes runs. The ^{252}Cf and AmBe source are run for more than an hour or overnight due to their low activity. Overnight background data was taken before the start of each calibration campaign day. All the calibration runs were performed during reactor-off period to avoid unnecessary reactor related backgrounds.

During calibration campaigns, the ZLE trigger threshold was set to 10(20) ADC channels for gamma and neutron sources. During analysis, additional 90 keV threshold is also enforced for all segments to resolve the non-uniformity of detector response to low energy events.

Table 5.1: Calibration sources used in PROSPECT experiment.

Source	**Particle type**	**Energy (MeV)**
^{137}Cs	γ-ray	0.662
^{22}Na	γ-ray	2x 0.511, 1.275
^{60}Co	γ-ray	1.173, 1.332
^{252}Cf	neutron	2.223 (n-H capture)
AmBe	neutron	4.4
^{12}B	β^-	3-13.4 MeV

For gamma calibrations with ^{137}Cs, ^{22}Na, and ^{60}Co, a PSD requirement of within 3σ band of the mean PSD value is applied. Overnight background gamma-like rates are subtracted from the calibration runs.

For ^{252}Cf calibrations, we look for time coincident pairs of prompt γ-ray and delayed 2.22 MeV de-excitation γ-ray signal, generated in the subsequent nH capture interaction. The prompt γ-rays are from the ^{252}Cf fissions and have an energy range of 3 MeV to 15 MeV. The time coincidence cut for the pair is 0-200 μs for the correlated and -1200 to -200 μs for the accidental events.

^{12}B events are produced by cosmogenic neutrons via the ^{12}C(n,p)^{12}B interaction. The energy of the emitted electron spectrum is between 3 and 13.4 MeV. The ^{12}B events are selected via pairs of a prompt nuclear recoil and a delayed electronic recoil. The prompt signal has to be within a single segment with a nuclear recoil PSD value, and the energy is between 0.7 MeV and 10 MeV. The delayed signal has an electronic recoil PSD with energy less than 15 MeV and multiplicity ≤ 3. The time difference is between 3 and 30 ms, eliminating neutron captures that exhibit ^{12}B-like pattern. The requirement of the distance between the prompt and the delayed is 12 cm.

The AmBe source provides 4.4 MeV high energy γ-ray via the reaction,

$$\alpha + {}^{9}\mathrm{Be} \rightarrow n + {}^{12}\mathrm{C} + 4.4\mathrm{MeV}, \tag{5.25}$$

where the α particle was emitted from ^{241}Am with an energy of 5.486 MeV for 85% of the time. The AmBe source was not used in the calibration process for the PROSPECT AD. It was only used to validate the final energy scale model. The AmBe events are selected via pairs of a prompt γ-ray and a delayed neutron capture on ^{6}Li. The energetic neutron produced in the reaction will mix with the prompt γ-ray as a prompt nuclear recoil, thus exclusion of proton recoils in the prompt signal is added.

The γ-rays produced from the calibration sources can hit multiple segments in the PROSPECT AD. The number of segments that contains deposited energy from

γ-rays, referred as multiplicity, is a crucial variable for highly segmented detectors, since it's highly correlated with detector energy loss due to dead or inactive materials inside the detector. The multiplicity distribution will also be included in the energy scale calibrations.

The non-linearity energy scale model in **PROSPECT-G4** MC packages are described in Section 5.2, Equation 5.7, and Equation 5.8. The energy of Cherenkov light is also added as part of the total energy,

$$E_{ckov} = k_c \sum_{\lambda} N_\lambda E_\lambda, \tag{5.26}$$

where N_λ is the number of photons per wavelength, E_λ is the energy of the photon, and k_c is the effective light collection efficiency. The energy scale model is determined by minimizing the χ^2 between the calibration data and simulations, which is also used in Chapter 8.

$$\chi^2_{\text{data-MC}} = \sum_{\gamma} \chi^2_\gamma + \sum_{\text{multi}} \chi^2_{\text{multi}} + \chi^2_{^{12}\text{B}}, \tag{5.27}$$

The best-fit energy scale model reproduces the spectrum and multiplicity of the calibration sources, as shown in Figure 5.12. The best-fit parameters are (A, k_{B1}, k_{B2}, k_c) = (1.0026±0.004, 0.132±0.004 cm/MeV, 0.023±0.004 cm^2/MeV^2, 37±2%), with a total χ^2/ndf = 581.5/420.

The agreement between the measured and predicted MC response is also illustrated in Figure 5.13 below.

We mentioned that the AmBe source was not used for determining the energy scale model but only used for energy scale model validation, this is shown in Figure 5.14.

The energy resolution is characterized for the calibration γ-ray sources, with the following function:

$$\frac{\sigma_E}{E_{rec}} = \sqrt{a^2 + \frac{b}{E_{rec}} + \frac{c^2}{E^2_{rec}}}, \tag{5.28}$$

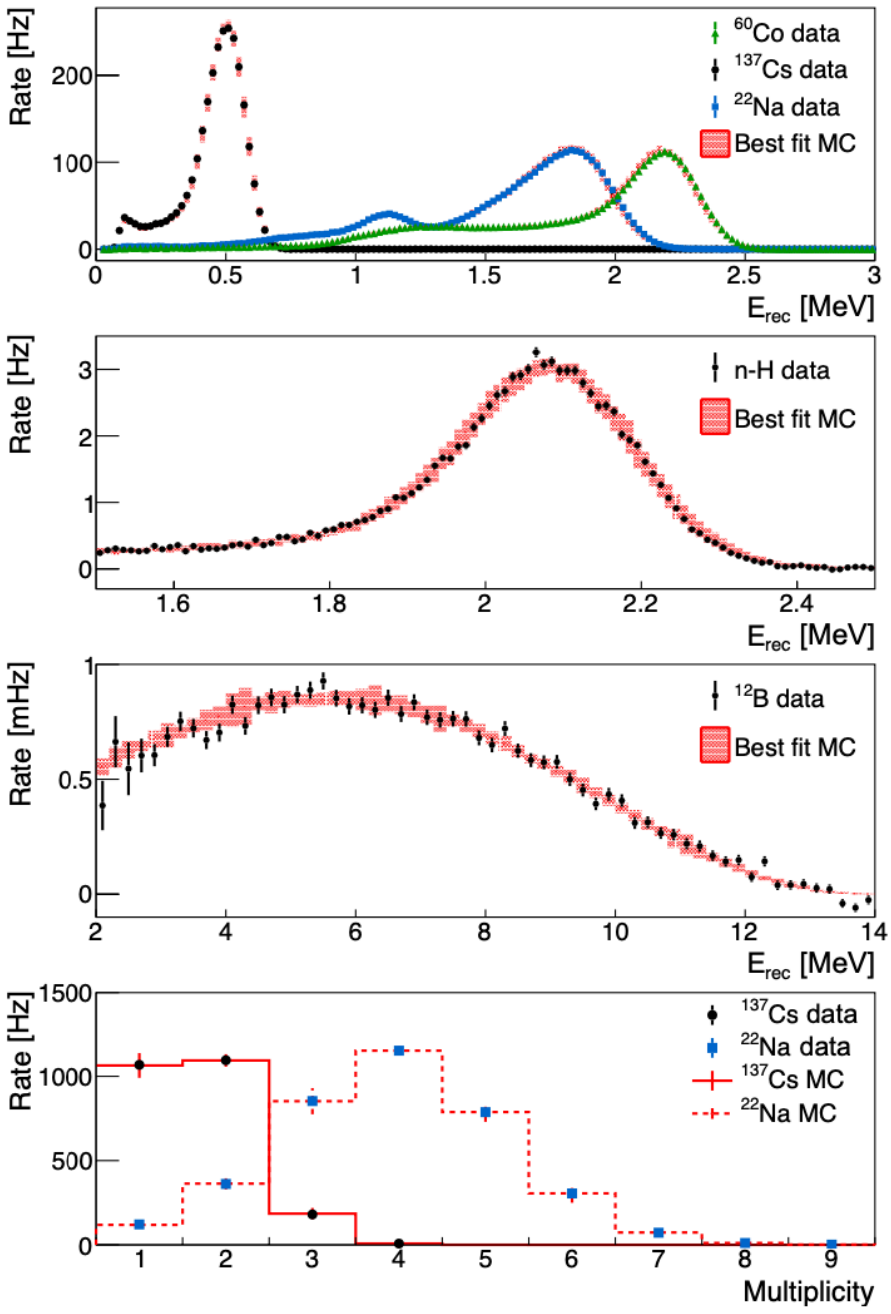


Figure 5.12: Best-fit energy scale model comparisons with calibration data. Source:[92]

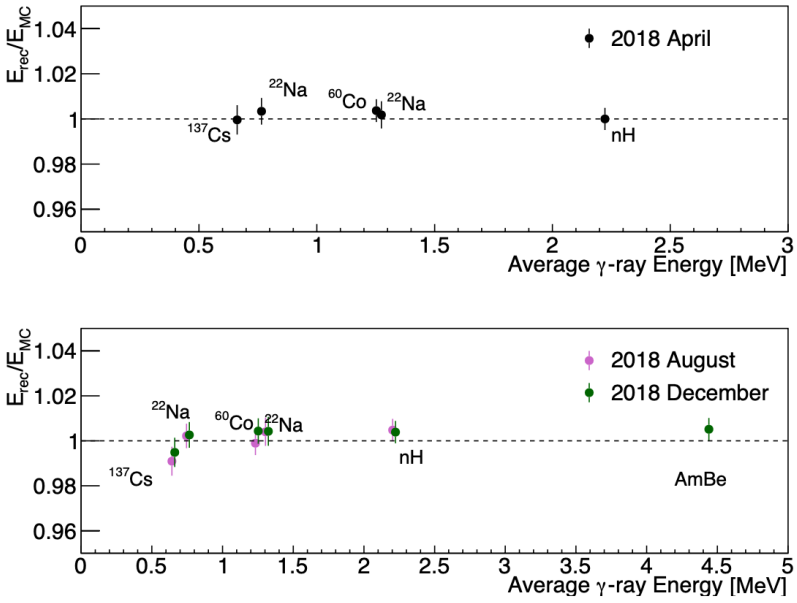


Figure 5.13: Ratio of γ-ray calibration between data and best-fit simulation. Top: calibration sources used in energy scale model determination; Bottom: ratio of calibration source in from all campaigns. Source:[92]

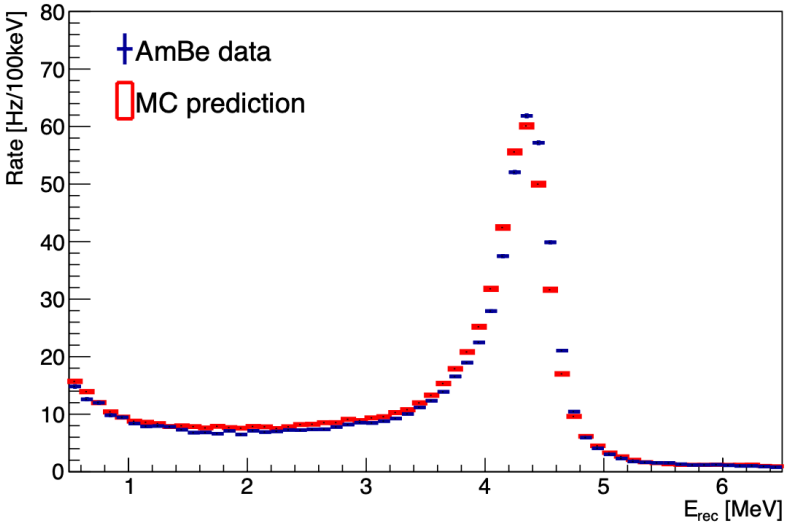


Figure 5.14: Spectrum comparison between data and best-fit energy scale model for AmBe source. Source:[92]

where a represents on detector configuration, b is related to photostatistics (PE/MeV), and c is related to the PMT and electronics noise. The best-fit energy resolution is shown in Figure 5.15, corresponding to a 4.8% energy resolution at 1 MeV. The best-fit parameters are (a,b,c) = (1.15%±0.47%, 4.61%±0.24%, 0.0±1.3%).

A detector energy response matrix can be generated using the simulation packages. The detector response converts the incident neutrino energy distribution in the neutrino energy space to the visible energy distribution. Such response matrix is generated via feeding slices of mono-energetic neutrinos through the detector response. The generated prompt reconstructed visible energy of each slice of mono-energetic neutrinos are combined into a matrix in the form of column vectors. Since the energy threshold of neutrinos in the IBD process is 1.8 MeV, the response matrix starts from the 1.8 MeV threshold, as shown in Figure 5.16.

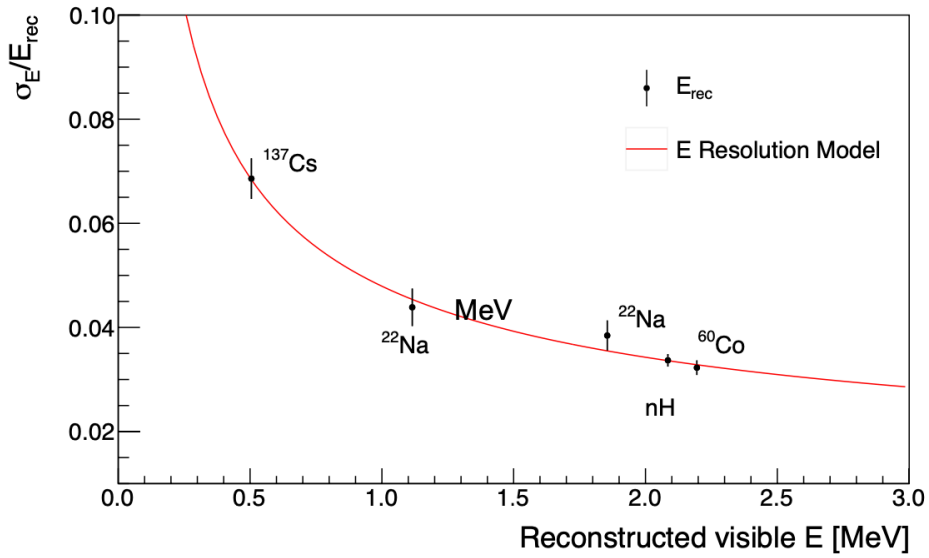


Figure 5.15: The best-fitted energy resolution from calibration sources. Source:[92]

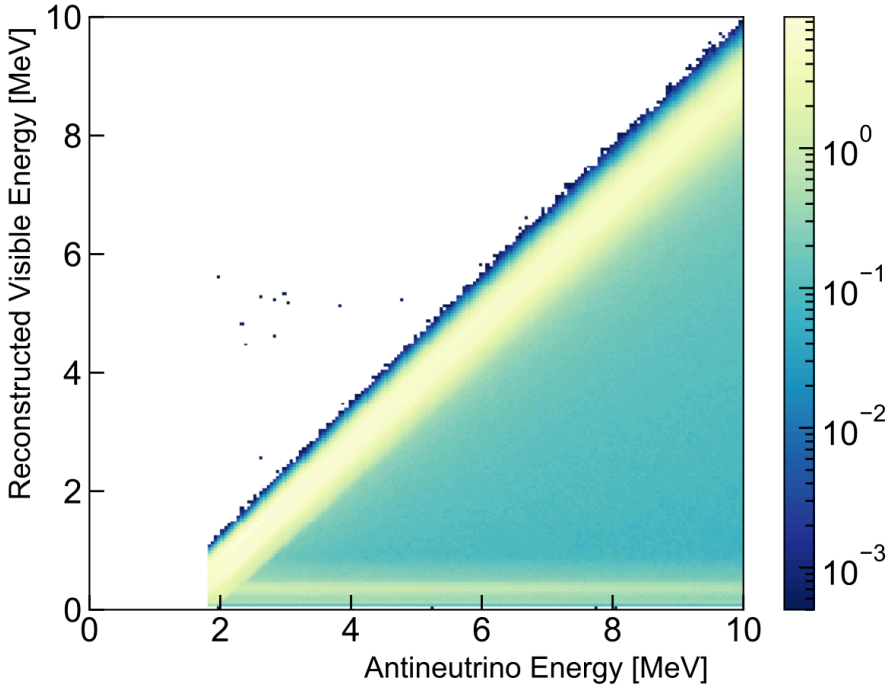


Figure 5.16: The PROSPECT AD response matrix that converts incident neutrino spectrum to prompt visible energy spectrum. Source:[92]

Chapter 6

Optimization of neutrino event reconstruction and PROSPECT-I physics results

In Chapter 5, we gave a detailed description of the absolute energy scale calibration and selection of a variety of background events to monitor the performance of the detector calibration. With accurate calibrations applied to **DetPulse**, the resulting **PhysPulse** data contains calibrated information such as z position, visible energy, PSD value, timing difference dt, as clearly discussed in the previous chapter. Physical pulses are scanned and combined into physical clusters if within 20 ns of each other. Then, the prompt and delayed events are identified via a coincidence analysis. Energy and PSD based analysis can identify the particle type, such as electrons, neutron captures, and fast neutron recoils.

In this Chapter, I continue to discuss the details of a window-based selection cut analysis of IBD event identifications. The optimization process of the selection cuts is presented. The spectrum and oscillation physics results based on the optimal IBD dataset are highlighted.

6.1 IBD event selection cuts

The PROSPECT IBD selection and analysis were performed via a plugin-based **PROSPECT2x_Analysis** toolkit. The **PROSPECT2x_Analysis** offers a plugin-based platform for various high-level analyses. The IBD selection analysis was performed by feeding **PhysPulse** pulse information into the **P2kIBDPlugin** plugin program via a cut-based analysis. Reconstructed IBD pair information are stored in **IBDClusters** in **ROOT TTree** format, containing information such as event number, reconstructed visible energy E_{vis}, the segment number and energy of the maximum deposition E_{max}, xyz-position, and the correlated neutron captures.

Estimated from the dimension of the PROSPECT AD and neutrino flux of HFIR reactor, less than 1,000 IBD interactions per day were expected in the active target volume during the reactor-on period. These IBDs co-exist with intense reactor related and cosmogenically-induced backgrounds. Highly efficient selection cuts were developed and optimized to greatly suppress the backgrounds while keeping IBD signals minimally ruled out. In the following paragraphs, we outline the selection criteria based on energy and PSD of the event clusters, the time coincidence of the prompt and delayed clusters, the topology of IBD positron and neutron pair, and the target volume. The power of selection cuts are best illustrated in Figure 6.1.

Prompt cuts The positrons produced in the IBD reaction take away most of the kinetic energy of incident neutrinos and will deposit energies in the detector up to 8 MeV in multiple numbers of segments, with the highest energy deposition usually happening in the same segment where IBDs take place. Thus, the prompt cuts consisted of E_{rec} energy cut between 0.8 and 7.2 MeV, and reconstructed PSD values all within the 2.0σ band of the calibration electron-like PSD mean.

Delayed cuts The neutron produced in the IBD reaction usually contains less than a few tens of keV of kinetic energy and produces negligible scintillation light as it thermalizes. The neutron capture on ^{6}Li happens within roughly 50 μs and a

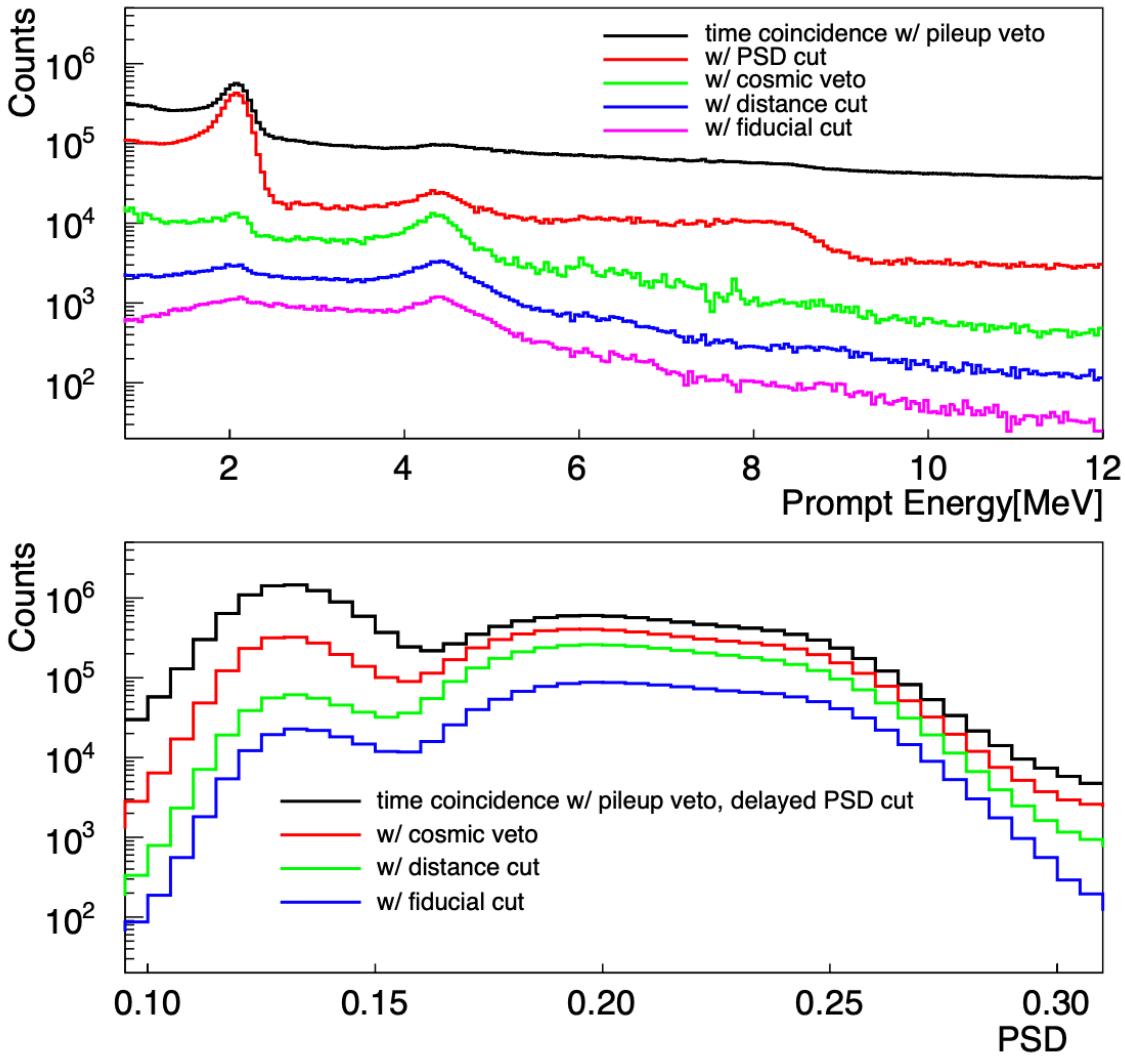


Figure 6.1: Illustrations of sequential application of IBD selection cuts in the reconstructed energy and PSD space.

few tens of centimeters away from the IBD interaction vertex, producing a highly quenched total visible energy of 0.526 MeV. The n-^{6}Li capture tracks are usually within micrometers away from the neutron capture vertex, resulting in scintillation light emitted in a single segment. The delayed cut is required to be a single-pulse cluster that is consistent with the energies and PSD values of n-^{6}Li, which was defined by cosmogenic n-^{6}Li capture events. The n-^{6}Li requires E_{rec} energy to be within $\pm 3\sigma$ of the mean value of 0.526 MeV and PSD values within $\pm 2\sigma$ of the PSD mean value.

The particle identification of the prompt electron-like events and the delayed neutron-like events are illustrated in the PSD vs energy Figure 6.2.

Prompt and delayed coincidence cuts Correlated prompt and delay clusters defined above need to meet a time and position difference requirement to be seen as products of the same IBD interaction. This delayed cluster is required to occur within 120 μs of the prompt cluster. The delayed cluster is also required to travel no further than segments vertically/horizontally adjacent to the primary segment in which the prompt clusters happen. If they happen in the same segment, the prompt-delayed Z_{rec} difference is required to be less than 140 mm; and if they happen in the adjacent segments, the prompt-delayed Z_{rec} difference is required to be less than 100 mm.

A set of background cuts are introduced to remove events associated with cosmogenic muons and muon-induced events that resembles delayed clusters.

Muon vetos Muon tracks traversing the PROSPECT AD usually deposit large amount (> 15 MeV) of scintillation light and induce showers of fast and slow neutrons. IBD candidates then are rejected if their delayed cluster is within 200 μs of a preceding cluster with E_{rec} greater than 15 MeV.

Neutron veto and recoil veto Similarly, cosmogenically generated fast and slow neutrons are removed if the delayed clusters of IBD candidates occurs within 400 μs of another n-^{6}Li event or within 250 μs of a preceding cluster with E_{rec} greater than

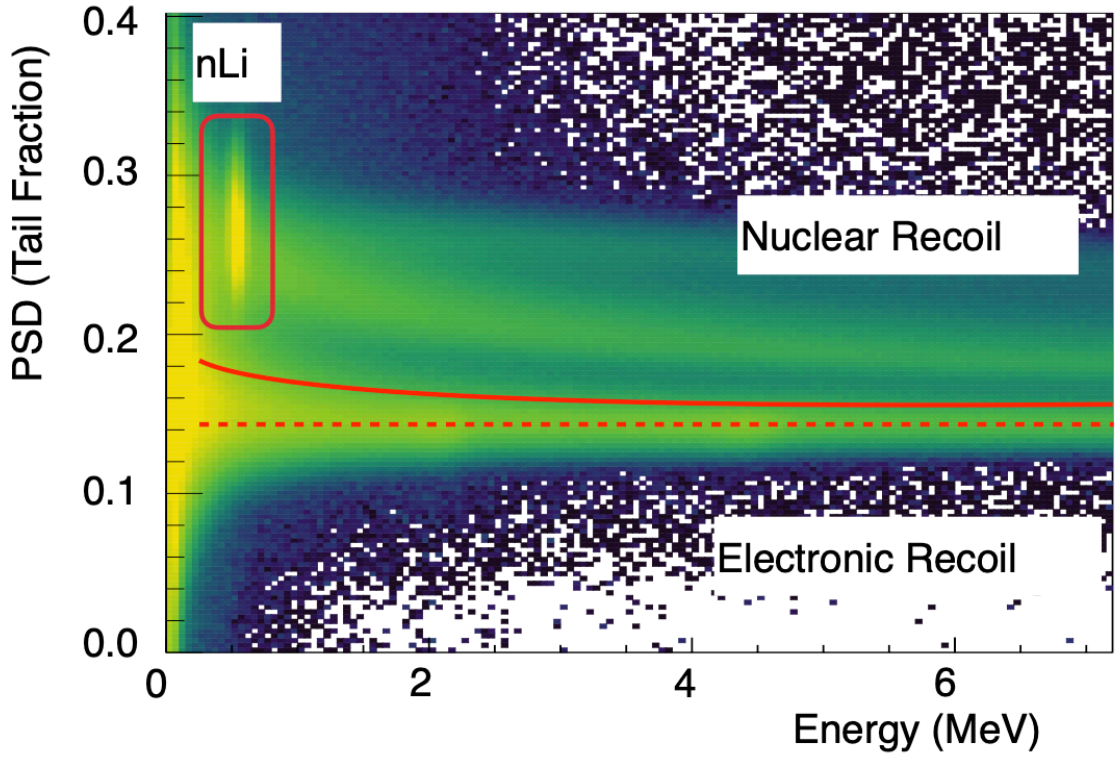


Figure 6.2: Illustration of the various particle types in PSD vs E space, allowing identification for prompt and delayed IBD products. Neutron captures on ^{6}Li are concentrated in the red box. The additional high PSD band is likely caused by recoils of heavier charged particles other than protons. Adapted from [76].

0.25 MeV and contains at least one pulse with a PSD larger than 2σ above mean of the electron-like PSD mean.

Pile-up veto Pile-up veto removes IBD candidates if either of the clusters is within 0.8 μs of a previous cluster, reducing ambiguities in the calculation of trigger-related dead times.

Fiducialization cut Simulations of cosmogenic backgrounds indicate high neutron-related background on the outer layer of the segments, shown in Figure 6.3. Thus, IBD candidates are rejected if either of the clusters is located outside the defined fiducial volume. Similarly, a fiducial layer of 140 mm thick is defined near both ends along the segment length.

Accidental IBD pairs Accidental pairs of IBD-like candidates can occur due to high rates of single γ-rays and neutrons. To measure accidental prompt and delayed events, an off-time window that is 100 times large than the IBD pair time windows are used to provide high statistics. The measured accidental IBD-like rates in the off-time window are properly scaled back and subsequently subtracted off from the IBD candidate rates.

The IBD selection cuts defined in the above paragraphs can be summarized in Table 6.1.

6.2 IBD cut optimization

The IBD selection cuts defined in the above paragraphs are the optimized values via a comprehensive study. The optimized selection is based on 20% evenly sampled of the whole dataset to avoid biasing the selection cuts. The final IBD spectrum was revealed until the selection cuts were optimized and frozen.

The optimization procedure is based on three important metrics, the number of IBD events, the signal to background ratio, and the effective IBD counts. The

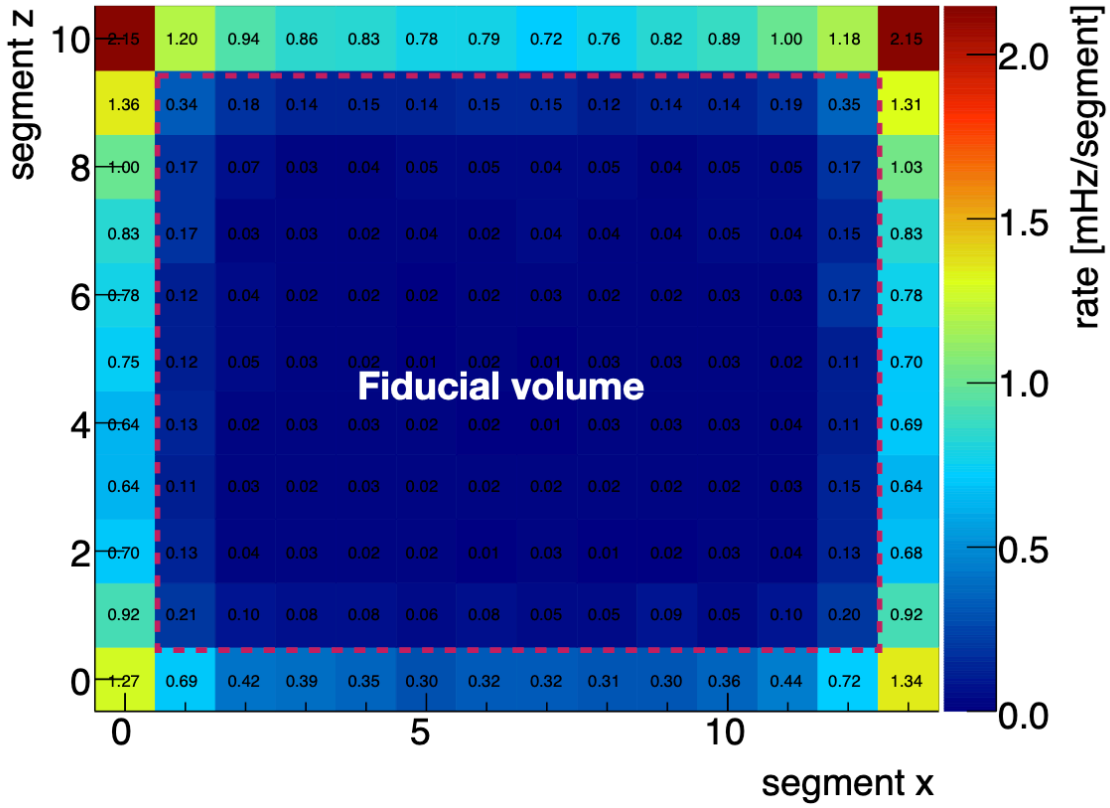


Figure 6.3: Illustration of the fiducial volume to reduce to cosmogenic backgrounds. Segments with higher cosmic ray related neutron rates are excluded in the IBD selection. A 140 mm fiducial layer is also defined along the length of the segment. Adapted from [76].

Table 6.1: Summary of IBD selection cut values

Selection cuts	**Value**
Prompt	$0.8 < E_{rec} < 7.2$ MeV
	PSD within 2.0 σ band of electron-like PSD mean
Delayed	E_{rec} within 3.0 σ of 0.526 MeV
	PSD within 2.0 σ band of n^6Li capture PSD mean
Time coincidence	0 μs $< dt <$ 120 μs
Distance coincidence	$<$ 140 mm for the same segment
	$<$ 100 mm for the adjacent segment
Muon veto	$<$ 200 μs
Neutron veto	$<$ 400 μs
Recoil veto	$<$ 250 μs
	contains pulses $> 2\sigma$ band of electron-like PSD mean
	$E_{rec} > 0.25$ MeV
Pile-up veto	$<$ 0.8 μs
Fiducialization	Segment list:(0, 1, 2, 3, 4, 5, 6, 7, 8, 9,
	10, 11, 12, 13, 17, 18, 21, 23, 24, 27, 28,
	29, 31, 32, 34, 36, 40, 41, 42, 43, 44, 46, 47,
	48, 50, 52, 55, 56, 60, 63, 68, 69, 70, 73, 79,
	83, 86, 87, 94, 97, 102, 107, 111, 115, 121, 122,
	126, 127, 128, 130, 133, 136, 139, 141)

former two metrics are self-explanatory and the effective IBD counts are defined in the following expression and provide a background-free estimate of the statistics of the dataset.

$$N_{eff} = \sum_{0.8}^{7.2\text{MeV}} (N_i/\sigma_i)^2, \tag{6.1}$$

where σ_i and N_i are the statistical uncertainty and bin content of the IBD energy spectrum obtained from 20% of the whole dataset evenly sampled. The summation range is from 0.8 MeV to 7.2 MeV, with 0.2 MeV bin size. The N_{eff} metric is proportional to $\sim$ N signal with background subtracted, thus representing a background-free measure of the statistical power of the dataset used for the optimization process, and is the main metric among the three. The signal to background ratio and the number of IBD events are secondary metrics when there is not much gain in effective IBD counts.

The effective counts based optimization process is independently accompanied and cross-checked by another Figure of Merit (FOM) analysis. The FOM analysis maximizes the two FOMs instead of effective counts,

$$FOM_1 = A_{IBD}/A_{nH}, \tag{6.2}$$

$$FOM_2 = A_{IBD}/A_{nC}, \tag{6.3}$$

where A_{IBD}, A_{nH} and A_{nC} stands for the area in IBD energy spectrum between 0.8 and 7.2 MeV, the area of reactor-off background counts around two prominent peaks, nH for neutron captures on hydrogen (1.8-2.2 MeV) and nC for neutron inelastic scattering on carbon (4.0-5.0 MeV). This alternative metric offers similar background-divided IBD counts.

Note that the optimization process for all the cuts were performed without taking into account the correlations. While a correlated approach would provide a more accurate topological profile of the IBD parameter phase space, the uncorrelated approach provides competitive statistics yet takes much less time and does not need to

deal with the complexity from the correlated selection cut parameters. Even though the optimization processes each selection cut parameter independently, the rest of the parameters used in the optimization process were good approximations of the physics properties of the IBD process. Thus, the uncorrelated approach of the optimization process provides competitive parameter estimates of the global best-fit minimum or maximum.

In the following paragraphs, we provide the results of each parameter optimization in the same order they were described in the previous section.

Prompt cuts The prompt cuts were varied from 1.0 σ to 3.0 σ in steps of 0.5 σ. The optimal value prompt PSD value of 2.0 σ were found to provide the best effective counts per day, as shown in Figure 6.4.

Delayed cuts The delayed cuts for the n^6Li capture events were varied from 2.4 to 3.4 σ for the energy and 1.2 to 2.2 σ for the PSD value. The optimal E cut was selected as 3.0 σ because it offered the best signal to background despite no obvious gains in effective counts and IBD counts were found. The effective count rates were shown in Figure 6.5.

The optimal PSD cut was selected as 2.0 σ because it provided more IBD counts and better signal to background ratio yet similar effective counts compared to the 1.8 σ case. The effective count rates were shown in Figure 6.6.

Prompt and delayed coincidence cuts The prompt and delayed time coincidence cut was already well optimized at 120 μs, as shown in Figure 6.7.

The prompt and delayed distance coincidence cut in the same or adjacent segment were mainly driven by the nH FOM from the other optimization analysis. The tighter cuts were selected as (140,100) mm to increase effective counts while providing better signal to background ratio in the nH/nC regions as shown in Figure 6.8 and 6.9.

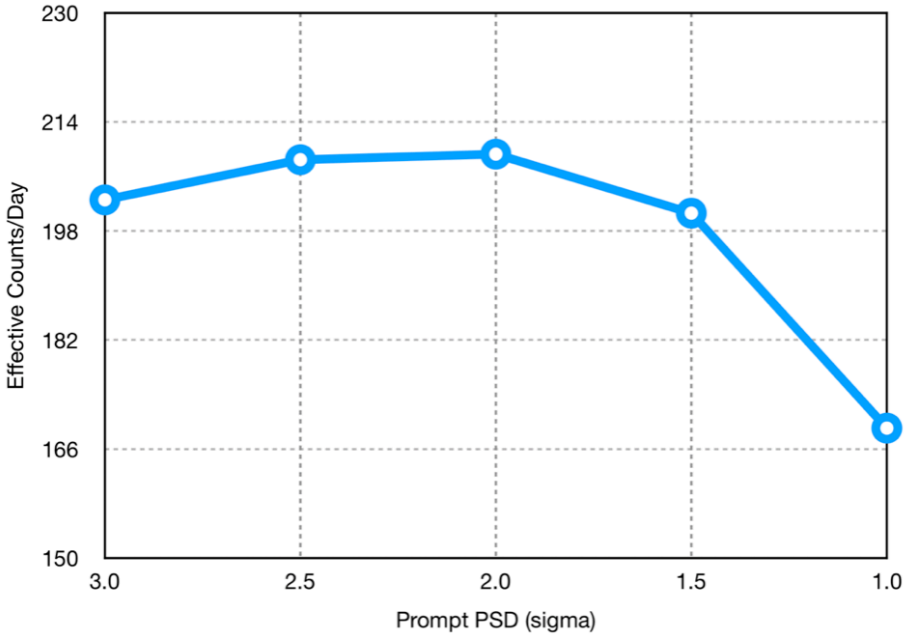


Figure 6.4: Prompt PSD optimization

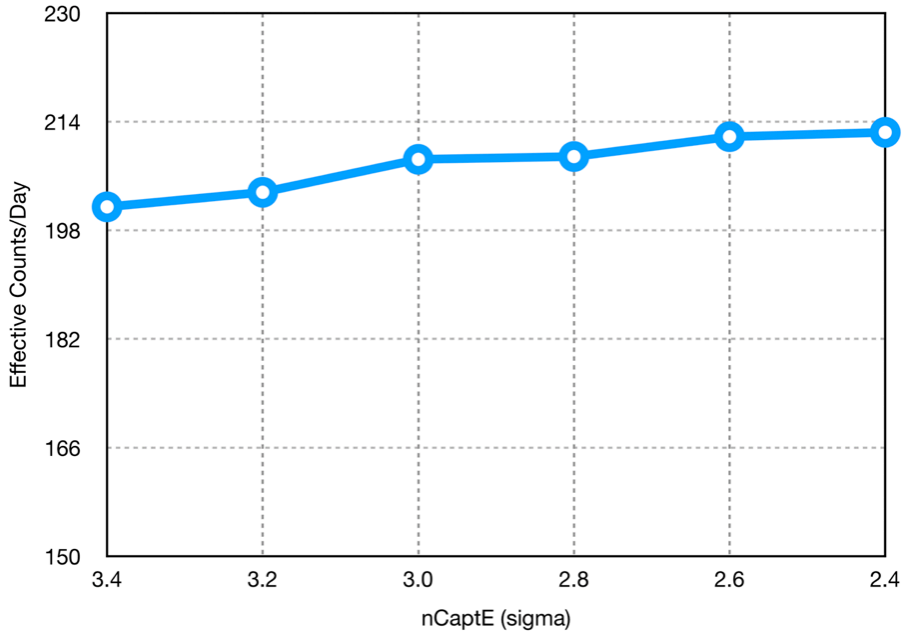


Figure 6.5: Neutron capture E cut optimization.

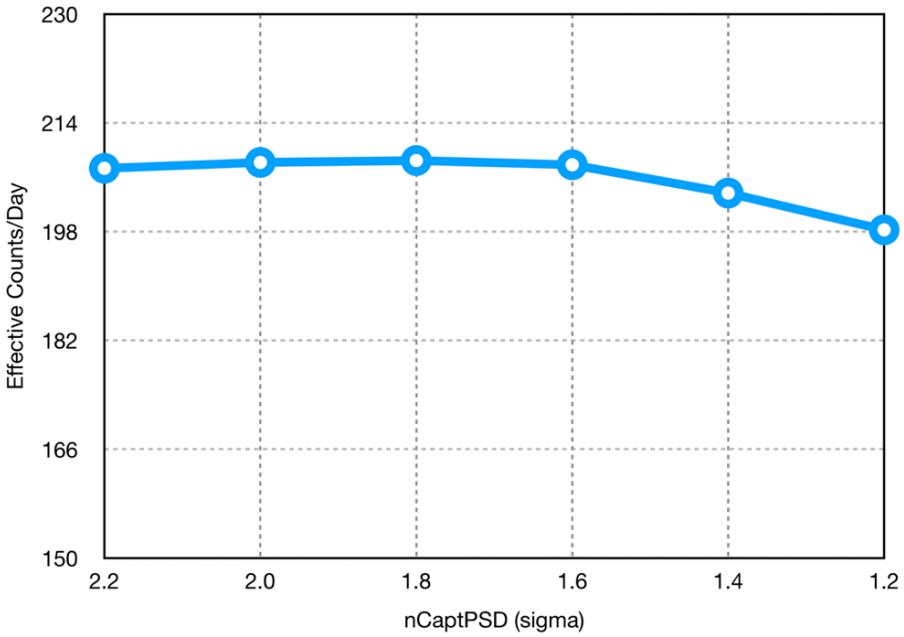


Figure 6.6: Neutron capture PSD cut optimization.

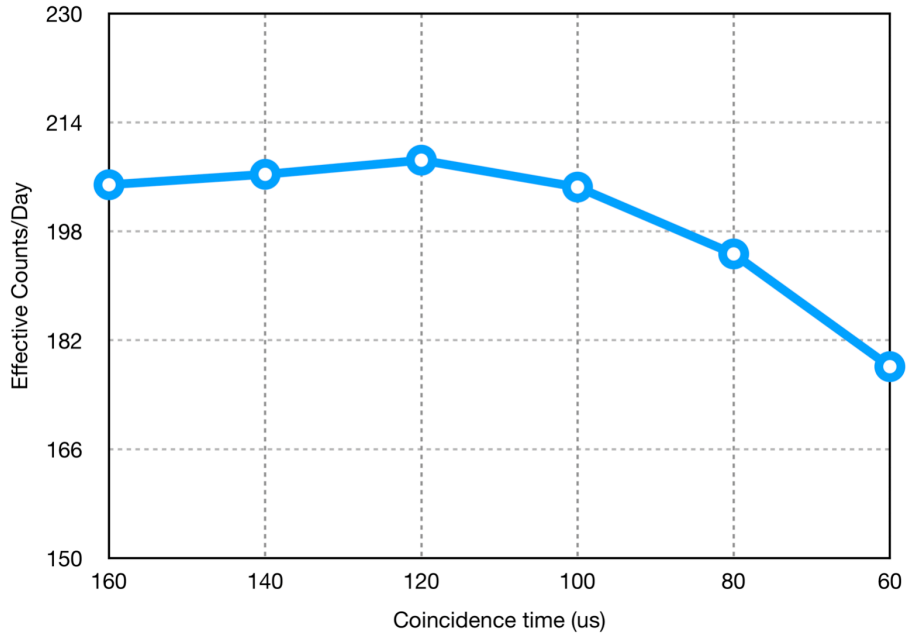


Figure 6.7: Prompt and delayed timing coincidence cut optimization.

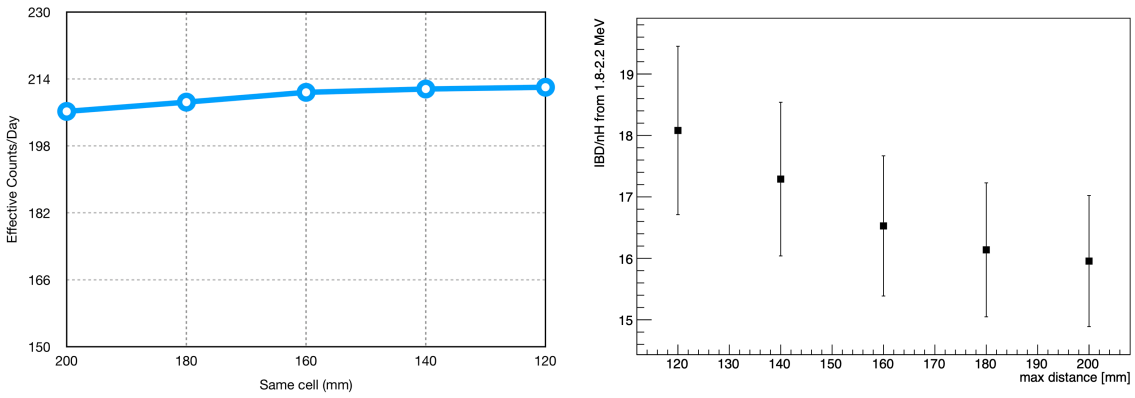


Figure 6.8: Prompt and delayed distance coincidence cut optimization in the same segment. The right plot shows signal to background ratio in the nH region.

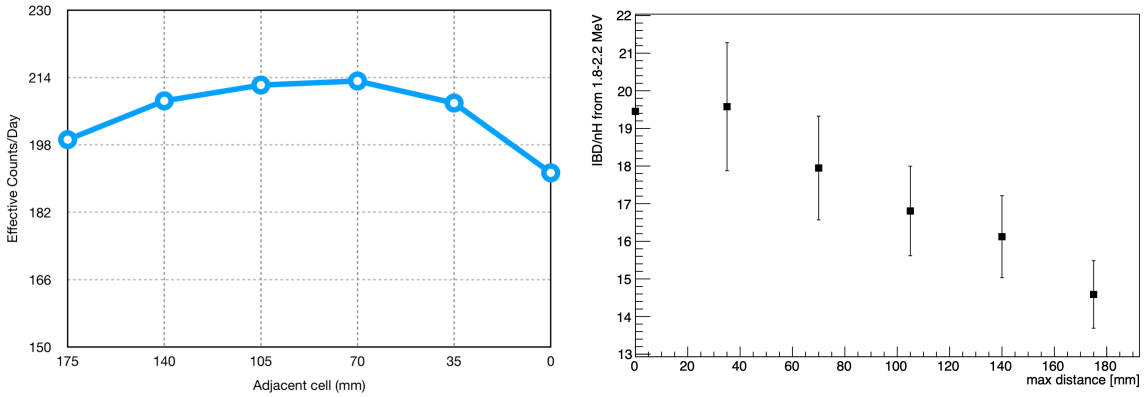


Figure 6.9: Prompt and delayed distance coincidence cut optimization in the adjacent segment. The right plot shows signal to background ratio in the nH region.

Muon vetos The muon veto timing cut were selected as 200 μs, having diminishing returns beyond 200 μs, as shown in Figure 6.10. Further increasing the time window would decrease the effective counts since more IBD events were excluded after any muon tracks.

Neutron veto and recoil veto The neutron veto cut was set at 400 μs where it provided more IBD counts despite having similar effective counts, as shown in Figure 6.11. The recoil veto cut was set at 250 μs, mainly determined by the nH FOM as shown in Figure 6.12.

Pile-up veto The pile-up veto cut was mostly dominated by event rates, with 800 ns selected to account for the 2% reactor-on and 1% reactor-off trigger dead-time.

Fiducialization cut The fiducialization cut has a (x,y)-plane and z component. Along the z-direction, $\pm$444 mm was used to provide a layer of fiducial layer with thickness matching the cross-sectional dimension of each segment. Thus, the value was selected from the point of view of providing a consistent thickness of fiducial layer. In the (x,y) fiducial volume optimization, a special analysis was performed. We started off with the whole target volume, and picked the worst segment in terms of signal to background ratio, i.e. the background contaminated segment, as one of the non-fiducial segments. Each time a dirty segment was selected as a non-fiducial segment, the effective counts of the fiducial volume increases. The process was repeated until the effective counts of the fiducial volume stopped increasing. The fiducial segments and the optimization process are illustrated in Figure 6.13.

To summarize the optimization we showed above, the optimization process of the selection cuts, in essence, were the optimization process of balancing between gaining more background rejection capability and not losing much IBD signals.

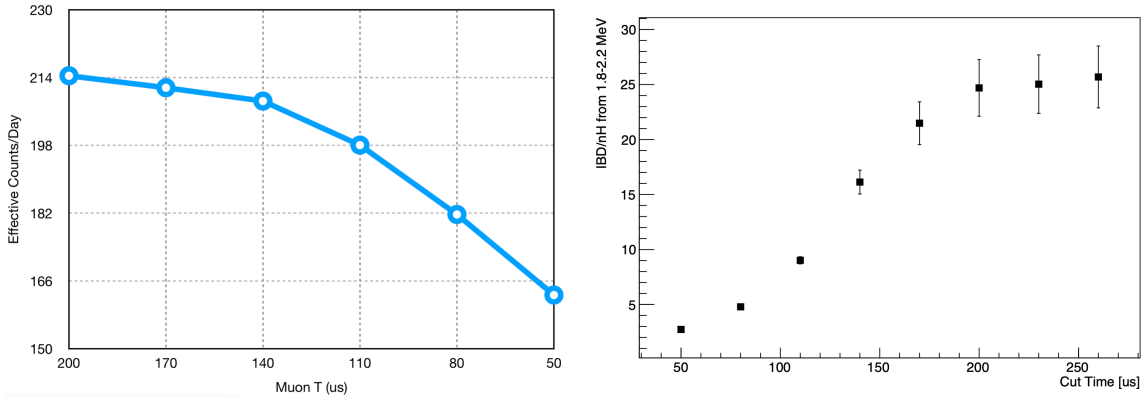


Figure 6.10: Muon veto cut optimization. The right plot shows signal to background ration in the nH region.

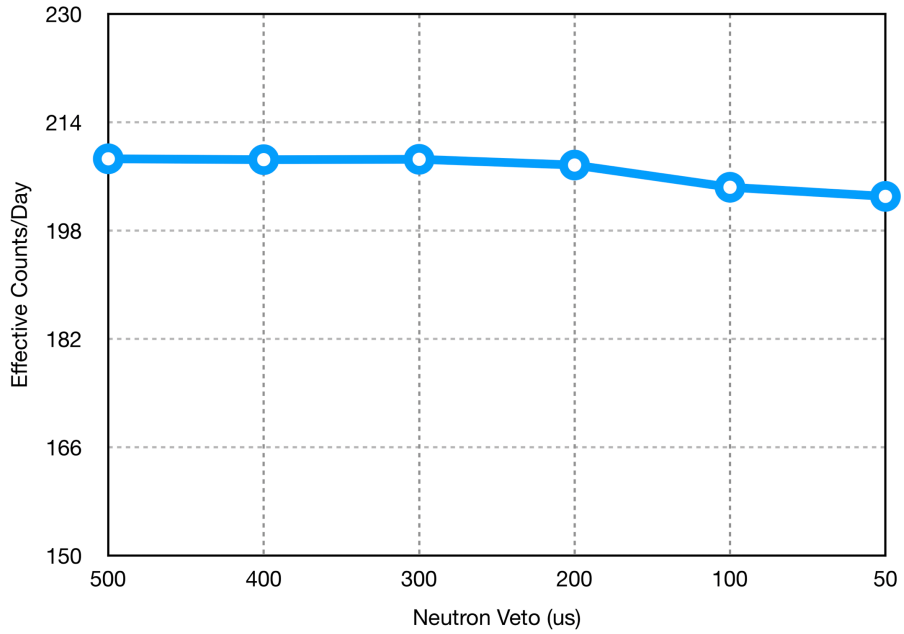


Figure 6.11: Neutron veto cut optimization. The 400 μs cut provides the most IBD counts.

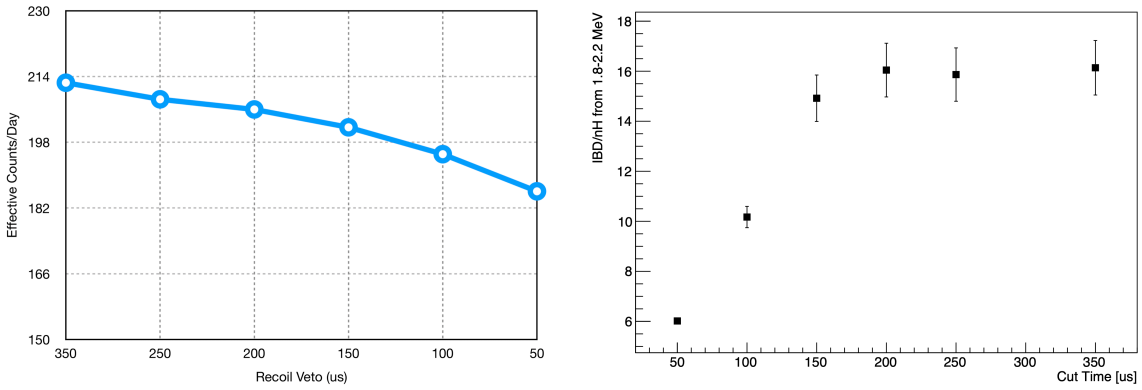


Figure 6.12: Recoil veto cut optimization. The right plot shows signal to background ration in the nH region.

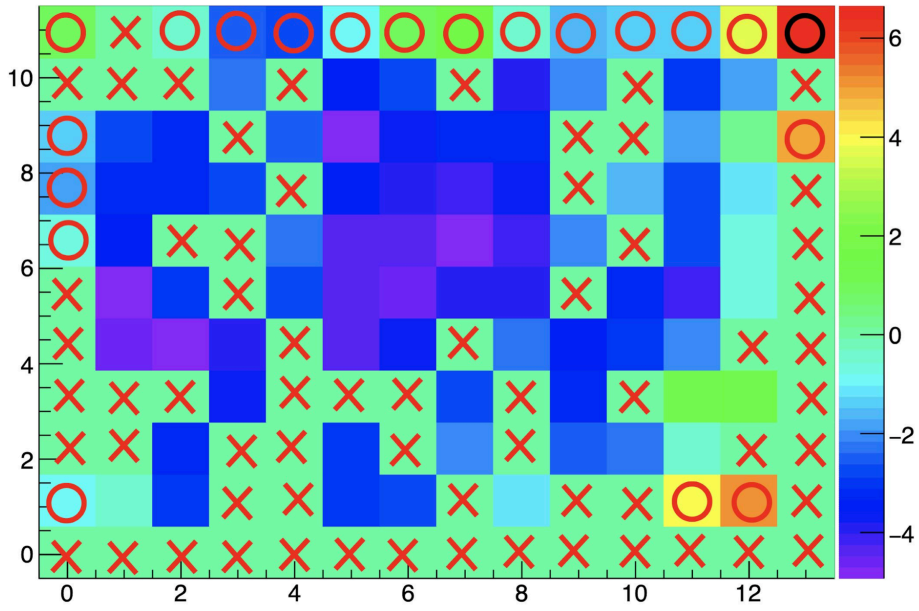


Figure 6.13: The segment lists of the fiducial volume. The segments marked by cross are turned off due to PMT failures. The segments marked by circle are excluded by the optimization process. The color bar represents the change of effective counts if the segment was fiducialized.

6.3 IBD prompt energy spectrum and cross-checks

In this section, we apply the optimized IBD selection cuts to the **PhysPulse** data via the **P2kIBDPlugin** program, and convert them to **IBD TTree** in **ROOT** format. The final IBD energy spectrum is a result of the summation of all the reactor-on histograms with background subtractions and atmosphere-corrected reactor-off histograms and accidental subtractions, as shown in Figure 6.14.

$$\begin{aligned}\text{Total IBD signal} = &\sum_{\text{files}} \Big(\text{hCorrelated}^{\text{f}} - \text{hAccidental}^{\text{f}}/\text{acc} * x^{\text{f}}\Big)^{\text{f} \in \text{RxOn}} \\ &- \frac{\text{livetimeOn}}{\text{livetimeOff}} * \text{atm_scale} * \Big(\text{hCorrelated}^{\text{f}} - \text{hAccidental}^{\text{f}}/\text{acc} * x^{\text{f}}\Big)^{\text{f} \in \text{RxOff}}, \quad (6.4)\end{aligned}$$

where acc stands for the accidental rate scaling of value 100, livetimeOn/livetimeOff stands for the detector live time correction between reactor-on and reactor-off, atm_scale stands for the atmosphere correction of the reactor-off relative to the reactor-on, and x^{f} stands for the additional dead-time correction for accidental rates, defined as, $x^{\text{f}} = \frac{\text{runtime}^{\text{f}}}{(\text{runtime}^{\text{f}} - \text{prompt}^{\text{f}})} \times \frac{\text{runtime}^{\text{f}}}{(\text{runtime}^{\text{f}} - \text{delay}^{\text{f}})}$.

The nominal reactor-off cosmogenic normalization scaling factor atm_scale of 1.00±0.03% is the ratio of the average reactor-on atmospheric pressure over the reactor-off average, accounting for the time-dependence of cosmic-related backgrounds [103].

The whole dataset is from 95.7 (73.1) calendar days of reactor-on (-off). The IBD candidates were selected from 82.2 (65.2) days of reactor-on (-off) live-time. During the reactor-on data-taking period, a total of 115852 IBD candidates are selected, 28358±18 of these are accidental backgrounds, yielding a total of 87494±341 correlated IBD candidates. The reactor-off period contains 1309±4 accidental background events and 29258±175 correlated IBD-like candidates. After applying live-time and atmospheric pressure corrections, this reactor-off IBD candidate corresponds to a total 36934±221. After reactor-off subtraction, a total of 50560±406 signal IBD events were reported. The ratio of IBD signal to cosmogenic background

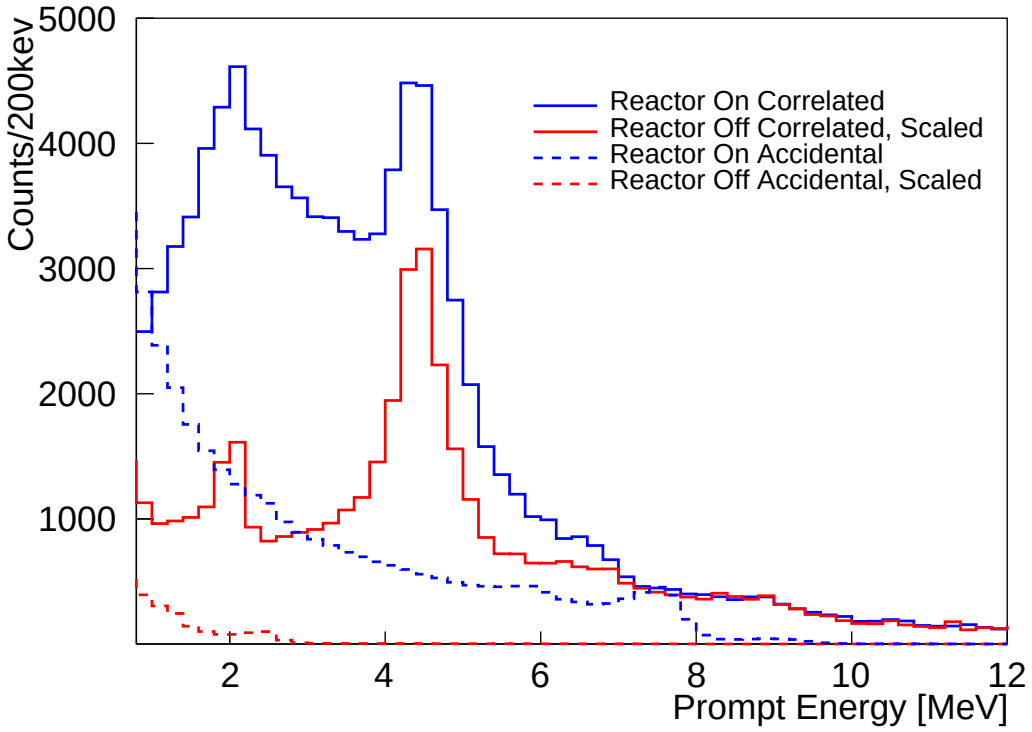


Figure 6.14: The measured reconstructed prompt energy spectrum of reactor-off/on correlated and accidental candidates up to 12 MeV to show three main contributions from n-H capture, nC inelastic scattering and a variety of neutron processes. Scaled accidental events are plotted in corresponding colors for reactor on and off.

(accidental background) events is estimated to be 1.37 (1.78). A summary of IBD candidate is provided in Table 6.2. Figure 6.15 shows the reconstructed IBD prompt spectrum.

Cross-checks To demonstrate the understanding of a proper background subtraction, it is valuable to compare IBD-like distributions between different periods and locations. Firstly, IBD-like event spectrum from a different reactor-on/reactor-off periods are compared in Figure 6.16. The observed consistency between two periods demonstrates the stability of our antineutrino detector over time after accounting for temporal atmospheric changes during reactor-on and reactor-off.

The reactor thermal power of the reactor is relatively stable during HFIR operation. A demonstration of time stability of the IBD rate is shown in Figure 6.17. The neutrino flux should also exhibits clear $1/r^2$ dependence of the baseline, as shown in Figure 6.18

Due to the compact size of the PROSPECT AD, the IBD interactions happened in the inner and outer part or top and bottom part of the segments should exhibit different level of annihilation γ-ray energy leakage, leading to difference in E_{rec} spectrum. The IBD spectrum comparison between the top and bottom half of the detector active volume is shown in Figure 6.19. The ratio of IBD spectrum shows consistency with the ratio of IBD spectrum from the simulations. The same behaviour is found for the inner and outer spectrum comparisons, as shown in Figure 6.20.

The prompt signal of the IBD interaction in the PROSPECT AD usually spans multiple segments. Another good cross-check of the PROSPECT detector response is the multiplicity and energy distribution of the reconstructed pulses outside the maximum hit segment, as shown in Figure 6.21. The data and simulation exhibits compatible distributions within systematic uncertainties.

To summarize, a set of pulse-based analysis selection cuts were developed to efficiently identify the IBD interactions and at the same time greatly suppress reactor-related and cosmogenic-induced γ-ray and neutron backgrounds. The cut-based

Table 6.2: Statistics of selected IBD candidates and accidental/cosmogenic backgrounds.

Category	**Reactor-On**	**Reactor-Off**
Calendar Days	95.65	73.09
Live Days	82.25	65.16
IBD Candidates	115852	30568
Accidental Backgrounds	28358±18	1309±4
Correlated Candidates	87494 ± 341	29258±175
Rate Per Calendar Day	915± 4	400±2
Cosmogenic Backgrounds	36934±221	N/A
Total IBD Signal	50560±406	N/A
Rate Per Calendar Day	529 ±4	N/A

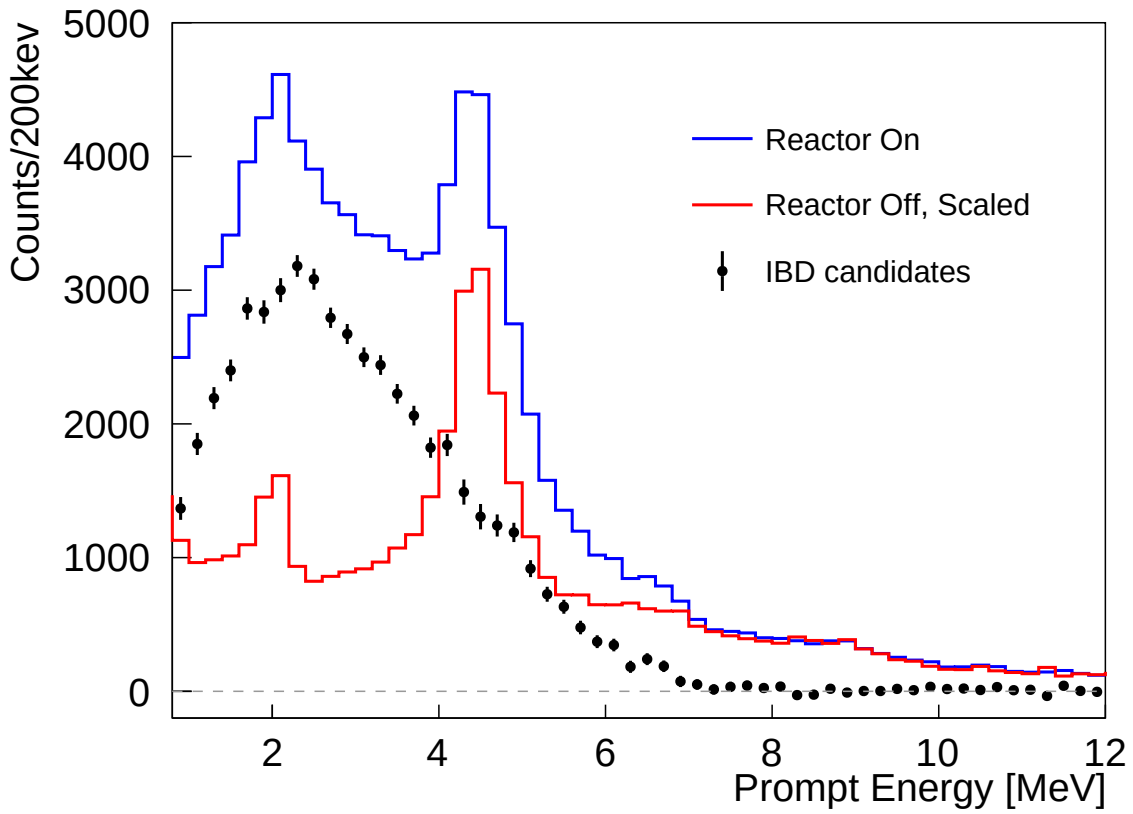


Figure 6.15: The reconstructed visible prompt energy E_{rec} (black marker) spectrum of IBD candidates (statistical error only) in addition to reactor-on(blue solid) and reactor-off (red solid) correlated candidates. The reactor-off spectrum is properly scaled to match reactor-on live time. Atmosphere scaling is also included to scale reactor-off background and all accidental events have been subtracted in the above spectra.

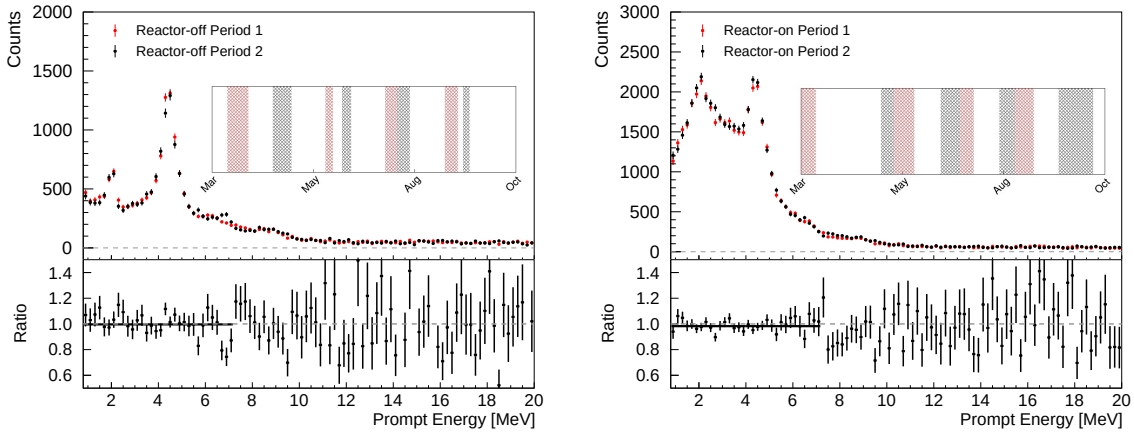


Figure 6.16: The reconstructed visible prompt energy E_{rec} spectral are compared at two periods for reactor-on (right) and reactor-off (left) respectively. Top panel : Reconstructed visible prompt energy from two periods. Bottom panel : The ratio of spectra.

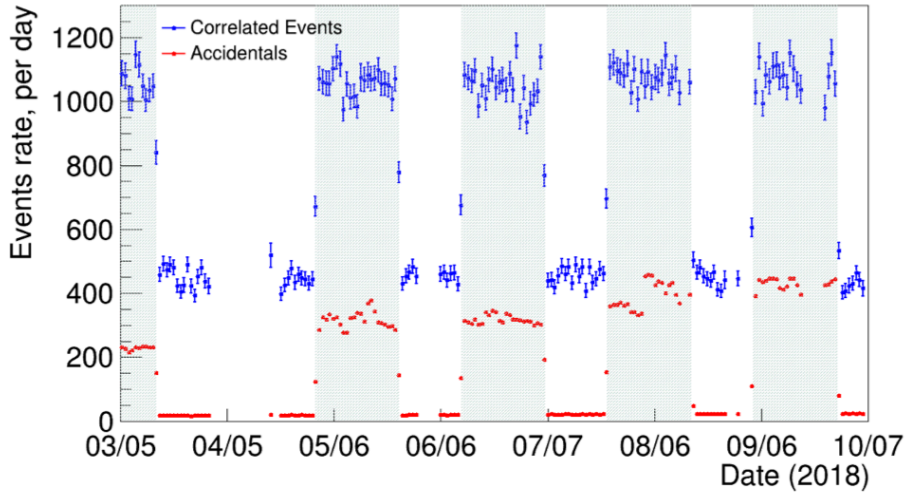


Figure 6.17: Time dependence of correlated IBD candidate rates. The rates are integrated between 0.8 and 7.2 MeV energy range. Source:[92]

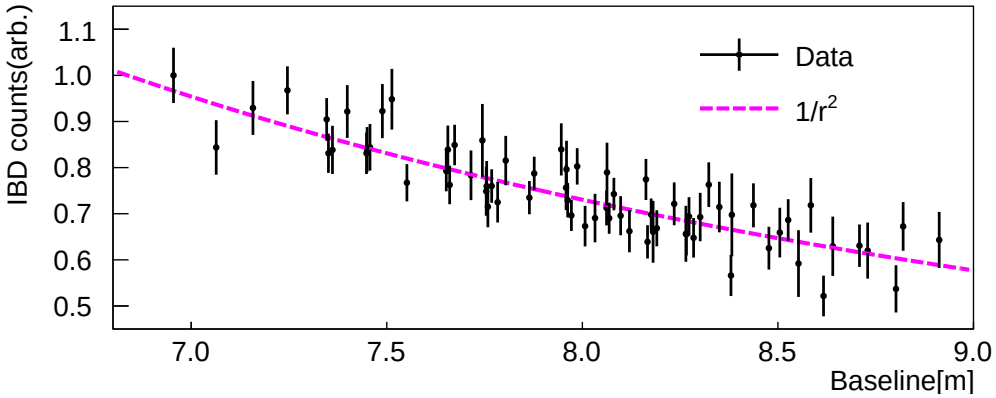


Figure 6.18: Clear baseline-dependence of physics-correlated IBD candidates within [0.8,7.2] MeV is fitted with $1/r^2$ trend. IBD counts are normalized by IBD counts in the shortest baseline bin. Efficiency variations at various baselines are accounted for. χ^2/DOF $\sim$ 72.43/69.

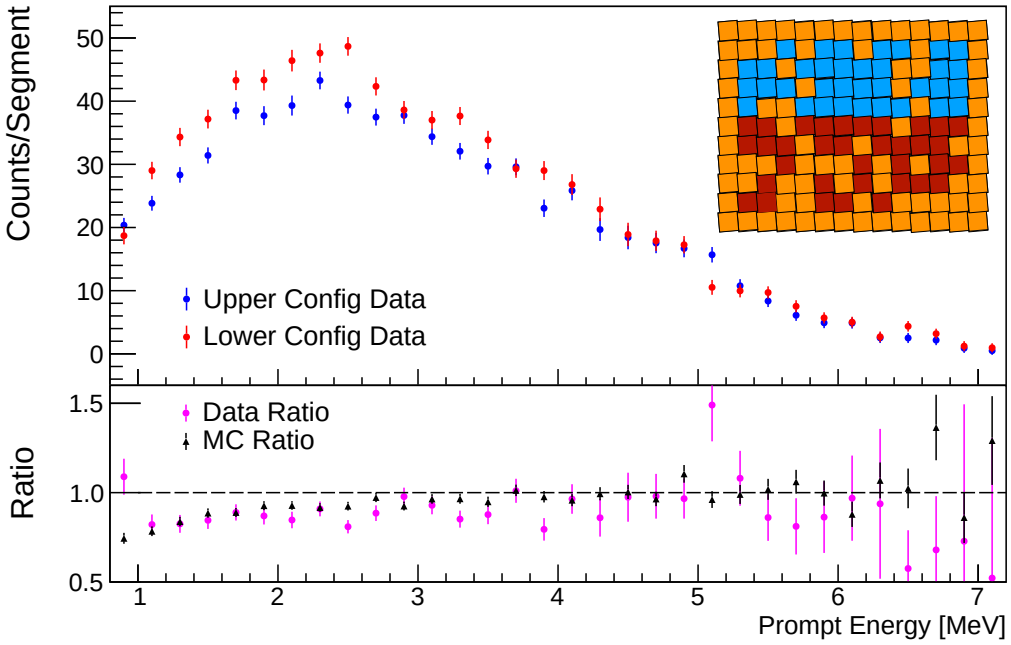


Figure 6.19: Spectra from upper/lower configurations are compared. Counts are normalized to per segment for relative comparison. Top panel : spectra of IBD candidate events (statistical errors only) from upper/lower region. Bottom panel : Ratio of two spectra bin-by-bin from Data/MC.

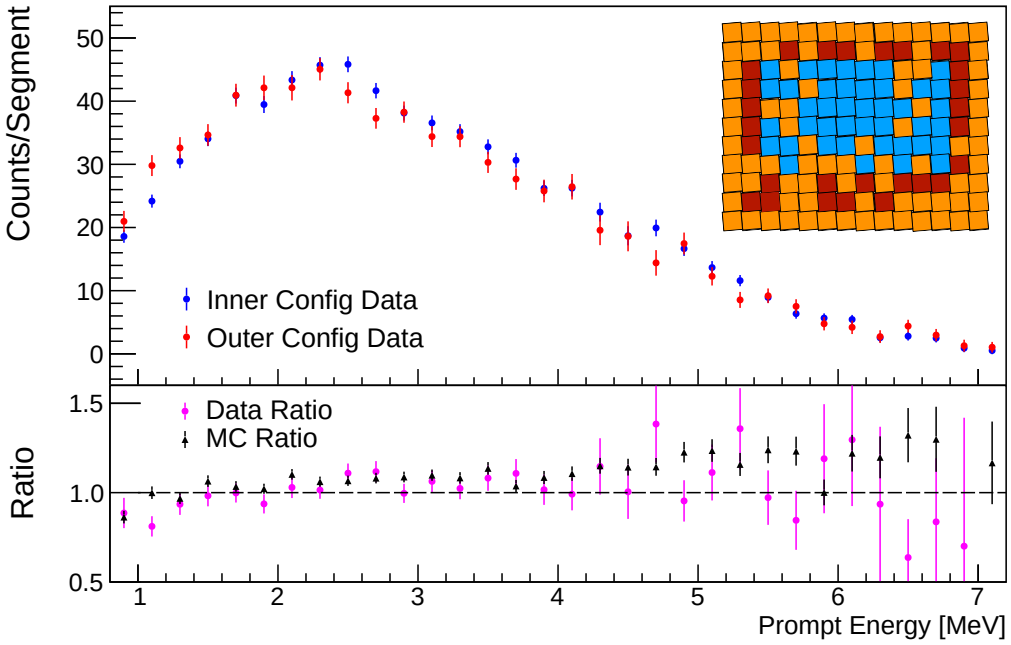


Figure 6.20: Spectra from inner/outer configurations are compared. Counts are normalized to per segment for relative comparison. Top panel : spectra of IBD candidate events (statistical errors only) from inner/outer region. Bottom panel : Ratio of two spectra bin-by-bin from Data/MC.

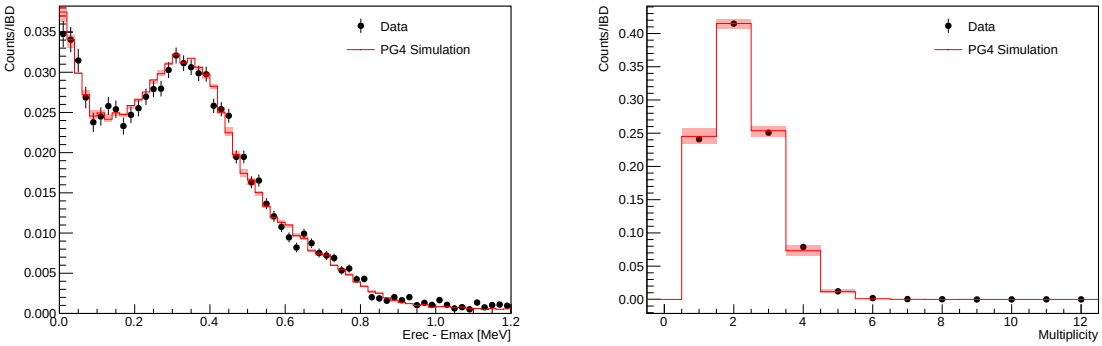


Figure 6.21: Left: Energy deposition distribution outside the main segment where inverse beta decay happens. This mainly comes from annihilation gammas. Right: Pulse multiplicity of prompt cluster. Multiplicity includes the center segment where IBD happens and thus starts with 1 and above.

parameters were optimized to maximize the effective count metric that represents the statistical power of a background-free IBD measurement. The optimization was based on a blinded subset of full PROSPECT dataset to avoid potential bias. The PROSPECT dataset was unblinded once the selection cuts were frozen, yielding a neutrino energy spectrum consisting of more than 50,000 IBD interactions in 96 calendar days of data-taking at an average baseline distance of 7.9 m from the reactor core. A number of cross-checks were performed to validate the time stability of the selection cuts and PROSPECT detector response.

6.4 Results from PROSPECT-I and ongoing analysis

So far, the physics analysis of eV-sterile neutrino searches and the spectral deviation were not discussed yet. Here we describe how these physics analyses were performed from the obtained IBD neutrino energy spectrum, and also briefly describe various ongoing spectral, flux, and oscillation analysis.

6.4.1 Modeling HFIR neutrino spectrum

Both the oscillation and spectral analysis depend on proper modeling of the HFIR neutrino spectrum, in which more than 99% of the neutrinos were produced in ^{235}U fissions. Small fluxes of non-^{235}U neutrinos were produced from ^{28}Al from the fuel cladding, ^{6}He generated in the beryllium neutron reflector [104], and non-equilibrium isotopes due to short reactor cycles of HFIR schedule. The contribution of each source is less than 1% of the total neutrino flux and limited to the low-energy regions of the spectrum, as shown in Figure 6.22.

The leading prediction model of the ^{235}U neutrinos is the Huber beta conversion method discussed in Section 3.1. The predicted neutrino spectrum is passed through the PROSPECT AD response model (illustrated in Figure 5.16) to produce a

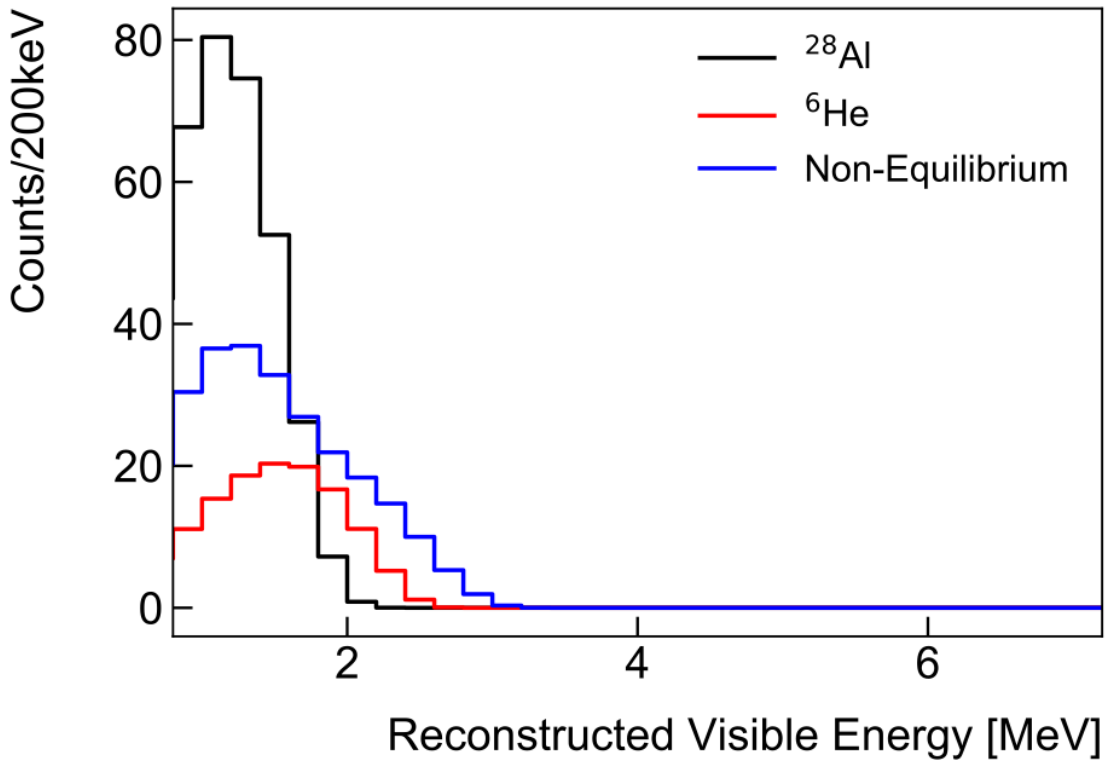


Figure 6.22: Non-fuel contributions to the ^{235}U neutrino spectrum. These neutrino sources contribute less than 1% of the total neutrino flux and limited to the low energy regions. Source:[92]

predicted reconstructed energy spectrum that can be used to compare to the measured spectrum.

6.4.2 Spectrum analysis

A χ^2 metric is used to determined the compatibility of the measured and predicted energy spectrum,

$$\chi^2_{min} = \Delta^T V^{-1} \Delta, \tag{6.5}$$

$$\Delta_i \equiv N_i^{obs} - N_i^{pred} \times (1+\eta), \tag{6.6}$$

where Δ_i is the difference between the measured and predicted energy spectrum for energy bin i up to a normalization fitting parameter η, and V stands for the total uncertainty covariance matrix, including contributions from signal and background statistics, detector systematics, background, reactor-related systematics, neutrino prediction model. More details about the various systematics, refer to reference [92]. In order to better quantify the local deviations of the measured spectrum to the predicted, a local sliding window analysis of 200 keV and 1 MeV width is introduced. A local χ^2 contribution profile is generated for each sliding window width in terms of local p-value format, as shown in Figure 6.23.

In order to investigate the isotopic origin of the spectral bump observed in LEU reactor neutrino experiments, an *ad hoc* Gaussian bump is added to the predicted neutrino spectrum before passing through the detector response. The mean and width of the Gaussian bump was matched to the size of the bump fitted in θ_{13} experiments, with mean 5.678 MeV and sigma 0.562 MeV. The amplitude of the Gaussian bump A is a fitting floating parameter, in units of Daya Bay bump size (A=1), that indicates how much spectral distortion comes from ^{235}U isotope. A best-fit value of $A = 0.84 \pm 0.39$ is obtained, shown in Figure 6.24, indicating the PROSPECT spectrum disfavors no-bump hypothesis (A=0) at 2.17σ, and hypothesis that ^{235}U spectral

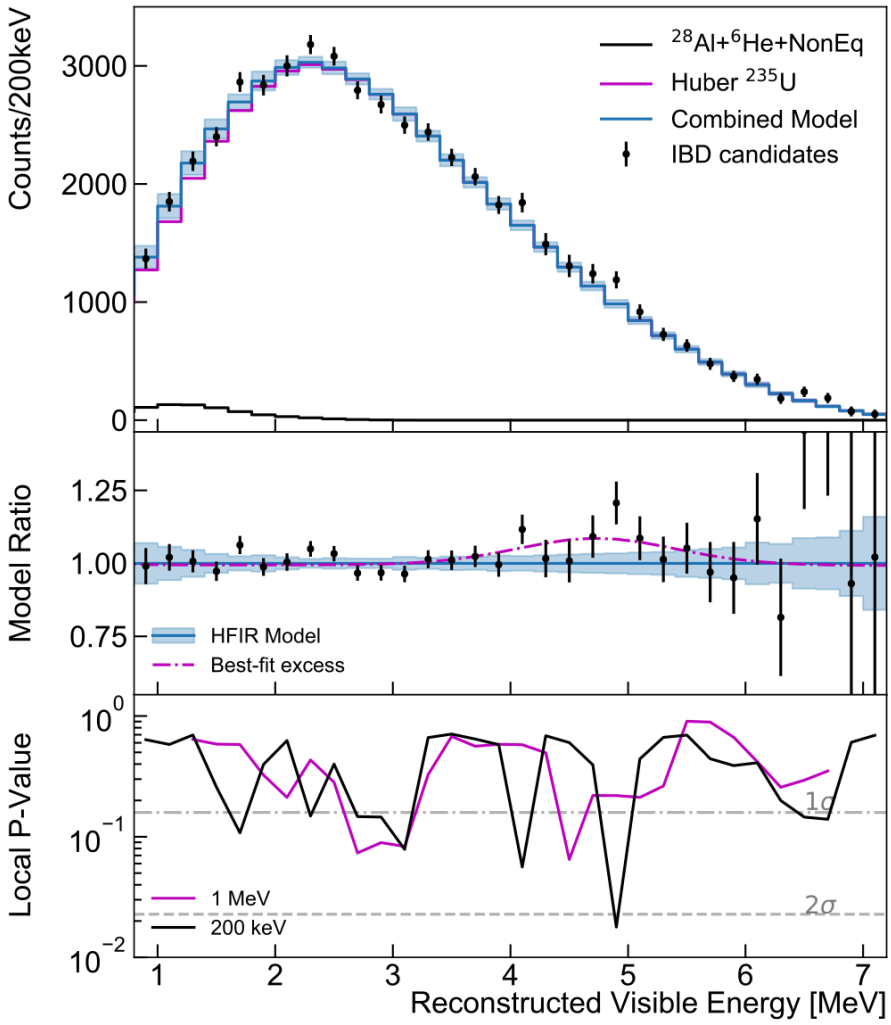


Figure 6.23: Comparison of the ^{235}U predicted spectrum to the measured PROSPECT data. Middle panel shows the ratio of the measured spectrum to the predicted; Bottom panel shows local deviations of the measured spectrum from the predicted in terms of p-value for two types of sliding window analysis with 200 keV and 1 MeV width. Source:[92]

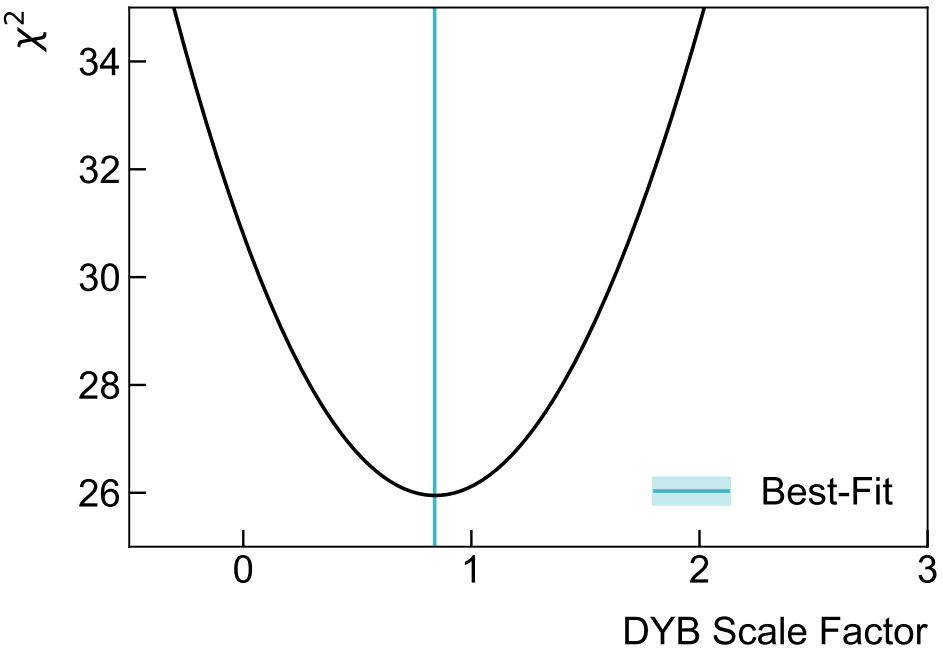


Figure 6.24: χ^2 profile of Gaussian bump amplitude fitting, whose sigma and mean are fixed by the unfolded Daya Bay spectrum, added to the HFIR model prediction. A best-fit value of 0.84±0.39 is found with a $\Delta\chi^2$ of 4.84 with respect to A=0. Source:[92]

distortion is the sole source of the bump in θ_{13} measurements (A=1.78), which is equal to 1 (full Daya Bay bump size) if multiplied with the ^{235}U fission fraction 56% in LEU reactors.

6.4.3 Oscillation analysis

The sterile neutrino search in PROSPECT experiment is performed via a reactor-model independent method by comparing neutrino spectrum at different baselines, as illustrated in Figure 6.25.

Comparisons of the relative spectra at different baselines are performed similarly to Equation 6.5 via the covariance matrix method with a slightly modified $\Delta_{l,e}$,

$$\Delta_{l,e} = M_{l,e} - \frac{M_e}{P_e} P_{l,e} \tag{6.7}$$

where $\Delta_{l,e}$ is 160-element vector with 10 l baseline bins and 16 e energy bins, and M_e, P_e are defined below:

$$M_e = \sum_{l=1}^{10} M_{l,e} \text{ and } P_e = \sum_{l=1}^{10} P_{l,e}. \tag{6.8}$$

The spectrum from 10 baselines are shown in Figure 6.26.

The χ^2 value of Equation 6.5 can be calculated for each point in the sterile neutrino parameter space ($\sin^2 2\theta_{14}$,Δm^2_{41}). The minimum value (χ^2_{min}/DOF) of 119.3/142 was identified at the grid point ($\sin^2 2\theta_{14}$,Δm^2_{41}) = (0.11,1.78 eV^2). A $\Delta\chi^2$ with respect to the best-fit point in phase space, shown in Figure 6.27, can be used to generate allowed and excluded regions in parameter space by two distinct statistical approach, Gaussian CL$_s$ method [105] and Feldman-Cousins frequentist approach [106]. The Gaussian CL$_s$ method provides a conservative excluded region that allows for easy combinations with other experimental results, while Feldman-Cousins frequentist approach addresses overstatement of levels of statistical disagreement between

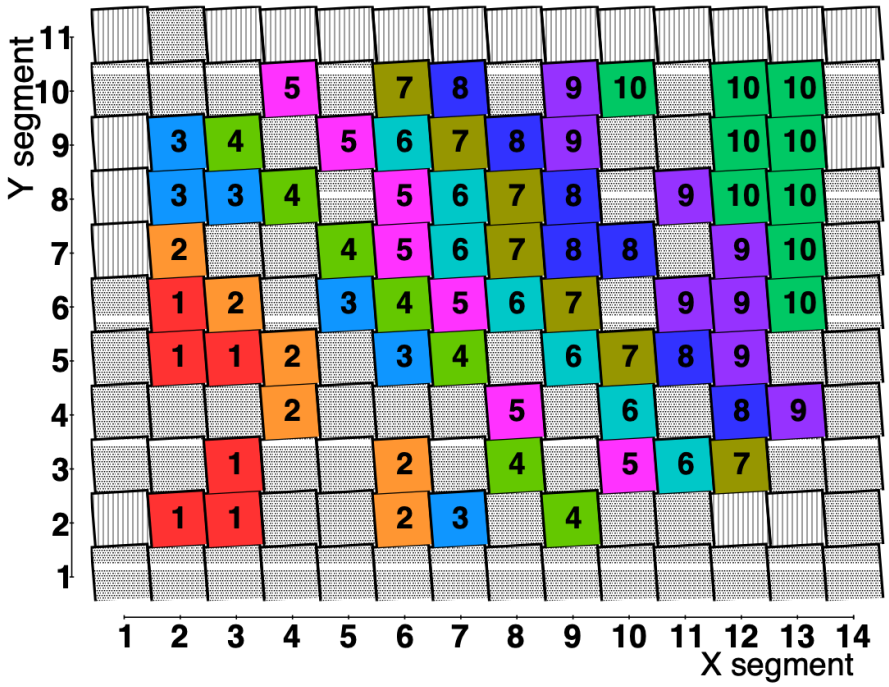


Figure 6.25: Active segments in the active fiducial volume are grouped into baseline bins, indicated by different colors and numbers. Source:[92]

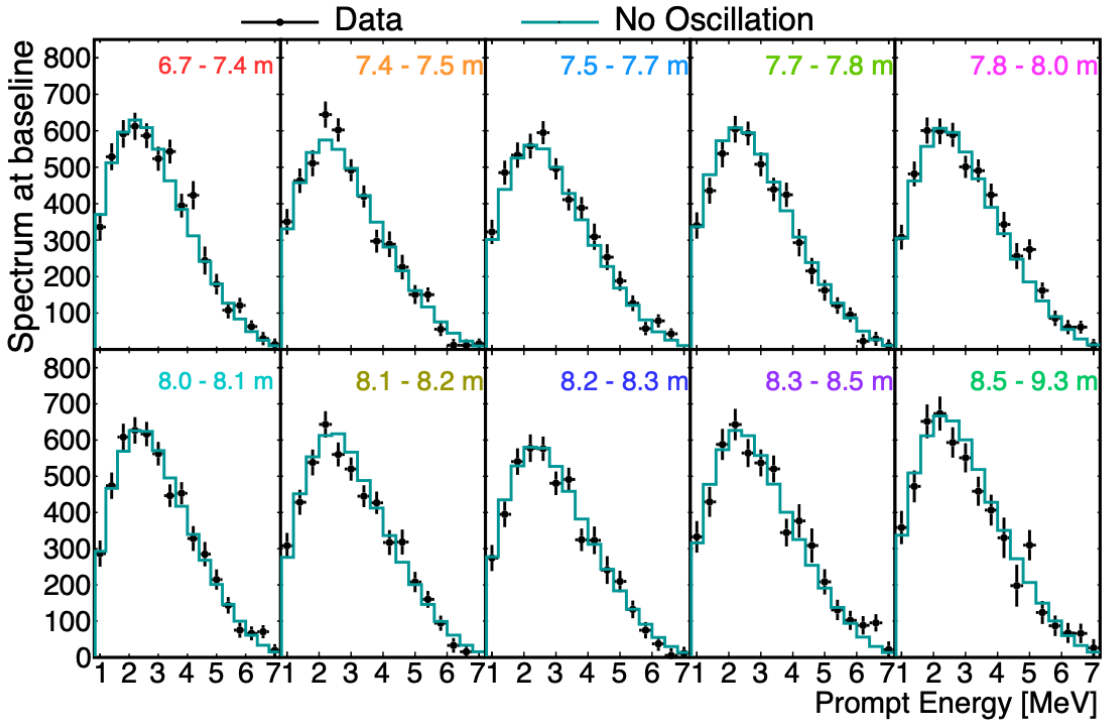


Figure 6.26: IBD spectral at different baselines. No oscillation predictions are in solid line. The predicted spectra are normalized to match the baseline-summed IBD signal. Source:[92]

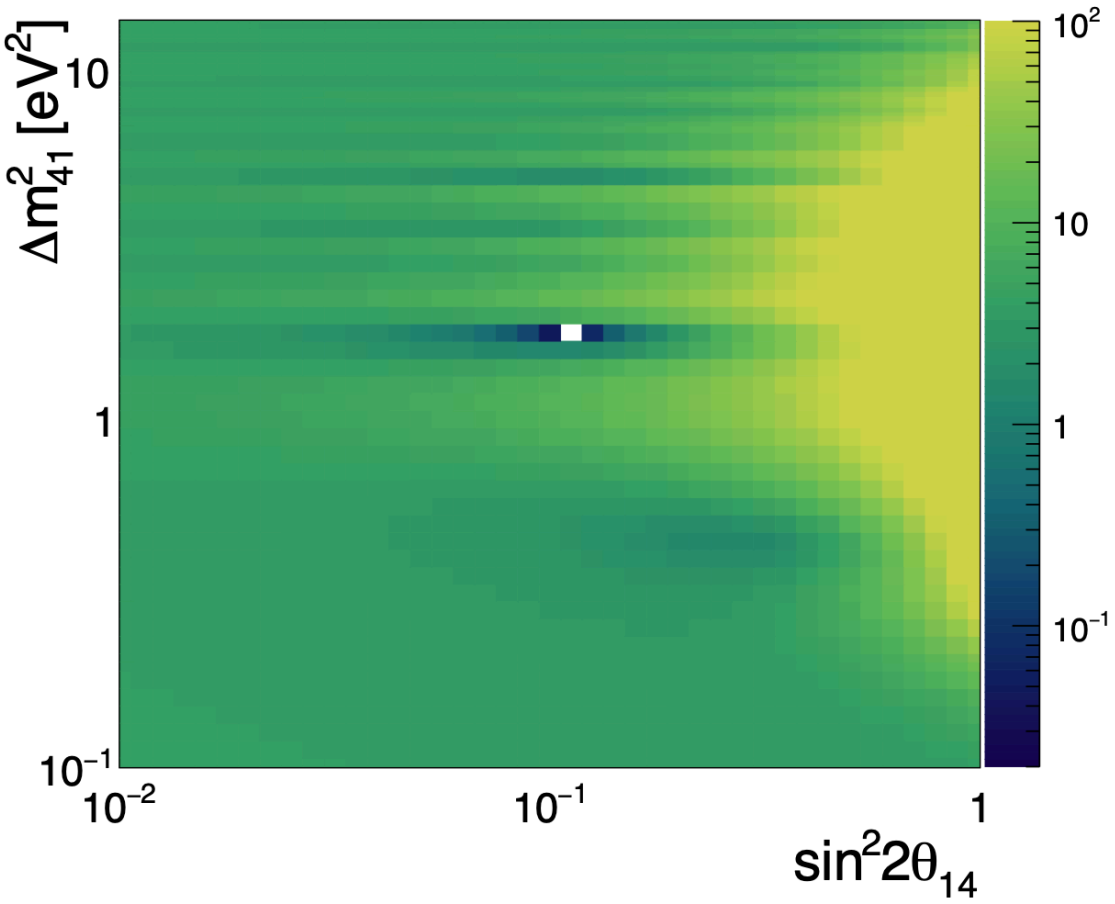


Figure 6.27: The distribution of $\Delta\chi^2$ in phase space ($\sin^2 2\theta_{14}$,Δm^2_{41}) with respect to the best fit point (white square) (0.11,1.78 eV^2) . Source:[92]

data and the no-oscillation hypothesis, as well as understatement of the level of compatibility between the data and some regions of non-zero oscillation parameter space. The exclusion curves generated via Gaussian CL_s and Feldman-Cousins approach are shown in good compatibility in Figure 6.28.

6.4.4 Reactor neutrino anomaly discussion

The existence of the bump cannot be explained by neutrino oscillations or sterile neutrinos. The cause of the bump could be rooted in the inaccurate measurement from the nuclear database and missing forbidden beta decay transitions. For example, the forbidden beta decays dominate the bump region and could be inaccurately incorporated in the conversion method [25]. New corrections to β feeding to higher states in daughter isotopes from Modular Total Absorption Spectrometer (MTAS) measurements could impact the bump size in high energy regions [107]. An improved conversion calculation (HKSS model) of reactor antineutrino fluxes in 2019 using forbidden transitions yielded a partial resolution of the 5 MeV bump but with larger antineutrino flux [108]. To date, the shape anomaly is still not fully understood, and requires global efforts from both the theoretical and experimental sides.

With the recent results of eV^2 scale sterile neutrino from PROSPECT [92] and STEREO [109], the best-fit point of the reactor antineutrino anomaly is rejected with high statistical significance. Estienne and Fallot *et al.* (EF model) reported a reduced ^{235}U antineutrino flux from the summation method using updated nuclear database, and was roughly in agreement with the experimental measurements [110]. More recently, Kopeikin *et al.* [111] in the Kurchatov Institute (KI model) reported an updated β spectrum ratio measurement between ^{235}U and ^{239}Pu, resulting in a smaller flux in the converted ^{235}U antineutrino compared to the Huber-Mueller model [112]. *

*However, the Neutrino-4 experiment [113] reported observation of sterile neutrino oscillations with $\Delta m^2_{41} = (7.3 \pm 1.137)\text{eV}^2$ and $\sin^2 2\theta_{14} = 0.36 \pm 0.12(\text{stats})$. The Neutrino-4 claim was in strong tension with the KATRIN, PROSPECT, STEREO experiments and was criticized by Giunti *et al.* [114].

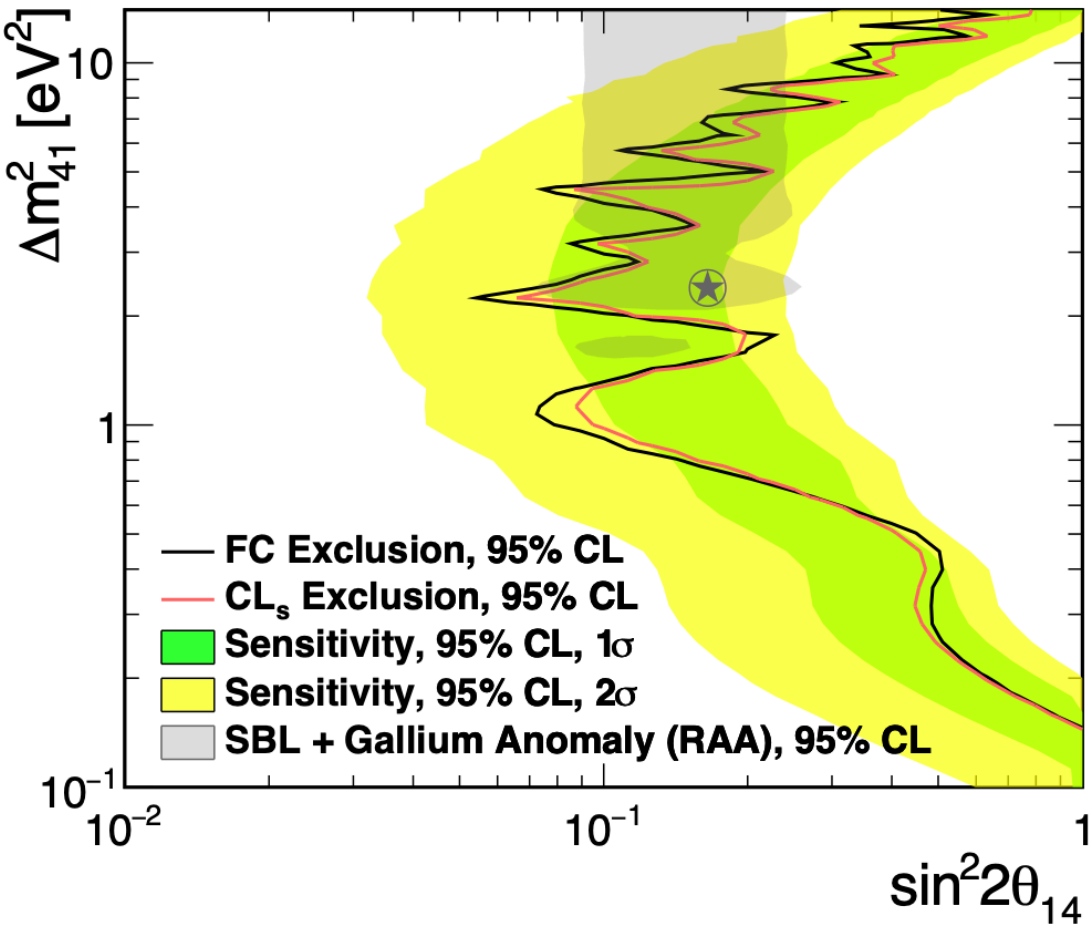


Figure 6.28: Exclusion curves generated via both Gaussian CL_s and Feldman-Cousins frequentist, as well as the best-fit RAA. The 1σ and 2σ (green and yellow) exclusion ranges are generated by PROSPECT toy simulations. Source:[92]

To summarize, the antineutrino flux deficit was partially resolved with EF summation model and KI conversion model with the deviation from the data about 1σ. The spectral anomaly is yet to be fully understood, and could be deeply rooted in the reactor nuclear physics.

6.4.5 Ongoing and future analysis

In addition to the published results on the spectrum shape and sterile neutrino oscillation analysis, there are still several ongoing analyses.

The PROSPECT is current planning an absolute neutrino flux analysis based on the original PROSPECT data. The measured IBD cross section per fission can be expressed as,

$$\sigma_f^{\text{obs}} = \frac{N^{\text{obs}}}{\frac{P_{\text{th}}}{<E_f>}\frac{N_p}{4\pi L^2}\epsilon_{\text{det}}} \tag{6.9}$$

where N^{obs} is the number of detected IBD, P_{th} is the thermal power of the reactor, $< E_f >$ is the average thermal energy released per fission, N_p is the number of target protons, L is the baseline distance, and ϵ_{det} is the IBD detection efficiency. Currently, the collaboration is working on determining the IBD detection efficiency, which is a key parameter for an absolute flux analysis.

As the time of writing, the PROSPECT collaboration has just updated its IBD analysis using multi-period data splitting and additional single-ended segment information [115, 116], effectively doubling the statistics of the previous analysis. The multi-period and single-end segment approach effectively traded increased analysis complexity caused by failing segments for better background rejection capability and more IBD signal statistics. The new analysis technique recovered over 25% of the previously reported number of IBD candidates and made a major improvement to background rejection, resulting in a signal-to-background ratio increase from 1.58 to 4.11. An updated oscillation analysis is in the works using the same improved IBD dataset. The updated spectrum and oscillation analysis also enables a triple joint analysis with STEREO and Daya Bay collaboration.

Chapter 7

PROSPECT-II program

The PROSPECT experiment collected more than 50,000 IBD interactions of $\overline{\nu}_e$ produced in beta decays of ^{235}U fission products in 96 calendar days. Despite the unexpected shutdowns of HFIR reactor and increasing numbers of PMT failures, the PROSPECT experiment reported one of the strongest limits on eV-scale sterile neutrinos and made hypothesis testing on the isotopic origin of the spectral bump observed in LEU and HEU reactor experiments. PROSPECT demonstrated detector techniques for an aboveground observation of antineutrinos with a good energy resolution and well-controlled backgrounds. The PROSPECT collaboration is now preparing for an upgraded detector, PROSPECT-II, to further extend the physics of the program.

This section will discuss major design changes of the upgraded PROSPECT-II detector and the physics goals the collaboration envisions for the program.

7.1 Physics goals of PROSPECT-II

The upgraded PROSPECT-II detector will measure the world-leading ^{235}U electron antineutrino spectrum, provide a total flux analysis of the reactor neutrino, search for sterile neutrino oscillations in larger parameter space, and possible redeployment of the detector to another commercial LEU reactor site to further expand the physics

of the program. The primary goals of PROSPECT-II program are closely related to the new features introduced in the PROSPECT-II detector. The main upgraded designs of the PROSPECT-II detector will be discussed in detail in Section 7.2. We here summarize some of the highlights:

- Separation of PMT modules outside the active LiLS volume ensures the long-term functional stability of the detector.
- Reduction of number of materials in contact with LiLS and *in-situ* LS replacement capability also ensures PROSPECT-II long term operation and possible redeployment to other commercial LEU reactor site.
- Longer data-taking operation time and elongation of active target LiLS volume with 25% longer segment length and 20% increased ^{6}Li-doping fraction by mass will increase the total neutrino statistic expected from PROSPECT-II detector.

Table 7.1 summarizes the main parameters of PROSPECT-I detector and expected PROSPECT-II detector at HFIR and commercial LEU reactor site. The highlighted major upgrades and a multi-year deployment of the upgraded PROSPECT-II detector at HFIR yields a significant increase in the total IBD statistics, which is the principal limits of current PROSPECT's oscillation and spectrum analysis. The IBD statistics shown in Table 7.1 is defined as the reactor-on IBD-like candidates with full background and accidental subtraction:

$$N_{IBD} = N_{\mathrm{On}} - N_{\mathrm{On},a} - R(N_{\mathrm{Off}} - N_{\mathrm{Off},a}), \tag{7.1}$$

where N_{On} and $N_{\mathrm{On,a}}$ are the prompt IBD-like candidates and accidental backgrounds during reactor-on periods, N_{Off} and $N_{\mathrm{Off},a}$ are the same but for reactor-off periods, and R is the relative reactor on-to-off live-time ratio to account for the time variance between reactor on and off. More relevantly, the effective IBD statistic are calculated using a effectively background free IBD measurement and better represents the

Table 7.1: Major experiment parameters for the PROSPECT-I detector ('P1') and nominal parameters for PROSPECT-II ('P2') deployments at HFIR and at a commercial LEU reactor.

Parameter		**P1**	**P2 at HFIR**	**P2 at LEU**
Reactor	Power (MW_{th})	85		3000
	Cylinder Size (d×h, m^2)	0.4×0.5		3×3
	Fuel	HEU		LEU
	Cycle Length	24 d		1.5 y
Detector	Segmentation	11×14	11×14	
	Segment Area (cm^2)	14.5×14.5	14.5×14.5	
	Segment Length (m)	1.17	1.45	
	Target Mass (ton)	∼4.0	4.8	
	Light collection (PE/MeV)	∼380	500	
	Detection Efficiency	∼40%	40%	
Exposure	Average Baseline (m)	7.9	7.9	25
	Reactor-On Days (d)	105	336	548
	Reactor-Off Days (d)	78	360	61
	Signal:Background	1.4	4.3	19.3
	IBD Statistics (N_{IBD})	50560	3.74×10^5	2.72×10^6
	Effective Statistics (N_{eff})	15195	2.08×10^5	1.79×10^6

statistical capabilities of the dataset in terms of the primary oscillation, spectrum measurement, and total flux analysis. The definition of the effective IBD statistic is defined using the same parameters in Equation 7.1:

$$N_{\mathit{eff}} = \frac{((N_{\mathrm{On}} - N_{\mathrm{On},a}) - R(N_{\mathrm{Off}} - N_{\mathrm{Off},a}))^2}{(N_{\mathrm{On}} + N_{\mathrm{On},a}) + R^2(N_{\mathrm{Off}} + N_{\mathrm{Off},a})} \tag{7.2}$$

Using the expected signal-to-background ratio of 4.3 for the PROSPECT-II detector, a two-year deployment of the PROSPECT-II detector at HFIR will detector over 200,000 effective IBD statistics, which is over 10 times larger than the roughly 15,000 effective IBDs reported in PROSPECT recent results [92]. The significant boost in IBD statistics will increase the sensitivity of the sterile neutrino oscillation analysis, reduce ^{235}U neutrino spectrum statistical uncertainties, and a modern ^{235}U neutrino flux measurement.

One of the main physics goals of PROSPECT experiment was to test for the signatures of sterile neutrino oscillations. The model-independent searches for sterile neutrino oscillation channels perform relative comparisons of measured IBD prompt energy spectra between different baselines in the detector, as illustrated in Figure 6.25. Prompt spectrum of IBD interactions reconstructed within groups of detector segments are compared to the predicted energy spectrum, oscillated or un-oscillated, in the same group of detector segments. The model prediction spectrum dictated by the parameters (Δm^2_{41}, $\sin^2 2\theta_{14}$) and the measured spectrum undergoes a χ^2 test. Both correlated and uncorrelated systematic and statistical uncertainties are included in the χ^2 test statistic using a covariance matrix approach. Using the same PROSPECT systematic uncertainties such as energy scale, baseline, relative efficiency variations, and re-simulated detector responses of the PROSPECT-II detector, projected sterile neutrino sensitivities for PROSPECT-II using the nominal detector parameters from Table 7.1 are shown in Figure 7.1. Current PROSPECT sensitivity is mostly limited by statistics, also shown in Figure 7.1. Even with one year's data-taking at HFIR, the sensitivity of PROSPECT-II improves by a factor

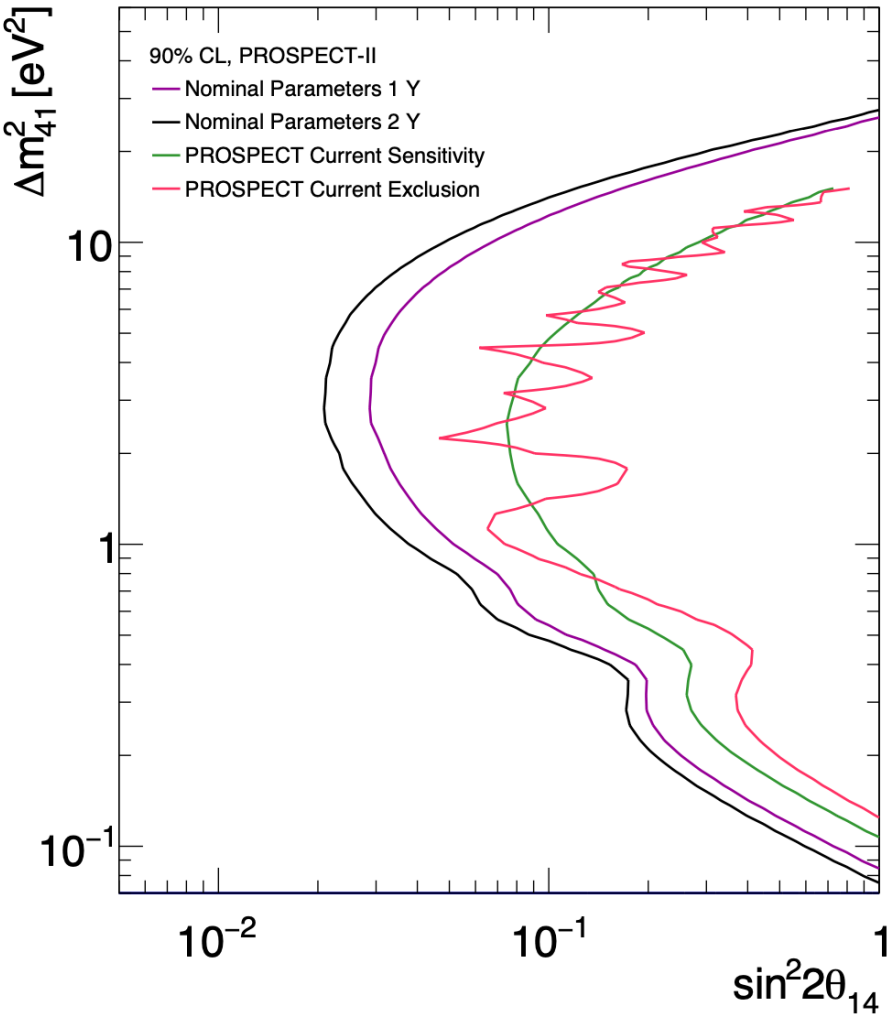


Figure 7.1: Projected sensitivities for PROSPECT-II with nominal detector parameters with one year and two years' detector data-taking time. Current PROSPECT sensitivity is also shown for comparison. Source:[117]

of up to three, depending on the mass splitting value. In the global context of the current and future sensitivities from other short-baseline neutrino experiments are shown in Figure 7.2. With two years' operation time at HFIR, PROSPECT-II will offer the best coverage in the sterile neutrino parameter space in high mass splitting values among all short-baseline reactor experiments. With one year's data-taking, PROSPECT-II will conclusively address the Neutrino-4's claim of an observation of sterile neutrino oscillations near 7 eV^2 [118] in spite of controversial analysis and statistical issues that had been raised by the community [119, 114]. In Figure 7.3, PROSPECT-II sensitivities are compared in the context of other relevant neutrino experiments. With two years' of data-taking at HFIR, PROSPECT-II will conclusively address the remaining parameter space of the best-fit oscillation explanation for the Reactor Antineutrino Anomaly. The sensitivities of PROSPECT-II will also cover an important gap in sensitivity space between Daya Bay disappearance results at low Δm^2 ($<$0.2 eV^2) [120] and KATRIN beta-endpoint measurement results at high Δm^2 ($>$10 eV^2) [121]. PROSPECT-II will also achieve the $\sin^2 2\theta_{14} = 0.03$ guideline with 95% confidence level, which is the CPV ambiguity limit advised for clarifying long-baseline interpretations [122] up to the parameter space around 10 eV^2.

The PROSPECT-II detector will also significantly improve the precision of PROSPECT's world-leading measurement of the ^{235}U neutrino energy spectrum, bringing spectrum uncertainties below 5%. The PROSPECT-II spectrum with higher statistics will also contribute to understandings of the spectral disagreement in 4-6 MeV reconstructed energy range. Figure 7.4 illustrates the improvement to PROSPECT-II ^{235}U spectrum measurement uncertainties after two years' of data-taking and PROSPECT-II hypotheses testing for bump-like feature in the 4-6 MeV prompt energy region observed by Daya Bay at high confidence level. PROSPECT-II's detector systematic uncertainties will be greatly reduced and the effective neutrino energy resolution will also improve through the elimination of lost IBD positron energy in non-functioning detector segments. In Figure 7.5, the simulated detector response to a mono-energetic source of 4 MeV $\overline{\nu}_e$ is displayed for both the current

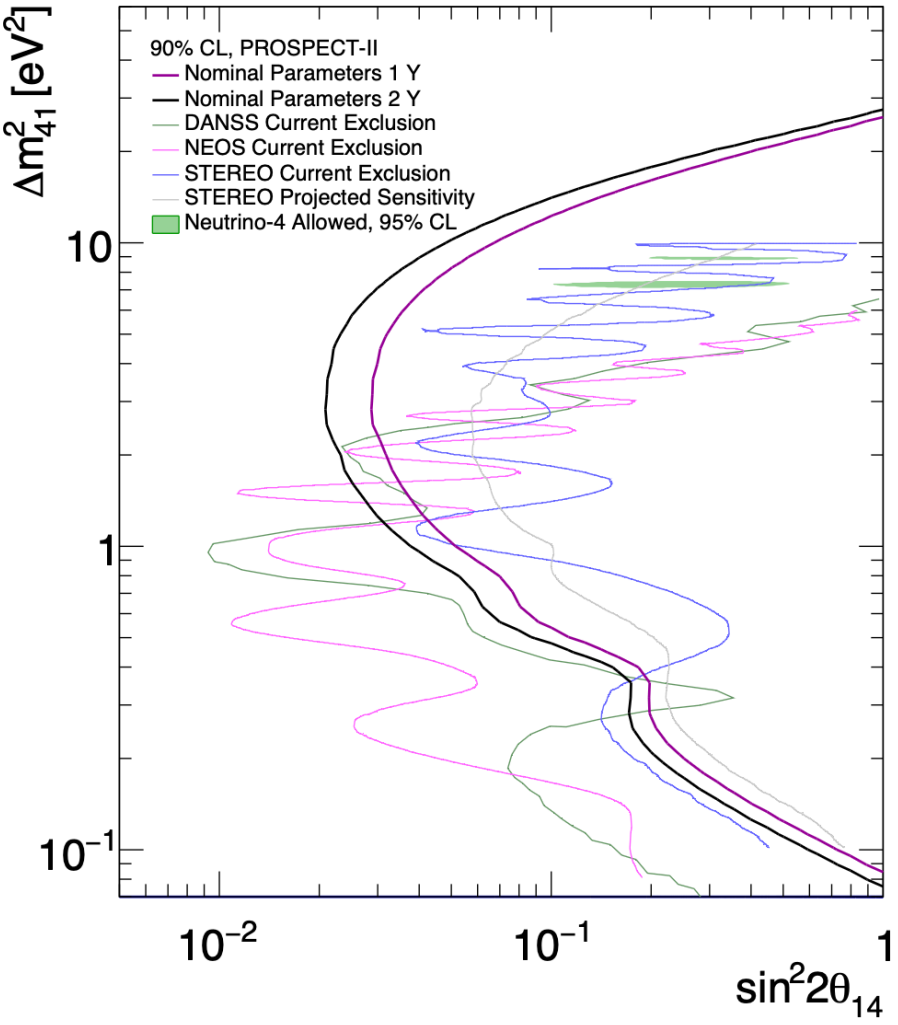


Figure 7.2: Projected sensitivities for PROSPECT-II with nominal detector parameters with one year and two years' detector data-taking time. Other short-baseline neutrino experiment contours are overlapped in comparison [70, 68, 118, 109]. Source:[117]

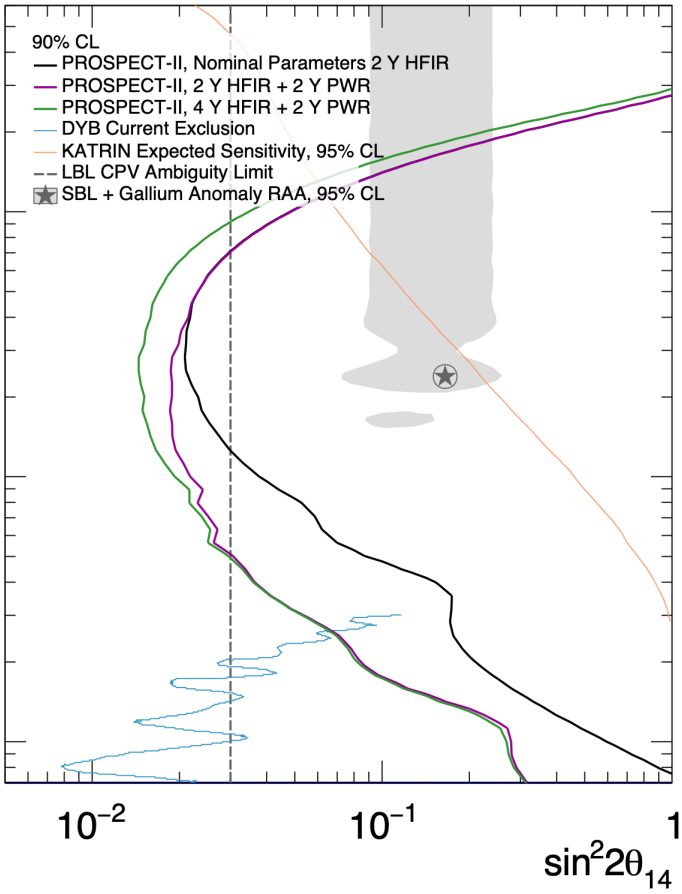


Figure 7.3: Project PROSPECT-II sensitivities with/without longer operation time and commercial LEU reactor redeployment. Daya Bay [120] and KATRIN [121] experiment sensitivities are also overlapped. The long-baseline CP-violation limit of couplings between sterile and active neutrino sectors is indicated by the dashed line [122]. Source:[117]

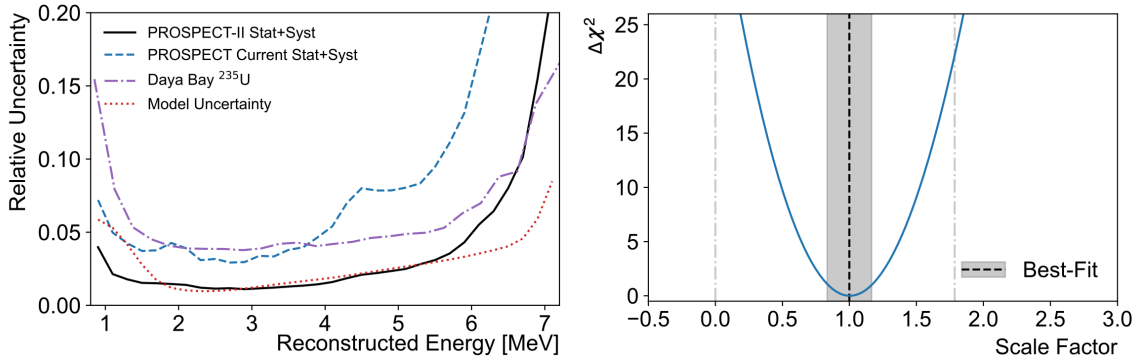


Figure 7.4: Left: Improvement to PROSPECT-II ^{235}U spectrum measurement uncertainties after two years of data-taking. Right: PROSPECT-II hypotheses testing for bump-like feature in the 4-6 MeV prompt energy region observed by Daya Bay at high confidence level. n=0 represents no contribution from ^{235}U and n=1.78 represents entire contribution from ^{235}U. Source:[117]

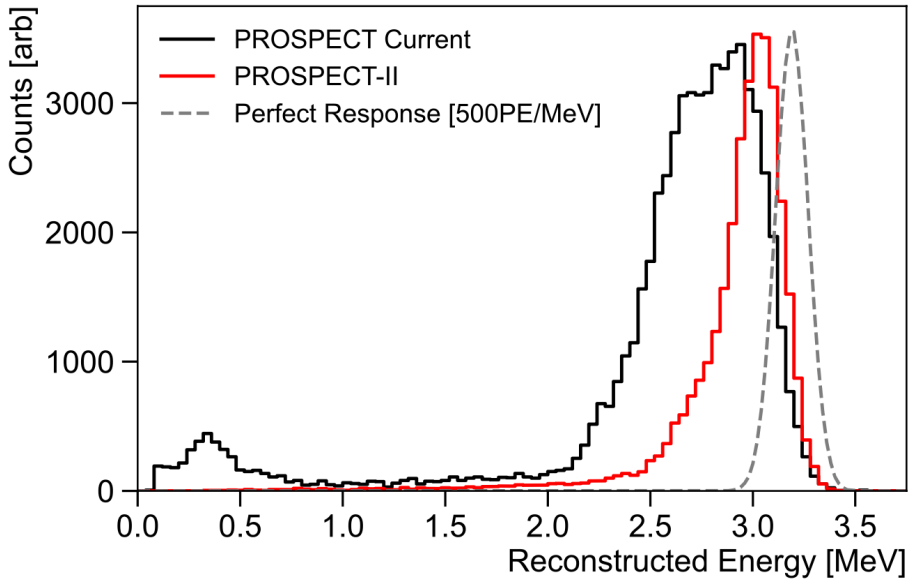


Figure 7.5: Comparison of simulated detector response to monoenergetic 4 MeV $\overline{\nu}_e$ for the PROSPECT-II detector (red) and the current PROSPECT detector (black). Source:[117]

PROSPECT detector and projected PROSPECT-II. The reconstructed energy peak in PROSPECT-II exhibits an improvement to the full width at half maximum and the energy bias with respect to the perfect full-energy peak by a factor of two in comparison to current PROSPECT detector response.

In addition to the spectrum measurement at HFIR, the PROSPECT-II detector will also make a precise measurement of the $\overline{\nu}_e$ flux produced in ^{235}U fission. PROSPECT-II HEU flux measurement will improve the understanding of the global-fit flux deficit that was strongly influenced by 30 year old HEU flux measurements and also provide an independent check of the HEU deficit recently observed at $\sim$10 m by STEREO [123]. As of this writing, the PROSPECT collaboration is preparing for a flux analysis based on original PROSPECT dataset, but encountered large uncertainties in IBD detection efficiency due to the positron energy loss and neutron migration effects in dead segments. The PROSPECT-II detector with zero non-functional segment and external γ-ray and neutron calibration will be able to achieve IBD detection efficiency determination below percent-level precision. With the 2%-level knowledge of HFIR's average thermal power, the PROSPECT-II neutrino flux measurement can achieve $\sim$ 2.5% accuracy.

7.2 PROSPECT-II detector

The precision goals of the PROSPECT detector was unprecedented for a segmented detector operating on-surface with minimal overburden. In order to achieve such precision, the PROSPECT detector had PMT housing in the optical grid to eliminate cross-talk and a calibration system for the full liquid scintillator volume, necessitating incorporation of PMT housings within the LiLS volume. However, PMTs started to fail gradually during the operation of the detector data-taking as a result of the LiLS leakage into the PMT housings, leading to the loss of segments in the active target volume. Additionally, large numbers of required penetrations of the inner acrylic tank combined with the diversity of materials in contact with the LiLS from

the calibration system likely led to the gradual degradation of the scintillator light yield. The PROSPECT-II detector had several design changes to improve the long-term stability of the upgraded detector, only requiring modification to the inner detector design and leaving the exterior outer aluminum containment vessel, shielding packages, and DAQ system mostly unchanged. These upgrade choices also keeps PROSPECT-II detector within the established size and weight footprint for operation at HFIR. The main upgrade to the inner detector is moving the PMTs outside the LiLS volume to reduce to the possibilities of LiLS leakage into the PMT housings and also reduces the number of materials in contact with LiLS, providing a more robust inner system without loss of detector performance degradation for long term operation.

The inner containment vessel is redesigned as a result of the PMT and LiLS separation shown in Figure 7.6. The target LiLS and optical reflector panels are contained in the PTFE-lined aluminum inner containment vessel (ICV). On each side of the ICV, thin UVT acrylic windows divides the LiLS target from the PMTs, sealed by double O-rings. PMT arrays are mounted on the PMT support frame. The space between the inner detector and the outer containment vessel is filled with mineral oil. The inner containment vessel structure is also redesigned and reinforced to allow for transportation by commercial air-ride trailer and redeployment at a different reactor site to expand the physics of the PROSPECT-II program. The reflectors will mostly use the same combination of materials of laminated FEP film, DF2000MA reflector, and carbon fiber. The reflecting panels are held in place by corner rods. The outermost reflector panels are separated from the inner containment wall by acrylic spacers, providing spaces for PTFE calibration source tubes, as shown in Figure 7.7. The acrylic window between the LiLS target and the PMTs provides a single piece of optical interface, thus introduces a small amount of optical cross-talk between segments of the detector. Details of the impact of this cross-talk effect are discussed in Section 8.3. A quick evaluation of the impact of the cross-talk on the event reconstruction is shown in Figure 7.8 using data from the first month of the

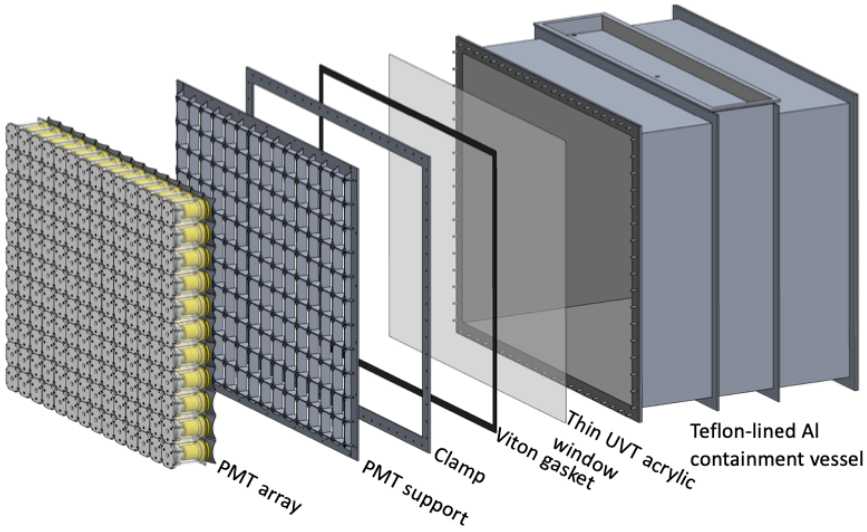


Figure 7.6: Exploded-view of the redesigned inner detector. The PMTs arrays and LiLS volume is separated by the thin acrylic window. The whole inner detector will be submerged in mineral oils filled within the outer containment vessel. Source:[117]

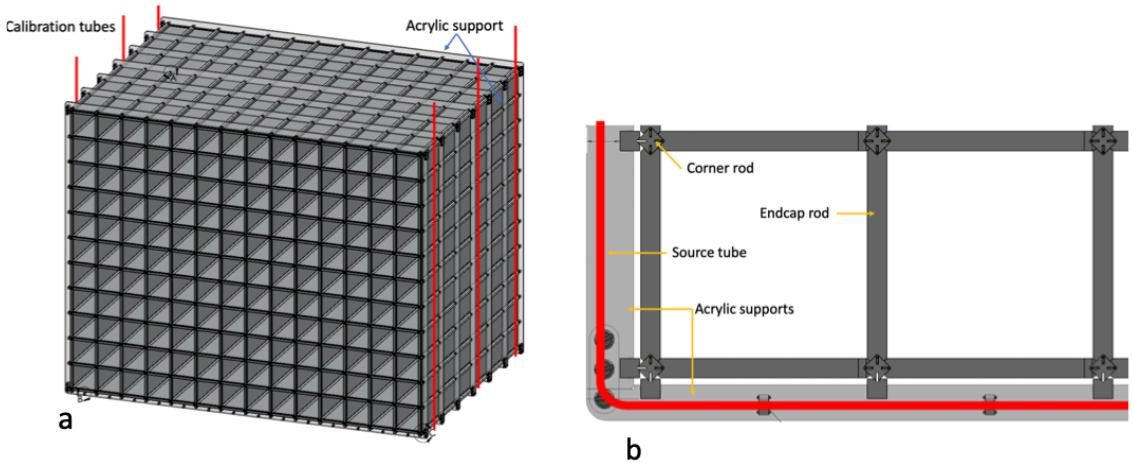


Figure 7.7: Left: Illustration of the external calibration source tubes along the perimeter of the segment array. Right: Side view of the reflector panels supported by corner rods and endcap rods. The outermost reflector are spaced by acrylic spacers from the inner containment wall, allowing for calibration source tubes. Source:[117]

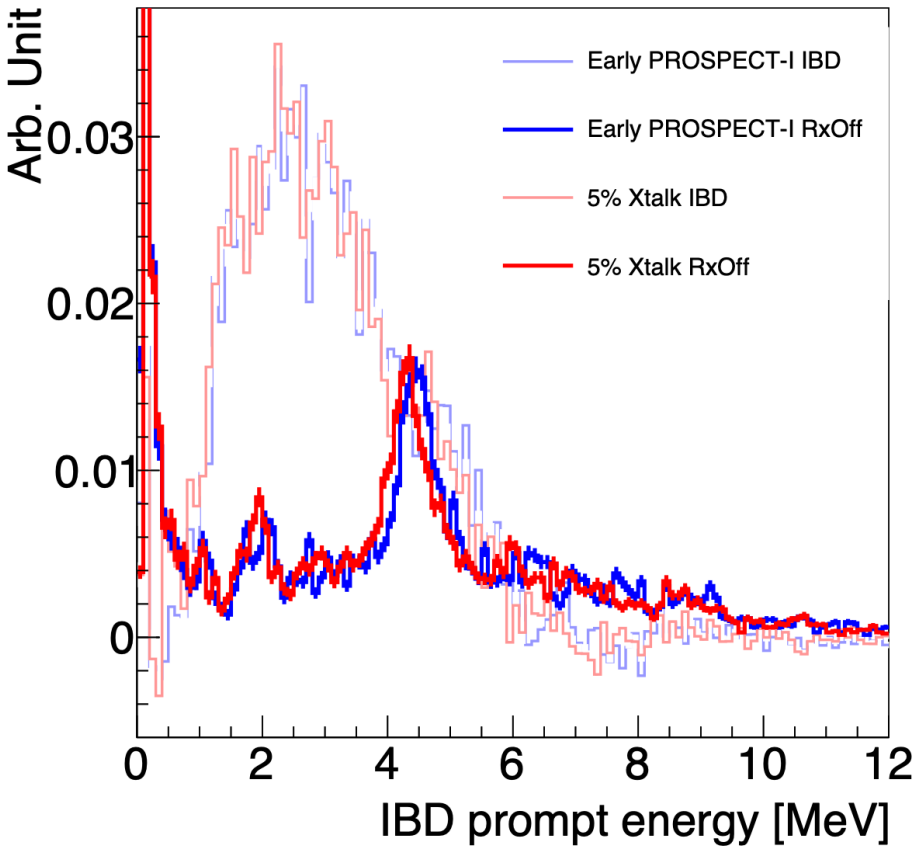


Figure 7.8: Using PROSPECT-I early dataset, the IBD-like prompt spectra are shown for reactor-off periods and reactor-on periods with full background subtraction. The blue is the original dataset without cross-talk and the red is applied with artificial cross-talk. Source:[117]

PROSPECT detector operation. A 5% cross-talk level is found to decrease the signal-to-background ratio for this early PROSPECT-I dataset from 2.9:1 to 2.8:1. This also demonstrated that the cross-talk expected in the PROSPECT-II detector will not substantially decrease event selection capabilities in the data analysis. The separation of the PMTs and LiLS volume effectively increases the active target volume of the detector by $\sim$20%, corresponding to a 30% increase in fiducial volume. Estimated using the default PROSPECT-I segment length of 118 cm, the expected IBD event rate is roughly 900/day with a signal-to-background ratio of 3.8.

The longer segment length of 145 cm in the PROSPECT-II increases the expected IBD rates to about 1150/day with a much improved signal-to-background ratio of 4.3. The liquid scintillator will be based on the same formulation given the great light yield output and excellent PSD capabilities observed in PROSPECT. The ^{6}Li-doping by mass will be slightly increased to 0.1% from the original 0.08%.

Chapter 8

Alternative energy scale calibration strategy for PROSPECT-II

The PROSPECT experiment was very successful despite early termination of operation due to a combination of PMT divider failure and unexpected HFIR downtime. We detailed a series of upgrades and additional physics capability for PROSPECT-II experiment in Chapter 7. The upgrades mainly focused on the long-term stability and structural robustness of the detector and possible relocation to a low-enriched-uranium (LEU) reactor after an initial deployment at HFIR.

One of the main upgrades in the PROSPECT-II detector is the separation of PMTs from the liquid scintillator volume to eliminate the possibility of liquid scintillator leakage into the PMT housings. This change allows for a simpler, fully-sealed liquid scintillator tank structure with minimal penetrations. Calibration access to the interior of the optical lattice would increase the complexity and risks associated with the tank design. Therefore we explore a calibration scheme that uses deployable sources located outside the optical lattice but inside the tank.

Given the precision goals of PROSPECT-II, it is essential to confirm that energy scale systematic uncertainties can be sufficiently constrained using an external calibration scheme. The ability to understand the response of highly segmented

detectors, like PROSPECT-I and PROSPECT-II, requires detailed Monte Carlo (MC) simulation models and data from a range of calibration inputs across the entire relevant energy range. When PROSPECT-I was designed, we chose to deploy internal calibration sources as a conservative approach to ensure a precise energy scale. Calibration analyses for PROSPECT-I demonstrated that excellent agreement between data and MC could be achieved, and that a uniform energy-scale response could be established across the entire detector. This outcome enables us to explore the feasibility of a data-driven external calibration scheme for the PROSPECT-II detector and its possible applications to other similar segmented detectors.

The study presented in this thesis aims to demonstrate the feasibility of an energy calibration scheme for a multi-segmented array such as P-II, eliminating the need to deploy internal radioactive sources. The goal of the energy calibration is a relative systematic uncertainty less than or comparable to the expected P-II statistical uncertainty. With recent interests in multi-segmented detectors on the scale of PROSPECT for neutrino physics or nuclear non-proliferation monitoring purposes [124], external source deployment provides a less intrusive yet versatile way to calibrate liquid or solid detectors. Improved and simplified calibration techniques for multi-detector arrays is a goal shared with other fields of subatomic physics such as intermediate-energy nuclear reaction studies that utilize large 4π multi-detector arrays. Detailed investigation of the interaction of various species with the detection medium as a function of E, Z and even A [125] has resulted in the characterization of the light output for a variety of nuclear species with a single quenching constant considerably simplifying the calibration process. It is worth noting that in the case of PROSPECT the detection medium is common to all segments; the segments, by construction, have very similar optical properties; and the range of energies of interest is modest (100 keV to 10 MeV) and adequately covered with conventional sources. The challenge however is the use of only external low energy sources, the low-Z detection medium, and additional passive shielding, resulting in reduction on the photopeak yields and decreased event multiplicities.

8.1 Setup for external energy calibration

This section details the procedure of external calibration scheme using the PROSPECT-I dataset and simulation package. This data-driven approach of approximating PROSPECT-II external calibration performance using existing PROSPECT-I calibration data and simulation is enabled by the high segmentation nature of the detector, which consists of 154 optically-isolated segments in 14×11 grid. Figure 8.1 shows a cross-sectional view of the detector segments and illustrates two calibration schemes: a PROSPECT-I internal calibration and a representation of the external calibration.

The approximation of a PROSPECT-II external calibration can be achieved by selecting data from an inner segment potion of the detector and excluding data from the outer segments, without any changes in the signal triggering and data acquisition. With these segment configuration capability, we can effectively perform external calibration analysis using existing PROSPECT-I calibration data and simulations. This study will evaluate the performance of the calibration using externally deployed calibration source and intrinsic cosmogenic induced ^{12}B decay events in PROSPECT-II . The actual segment and calibration source layout are shown in Figure 8.2, due to the fact that an increasing number of PMT failures caused PMT voltage divider instabilities. The white segments on the left of Figure 8.2 represents the non-functional PMTs, and represents functional segments but were excluded from the calibration analysis on the right of Figure 8.2 to mimic the PROSPECT-II external calibration. Note all particle interactions in the non-functional and excluded segments are tracked in the simulation.

The PROSPECT-I calibration dataset came from the calibration campaign, which consisted of individual deployment of a set of γ-ray and neutron sources at the indicated locations inside the detector. The simulation packages were built in GEANT4 [126] to generate a detailed detector model based on the measured detector geometry and materials with tunable energy scale model parameters. The best-fit

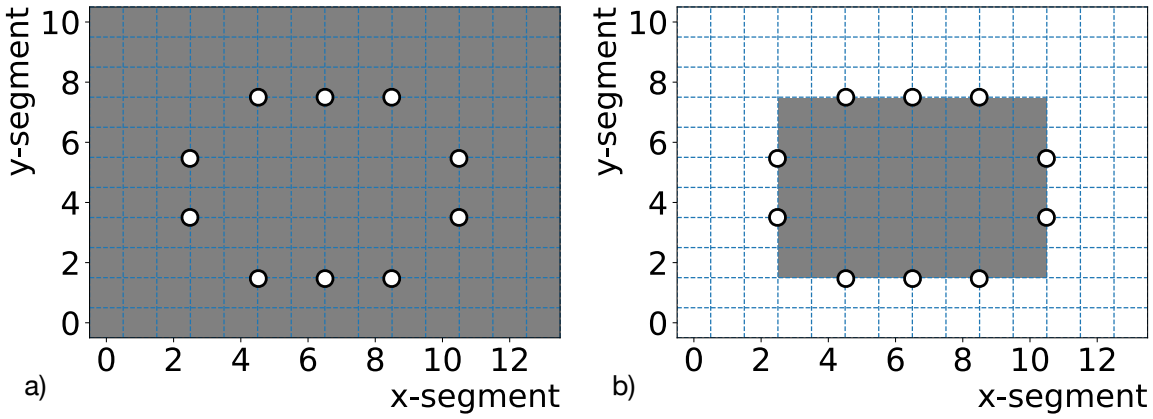


Figure 8.1: Illustration of the PROSPECT-II external calibration performance evaluation using PROSPECT-I data and simulation in an ideal case where all detector segments were functional. a) PROSPECT-I internal source configuration. Active segments are represented in gray. b) PROSPECT-II "external source" configuration. White segments are excluded from the calibration analysis. Source location indicated by white circles are for illustration purposes. Only one source is deployed at a time.

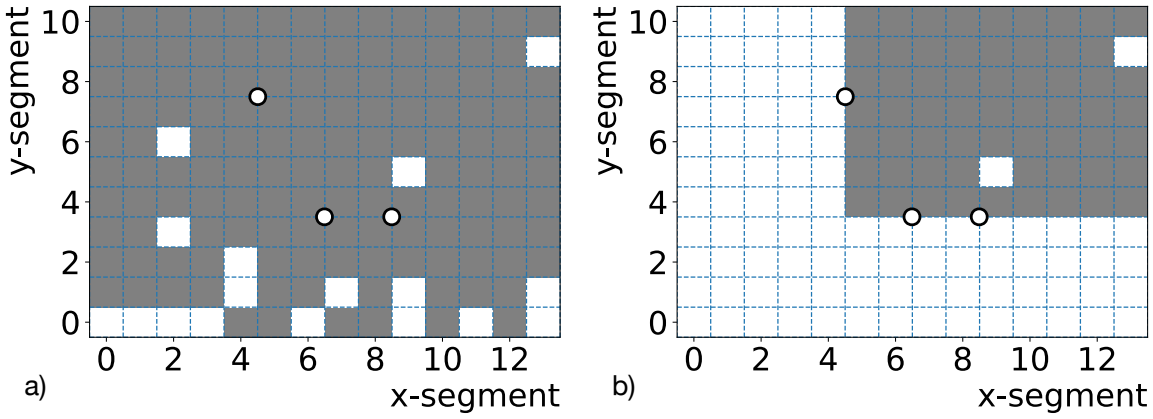


Figure 8.2: Illustration of the actual PROSPECT-II external calibration performance evaluation using PROSPECT-I data and simulation. This differs from the idealized case of Figure 8.1 due to a number of PMT failures at the time of calibration campaign. The white circles indicate available source locations and only one source was deployed at a time. a) Actual PROSPECT-I radioactive source and segment layout. b) Configuration used in this work to mimic external calibration.

energy scale model is determined by minimizing the data-simulation χ^2 comparisons, the details of which were covered in Chapter 5 and later in the section.

A quick sanity check of this approximation method was done by setting up the segment layout illustrated in Figure 8.3 and compare the ^{60}Co calibration spectrum between data and simulation. The gamma peaks of the ^{60}Co were more likely to be single captures than the double captures, easily explained by the fact that the ^{60}Co source were location outside the smaller active target volume and only covers half of the solid angles compared to the case where the source is fully surrounded by the liquid scintillator. Notably, the energy of the feature gamma peaks matches really well with the simulations, reconfirming the approach we used for this study.

8.1.1 Calibration data

We confirmed the approach to use PROSPECT-I data and simulation to evaluate the performance of the external calibration by analyzing the response of a subset of the segments of the detector in Figure 8.3. Here we go over additional details about the calibration campaigns that were not present the discussion in Section 4.2.4. There are in total four calibration campaigns (April 2018, August 2018, December 2018, and February 2019) during the operation of the PROSPECT experiment, and later calibration campaign has more non-functional segments due to PMT failures. The best segment configuration would be the early stage of the detector, as shown in Figure 8.2. During each calibration campaign, various γ-ray and neutron sources were deployed in the available 35 calibration source tube locations, the known energy and activity of which were summarized in Table 8.1.

Additionally, the ^{22}Na source provides the positron annihilation for the study of annihilation γ-rays transport. The neutrons produced from the spontaneous fission of ^{252}Cf source can be used for a source of tagged and internally produced 2.22 MeV γ-rays from the p(n,γ)d reaction. The AmBe source was acquired by the PROSPECT collaboration near the end of data-taking and only used for data-simulation energy

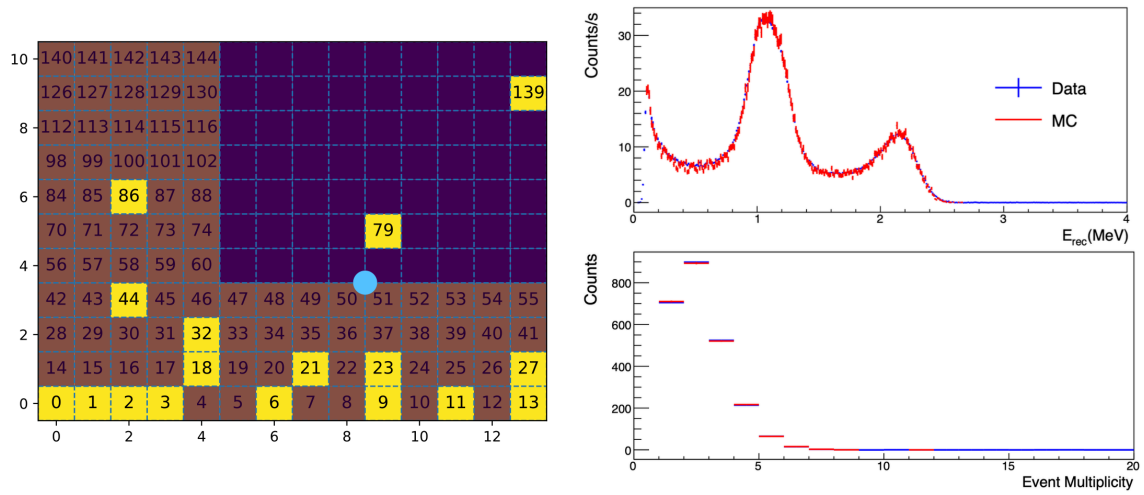


Figure 8.3: Sanity validation of the external energy scale using deployed ^{60}Co source in the indicated source location. The spectra comparison between the data and simulation is shown on the left.

Table 8.1: Calibration sources and their γ-ray energy. The AmBe source was added for the external calibration analysis.

Source	**Type**	**γ-ray Energy (MeV)**	**Activity**
^{137}Cs	γ-ray	0.662	0.1 μCi
^{22}Na	γ-ray	2x 0.511, 1.275	0.1 μCi
^{60}Co	γ-ray	1.173, 1.332	0.1 μCi
^{252}Cf	neutron	2.223 (n-H capture)	866 n/s
AmBe	neutron	4.4	70 n/s

scale validation purpose in the PROSPECT analysis. The intrinsic cosmogenically produced ^{12}B (predominantly β-decays with an energy up to 13.4 MeV) helps establish detector response in the higher energy region and will remain the same for both calibration schemes.

During calibration campaigns, the sources were deployed at 35 source tube locations and each has seven positions with 20 cm apart along the length of the segments. Typically, the center source deployment for energy scale ran for 10 minutes, while other off-center deployments usually ran for a short 5 minutes for edge effect studies. The AmBe source was deployed more than 10 hours overnight to accumulate sufficient statistics due to low activity. In the calibration analysis, calibration events were identified by selection criteria mostly based on PSD particle identification, the event multiplicity which is the number segments lit up with energy depositions above a 90 keV energy threshold, and additional spatial and temporal correlation. For electron-like events from the γ-ray sources, they were identified via the PSD values if it was within the within 3σ of the mean electron-like PSD band as a function of energy. The integral γ-ray rate of $\mathcal{O}(1000)$ counts per second for the entire energy range is observed with all selection cuts applied. ^{252}Cf events were selected by identifying a correlated pair of a prompt γ-ray from ^{252}Cf fission followed by a 2.22 MeV γ-ray from the p(n,γ)d thermal neutron capture interaction. The n-H capture γ-ray has to be within 200 μs of the prompt γ-ray as the requirement of the time coincidence cut. ^{12}B event identification, generated via the ^{12}C(n,p)^{12}B interaction, requires a correlated prompt single-hit proton-like recoil event with energy of from 0.7 MeV$_{ee}$ to 10 MeV$_{ee}$, followed by a delayed signal that has electron-like PSD with energy less than 15 MeV and multiplicity ≤ 3. The time coincidence between the prompt and the delayed signals is between 3 and 30 ms, and the distance separation is set to be less than 12 cm. More details can be found in the thesis [102].

8.1.2 Parameterization of the energy scale model

The physics of liquid scintillator and detector energy scale parameterization was discussed in great detail in Chapter 5. Birks' law [93] offered an empirical description of the light yield as a function of the energy loss and path length for a particle traversing a scintillator detector. A second order Birks' model was employed in PROSPECT analyses, however, it was found that current calibration data are also well produced by a first order approximation. As a result, the external calibration analysis is performed with a first order Birks' model.

The GEANT4-based Monte Carlo simulation package developed for the PROSPECT detector was extensively benchmarked and reproduces detector response well [92]. As discussed in Chapter 5, the Monte-Carlo simulation with tunable energy scale model parameters simulates particles traversing the liquid scintillator and converts the deposited energy to scintillation light via a nonlinear relation. The energy scale model parameters were fitted by comparisons of simulations and comprehensive calibration data collected with a set of neutron and γ-ray radioactive sources and intrinsic ^{12}B across the entire PROSPECT energy scale to precisely reproduce PROSPECT detector energy response nonlinearities.

In GEANT4, the energy deposition is accumulated with each simulation step is now simplified using the same fractional conversion rate of true deposited energy in the scintillator to scintillation light,

$$E_{MC} = A \sum_i (E_{scint,i}(k_B) + E_{c,i}(k_C)), \tag{8.1}$$

where $E_{scint,i}(k_B)$ contains only first order Birks' approximation as follows:

$$\frac{dE_{scint}}{dx} = \frac{\frac{dE}{dx}}{1 + k_B \frac{dE}{dx}}, \tag{8.2}$$

and $E_{c,i}(k_C)$ was discussed in Section 5.2 and Equation 5.8.

The simulations contain 1×10^6 and 4×10^5 events for the γ-ray sources (^{60}Co, ^{137}Cs, ^{22}Na) and ^{252}Cf neutron source, respectively, and 1×10^6 events for cosmogenic ^{12}B, for each set of nonlinearity parameters. This choice of the size of the simulation provides ample statistics (over four times larger than the event statistics of the calibration data) for energy scale model optimization while keeping computation time moderate. The selection rules we discussed in the previous section will be applied to both the calibration data and simulations. The simulation spectra using nonlinear energy model parameter k_B and k_C from Equation 8.1 will be subsequently rescaled by the overall scaling factor A, which allows the parameter A to be varied without re-running the simulation.

8.1.3 χ^2-based energy scale model determination

The energy scale model of the detector is fit to the set of calibration data by minimizing the χ^2 function described in Equation 8.3, which was previous described in Chapters 5. However we still show it again to improve the readability of the following section.

$$\chi^2_{\text{data-MC}} = \sum_{\gamma} \chi^2_{\gamma} + \sum_{\text{multi}} \chi^2_{\text{multi}} + \chi^2_{^{12}\text{B}}, \tag{8.3}$$

The χ^2 function consists of contributions from both the energy spectra and the event multiplicity distributions from radioactive sources described in section 8.1.1. The χ^2 contribution from the individual γ-ray spectra is denoted as χ^2_{γ}. The event multiplicity distributions for each source are included in χ^2_{multi}. The intrinsic cosmogenic ^{12}B β-spectrum contribution is denoted as $\chi^2_{^{12}\text{B}}$. The γ-ray event multiplicity distribution captures the detector response to low energy deposits and threshold effects, and thus plays an important role in constraining the energy model for highly-segmented inhomogeneous liquid scintillator detectors. The ^{12}B β-dominated spectrum constrains the energy response model in the high energy region up to $\sim$14 MeV.

A point-wise search of minimum $\chi^2_{\text{data}-\text{MC}}$ is performed in the three-dimensional detector response parameter space (A,k_B,k_C) using weighted histogram comparison as follows [127]:

$$\chi^2 = \sum_{i=n_{\min}}^{n_{\max}} \frac{(W_E w_{Si} - W_S w_{Ei})^2}{W_E^2 \sigma_{Si}^2 + W_S^2 \sigma_{Ei}^2}, \tag{8.4}$$

where W_E and W_S are the integrated bin contents from experimental and simulation histograms, respectively, w_i is the individual bin content, σ_i is the individual uncertainty from each bin, $n_{\min}$ and $n_{\max}$ is the lowest and highest energy bin of the range of interest. The χ^2 value is calculated in the energy range covering all peak areas and regions between the peaks, defined as the lower energy edge of the lowest energy peak to the upper edge of the highest energy peak. The peak locations of the data energy spectrum are identified by the ROOT peak-finding algorithm, and the lower and upper edges are located at $\pm 3\times$ energy resolution of 4.5 $\%/\sqrt{E}$ around each peak energy, which is the measured energy resolution from the PROSPECT detector [92]. Figure 8.4 shows simulations generated by the best-fit energy scale model in comparison to the ^{22}Na calibration data. The grey lines in the spectrum plot indicate the energy range for the χ^2 optimization. The bin size of the energy spectrum is 0.01 MeV, and the event multiplicity range for χ^2_{multi} between 1 and 9, since negligible event counts are found. Note the three-dimensional $\chi^2_{\text{data}-\text{MC}}$ map in the model parameter space (A,k_B,k_C) is hard to visualize and can be simplified without change of the fundamentals of the model optimization and will significantly reduces the computation time for a point-wise search in axis-A. The decoupling of axis-A is achieved by the fact that the parameter A is the overall energy scaling factor of the energy spectrum, thus can be optimized once the other two parameters are set. With axis-A decoupled from the three-dimensional response parameter space, a two-dimensional $\chi^2_{\text{data}-\text{MC}}$ map can be easily visualized in the parameter coordinate (k_B,k_C), shown in Figure 8.5. Elliptical contours with a $\Delta\chi^2 = 30$ are plotted centered around the minimum value of the $\chi^2_{\text{data}-\text{MC}}$. The elliptical contours are used to

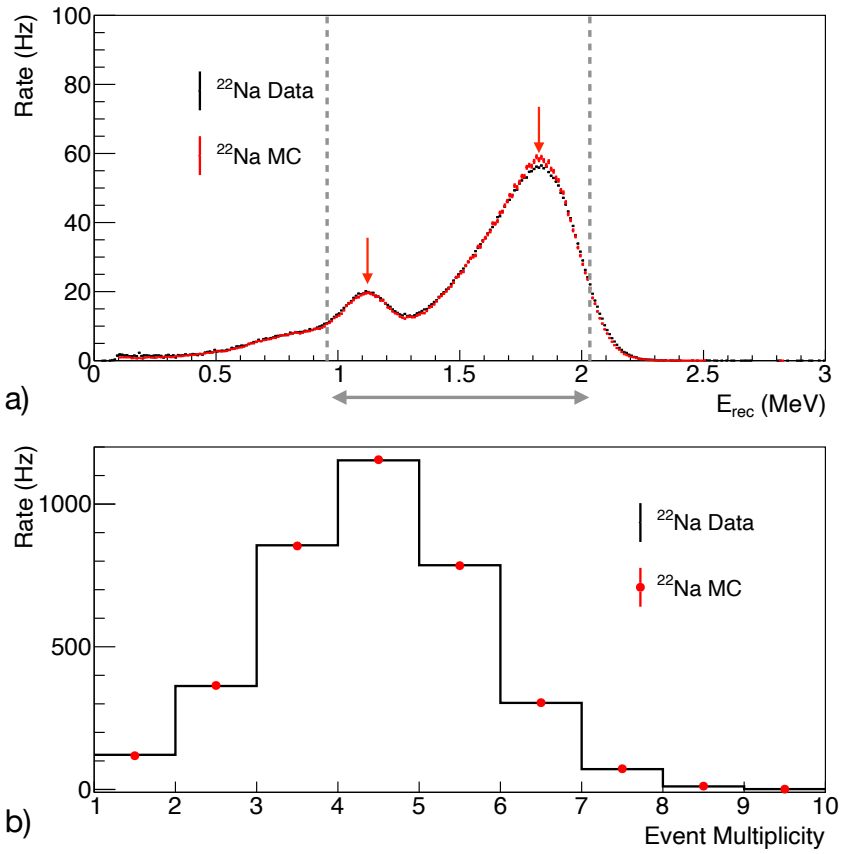


Figure 8.4: Here we show ^{22}Na data and MC comparison for an internal energy scale model, corresponding to the best-fit set of nonlinearity model parameters. The reconstructed energy E_{rec} represents scintillator quenched visible energy, which is typically shifted to lower energy compared to the true gamma energies. The gray lines in a) indicate the energy range for χ^2 calculation. They are determined by the peak location and energy resolution as described above. The range for event multiplicity is between 1 and 9, as shown in b).

determine the each parameter's best fit value and uncertainty. The best-fit values of k_B and k_C parameters are simply the ellipse's center value, and their associated uncertainties half of the projected width in each parameter axis within $\Delta\chi^2 = 30$ boundary. The best fit value of A is the average of all values of A within the $\Delta\chi^2 = 30$ contour, and the uncertainty is half of the A variation. Note the choice of $\Delta\chi^2 = 30$ is chosen very conservatively by intention and larger than the simulation statistical fluctuations due to the limited size of the samples (approximately 10 units). Additional 20 units are added and corresponds to about 4σ confidence intervals. The same $\Delta\chi^2 = 30$ is applied to both the internal and external energy scale uncertainty analysis, thus leaving the choice less likely to bias the final result.

8.2 Performance evaluation

In this section, we discuss the results and performance of PROSPECT-II external calibration using the data and method described in the previous sections. The performance evaluation includes the compatibilities of the energy scale models obtained from both calibration schemes and also the estimated energy scale model systematic uncertainty contribution to the spectrum analysis. We also include the AmBe neutron source in the PROSPECT-II external calibration and investigated the benefits of the inclusion.

8.2.1 Energy scale model compatibility

Table 8.2 summarizes the best fit values of each parameter and associated uncertainties for the internal and external calibration schemes. The parameters for the external calibration energy model is compatible with the internal calibration within uncertainties. However, we can also conclude that the external calibration model uncertainties are less well constrained by almost a factor of two. In the next section, we will try to incorporate AmBe source's high energy γ-ray calibration point in the

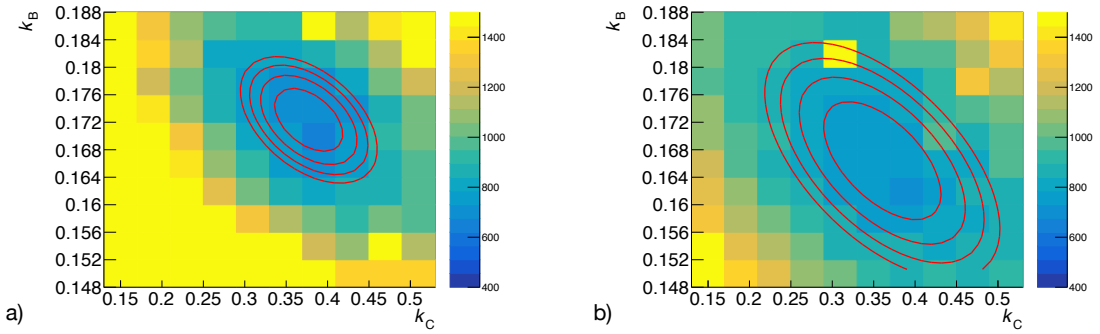


Figure 8.5: χ^2 distribution in energy scale parameter space for a) internal calibration and b) external calibration. Each $\chi^2(k_B, k_C)$ on the grid represents the corresponding detector response deviation from the calibration data with the optimized A value. The contours are generated with $\Delta\chi^2 = 30$ increments for illustration purposes. Note the intervals in the contours are larger for the external calibration. Thus, the best-fit is less well-constrained compared to the internal case, but is still well-defined.

Table 8.2: Nonlinear energy model fit parameters. The number of degrees of freedom (ndf) is different in two configurations due to change of region of interest in the energy spectrum.

Configuration	**A**	$\mathbf{k_B}$ **(cm/MeV)**	$\mathbf{k_C}$	$\boldsymbol{\chi^2}$	**ndf**
Internal	1.0080 ± 0.0020	0.1723 ± 0.0038	0.3772 ± 0.0338	657.6	330
External	1.0073 ± 0.0055	0.1664 ± 0.0070	0.3603 ± 0.0579	712.4	460

analysis chain to reduces parameter uncertainties specifically for the Cherenkov k_C. Given the reduced statistics of calibration events in the external configuration, the results presented here are the worst case scenario and improvements are expected from an actual PROSPECT-II detector setup, such as higher activity sources and longer calibration acquisition time.

Using the best fit values in Table 8.2 for internal and external calibration, both models demonstrate good agreement between data and simulations in the reconstructed energy spectrum and event multiplicity, as shown in Figure 8.6. Noticeable changes in both the spectral shape and multiplicity are apparent between internal and external configurations. The detector active volume only covers half of the solid angle of the external sources and thus is less likely to fully capture multiple γ-rays, causing the change of energy spectrum and downshift in event multiplicity shown in Figure 8.6. nH capture γ-ray rates are reduced due to less neutron captures internally, similar to the γ-ray source. The event multiplicity of nH event will suffer a similar downshift, depending on how deep the nH reaction happens in the fiducial volume. On the other hand, ^{12}B, generated intrinsically via the ^{12}C(n,p)^{12}B reaction in the liquid scintillator, is independent of the calibration setup. In the external calibration setup, both the γ-ray calibration sources and the 2.2 MeV γ-ray from neutron captures on hydrogen see a reduction of event statistics that could be compensated by higher activity sources in the actual P-II calibration.

8.2.2 Benefits of inclusion of AmBe source

The inclusion of high energy gamma calibration point would provide the better constrains on the Cherenkov parameter k_C. The ^{241}Am^{9}Be source provides neutrons and a correlated 4.4 MeV γ-ray via the ^{9}Be(α,n)^{12}C* reaction. The α particles are emitted from ^{241}Am. The half-life of the AmBe source is about 432.2 years with an average neutron energy of 4.2 MeV, up to 11 MeV. The AmBe source is of particular relevance to IBD neutrino detectors because the correlated pair of neutron and γ-ray

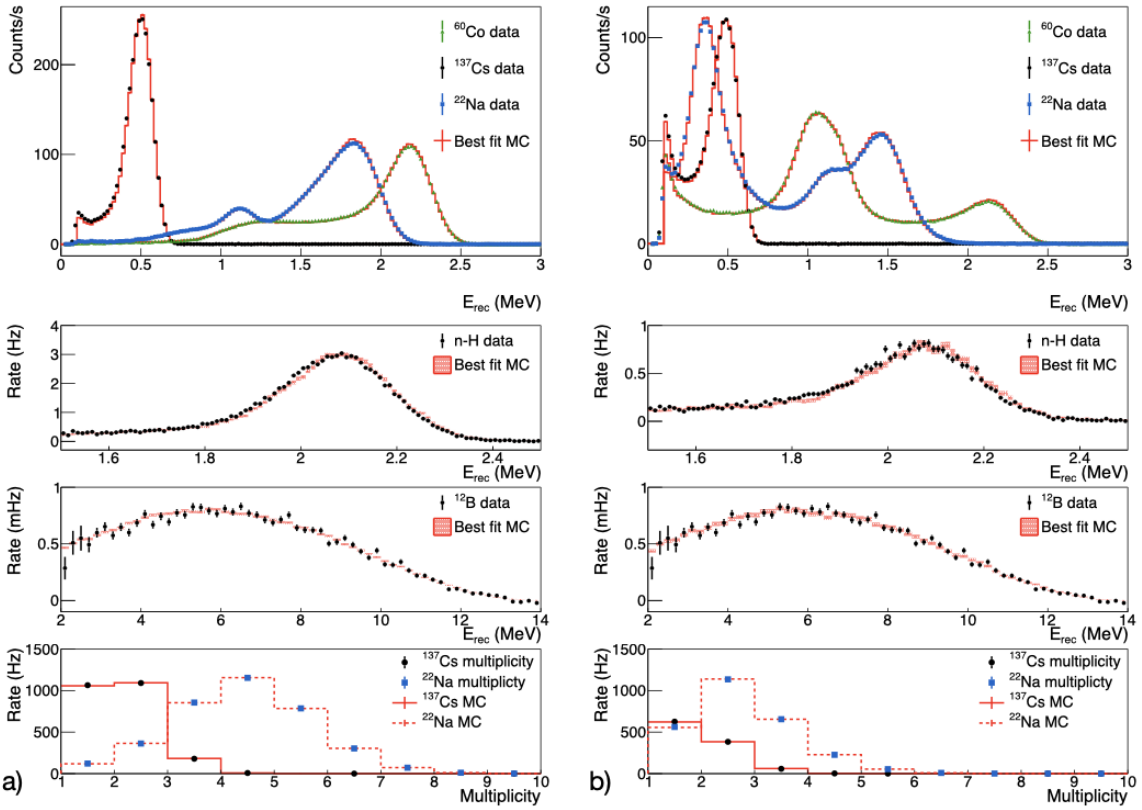


Figure 8.6: Data-simulation comparison of calibration source spectra and event multiplicity for a) best-fit internal energy scale model and b) best-fit external energy scale model. The reconstructed energy E_{rec} represents scintillator quenched visible energy, which is shifted to lower energy compared to the true gamma energies. External calibration events generally have lower event statistics and decreased event multiplicity due to smaller solid angle coverage. The external calibration spectra show more pronounced single-γ-ray photopeaks, with lower rates of total γ-ray photopeaks. The total χ^2 from both energy scale models are listed in Table 8.2.

is similar to IBD interactions and thus can be used as a tool to quantify neutron capture efficiency and neutron mobility. The 4.4 MeV γ-ray will provide additional calibration feature to further constrain k_B and k_C over the high-energy region.

The PROSPECT collaboration acquired an AmBe source near the end of the PROSPECT data-taking period and was not included in the calibrations and only used as a energy scale check for simulations, reported in previous published results [92]. However, without the inclusion additional high energy calibration feature provided by the AmBe source, the external calibration was shown to have worse calibration performance detailed in the previous section. We include the AmBe source to quantify the benefits of higher energy calibration features on future calibration campaigns. This inclusion of the AmBe source in the calibration data analysis is implemented via the Equation 8.5:

$$\chi^2_{\text{tot}} = \chi^2_{\text{data-MC}} + [\chi^2_{\gamma} + \chi^2_{\text{multi}}]_{\text{AmBe}}, \tag{8.5}$$

where $\chi^2_{\text{data-MC}}$ is defined in Equation 8.3 and the χ^2 contributions from the AmBe 4.4 MeV γ-ray reconstructed energy spectrum and event multiplicity are added to χ^2_{tot}. With the inclusion of the AmBe source in the calibration analysis, good agreement is found between the AmBe data and simulations, as shown in Figure 8.7 with χ^2_{AmBe}/ndf = 250.6/245.

The fit for other sources shows good agreement as well. For example, ^{22}Na energy spectrum contributes χ^2_{Na}/ndf = 254.7/106 with the inclusion of the AmBe source, compared to χ^2_{Na}/ndf = 254.3/106 without the AmBe source. The benefit of including an energetic calibration γ-ray is an improved constraint on the higher energy calibration. In particular, the k_C uncertainty is reduced, as shown in Table 8.3, where we see a 31 % improvement. The amount of the improvement is unlikely to increase in PROSPECT-II calibration run, given that the AmBe data we used contains sufficient events statistics for the purpose of the study.

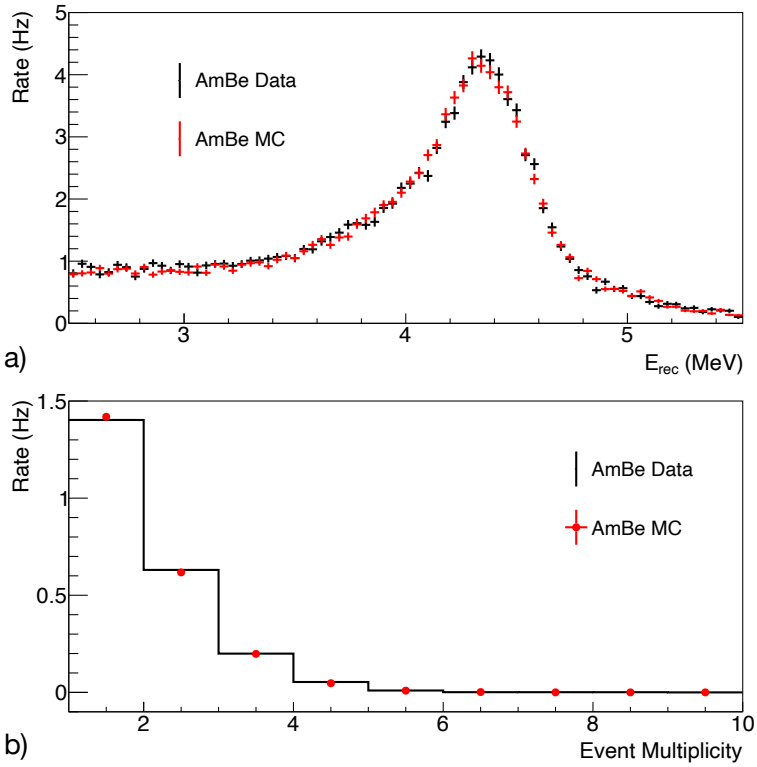


Figure 8.7: AmBe 4.4 MeV γ-ray energy spectrum in a) and event multiplicity distribution in b) using the external energy scale model obtained with AmBe calibration.

Table 8.3: Reduced k_C uncertainties with the inclusion of AmBe source in the external calibration.

Configuration	**A**	**k_B (cm/MeV)**	**k_C**
Internal	1.0080 ± 0.0020	0.1723 ± 0.0038	0.3772 ± 0.0338
External	1.0073 ± 0.0055	0.1664 ± 0.0070	0.3603 ± 0.0579
External with AmBe	1.0028 ± 0.0045	0.1658 ± 0.0061	0.4055 ± 0.0399

8.2.3 Energy scale model systematic uncertainty contribution

Another key performance metric of the PROSPECT-II calibration scheme is the systematic uncertainty contribution of the energy scale model. The desired goal is that the systematic uncertainty contribution from the external calibration scheme is less than the expected statistical uncertainties of the PROSPECT-II experiment, estimated by a combination of signal and background rate projections.

The energy scale systematic uncertainty will enter the analysis of sterile neutrino oscillation and neutrino spectrum of PROSPECT-II. To evaluate the impact, we begin by generating covariance matrices. The covariance matrix is generated by bin-by-bin comparison of sets of toy model spectra to the reference IBD spectrum. Reference IBD spectra are generated by passing the Huber-Mueller neutrino model predictions through the detector response, using the best-fit energy scale models. The toy model spectra are generated the same except the energy scale model parameters are uncorrelated Gaussian distributed with the best-fit model mean value and uncertainties. Reference IBD spectra contains 4×10^7 simulated IBD events. Toy model spectra contains 1×10^3 toy simulations, each of 4×10^6 simulated IBDs. Approximately 10 % of simulated IBDs pass the selection cuts in the fiducial volume for both the toy model and the reference IBD. The covariance matrix thus can be defined using the toy model spectra and reference IBD spectra information via the Equation 8.6:

$$\mathrm{Cov}[i,j] = 1/n \sum_n (T[i] - S[i]) * (T[j] - S[j]), \tag{8.6}$$

where $T[i]$ stands for the i-th bin content of the toy model spectra and $S[i]$ stands for the i-th bin content of the reference spectrum. Reduced covariance matrix can also be defined in Equation 8.7:

$$\mathrm{ReducedCov}[i,j] = 1/n \sum_n \frac{(T[i] - S[i]) * (T[j] - S[j])}{S[i] * S[j]}, \tag{8.7}$$

The relative uncertainty in each energy bin of the spectrum is by definition the square root of the diagonal elements of the reduced uncertainty covariance matrix. Figure 8.8 shows the relative uncertainty between 0.8 MeV and 7.2 MeV visible energy, which is the energy range where most detector IBD events fall from the reactor neutrino. The red curve represents the external calibration uncertainty with the AmBe source and the black curve stands for the default internal calibration uncertainty without the AmBe source. Similar level of systematic uncertainty contributions are found between these two calibration method. Estimated PROSPECT-II statistical uncertainty with background subtraction is also plotted in blue. The external calibration also has smaller or equal systematic uncertainty contributions compared the projected PROSPECT-II statistical uncertainty across the energy range of the spectrum, meeting the precision requirement of the PROSPECT-II program. The external calibration systematic uncertainties can be further reduced by one or combinations of higher activity calibration sources and longer calibration acquisition time, resulting even smaller systematic uncertainties than the projected two years' PROSPECT-II neutrino statistics with full background subtraction, ensuring that the energy scale model will not be the dominant uncertainty contributor for the improved PROSPECT-II detector.

8.3 Discussion on specific concerns related to the upgrades

So far we demonstrated the feasibility of an external energy scale calibration scheme for the upgraded PROSPECT-II detector. However, the changes in the design of the PROSPECT-II detector introduces additional concerns, including the detector-source stand-off distance, increased backgrounds in the location of the external calibration source, and the impact of inter-segment cross-talk. Note that the change in size and geometry of the detector, and dimensions of each segment can also impact the

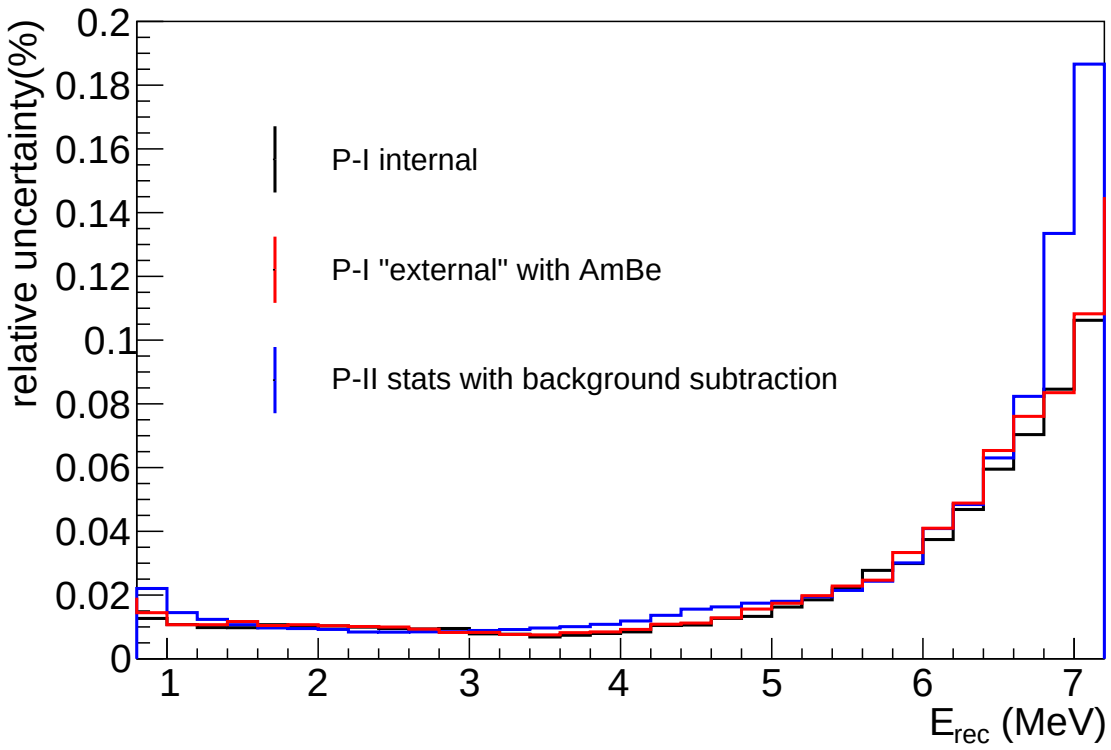


Figure 8.8: Relative systematic uncertainty from the energy scale model is plotted in the energy range where most IBD events fall. P-I internal in black represents the uncertainty from the P-I internal calibration without the AmBe source. P-I "external" in red represents the uncertainty from the P-II type external calibration study with the AmBe source. P-II signal statistics with background subtraction in blue includes the estimated statistical uncertainty from the expected IBD statistics in the P-II detector and estimated background statistics.

performance of the external calibration technique. But we expect the impact to be minimal since the inner design elements of the PROSPECT-II detector remain largely the same. Hence we will only discuss the impact of the stand-off distance, increased backgrounds of the external calibration source location, and inter-segment cross-talk.

First, the displacement of the calibration sources in the external position introduces additional stand-off distance between the detector active volume and the source. This displacement is estimated around $\sim$ 3 cm from the center of the source tube and to boundary of the active liquid scintillator volume, illustrated in Figure 8.9 below. If the location of the external source cannot be precisely determined, the stand-off distance would introduce additional systematic error and thus impact the performance of the external calibration scheme. Here we want to evaluate the precision requirement of the stand-off distance to have minimal impact on the calibration performance, by comparing MC spectra at different stand-off distances to the spectrum at nominal position. In the MC simulation studies, we offset the external calibration source from its nominal position by 1, 2, 5 and 10 times the unit of 1.4 mm, which corresponds to $\pm$1% of the segment width. In Figure 8.10, MC simulation spectra of additional source stand-off distance of 1.4 mm further away from the nominal position show negligible differences in the spectrum, with a χ^2/ndf=250.6/245. At other offset positions, apparent spectral deviations are visible with increasing χ^2/ndf values, 1.25, 1.74 and 4.19 respectively.

A full external calibration analysis should be used to evaluate the impact of the stand-off distance if the precision of the source can't be precisely determined. Since a position error of $\pm$1.4 mm or $\pm$1% of the segment width is shown to have minimal impact on the MC spectra, and the same requirement is achievable through careful engineering, we conclude that the a positioning requirement of $\pm$1.4 mm will have minimal impact on the desired energy scale uncertainty.

Since the calibration sources are deployed in external positions and the external calibration scheme will primarily use data from segments on the edge, the performance

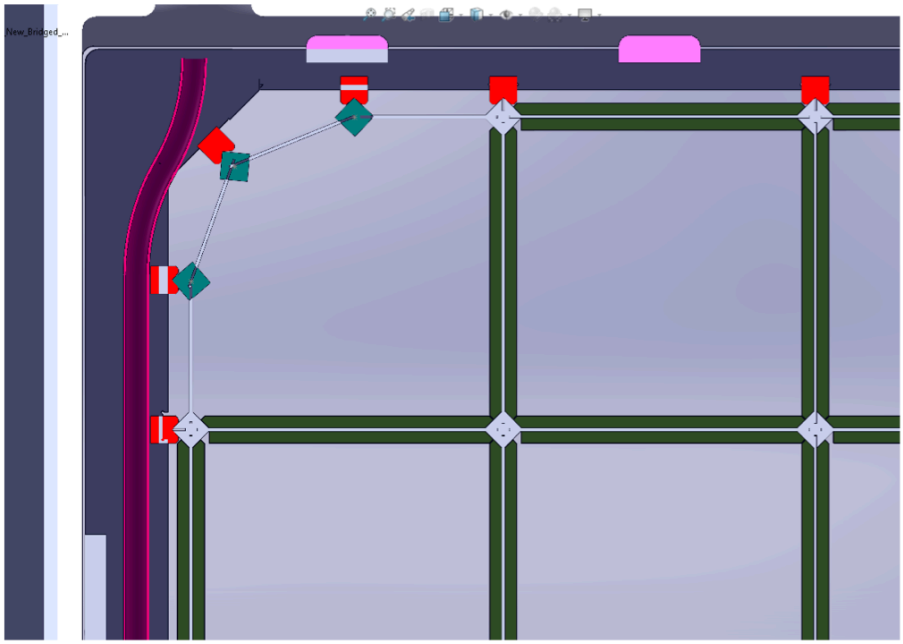


Figure 8.9: The schematic shows the stand-off distance introduced in the upgraded PROSPECT-II detector. The 3/8 inches calibration source tube can be inserted from the top of the detector, shown in red. The green are supporting rods that house the reflective panels. The center of the source tube to the boundary of the active liquid scintillator volume is estimated to be $\sim$ 3 cm.

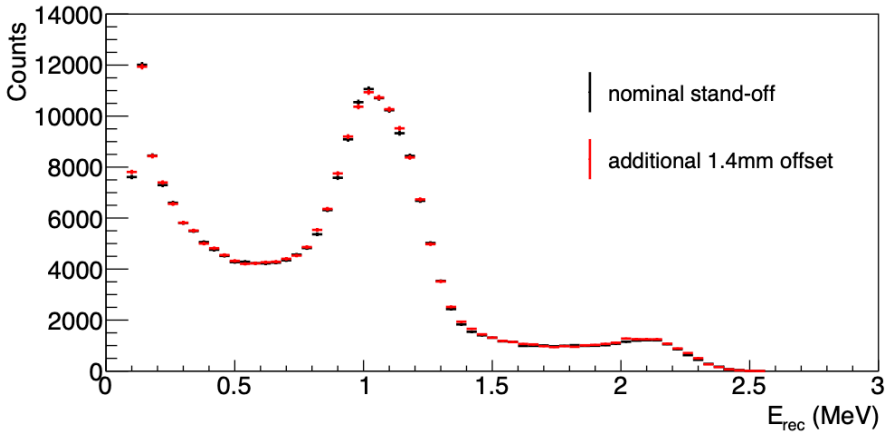


Figure 8.10: MC ^{60}Co spectrum externally deployed with a stand-off distance of 1.4 mm further away from the nominal position, with a χ^2/ndf=250.6/245.

will likely suffer from increased γ-ray backgrounds, in comparison to the segments in the center of the active liquid scintillator volume. Note that the external calibration sources sits outside the active liquid scintillator volume but still inside the PROSPECT-II exterior shielding packages. Using γ-ray background observed in the PROSPECT-I detector, an increase γ-ray background rates by a factor of four in the outer layers of the detector segments compared to the interior segments of the detector. In Figure 8.11, a map of γ-ray events background rates are shown as a function of segment numbers. In the simulations, we can artificially increase the background rates by a factor of four, and found that these increased γ-ray background rates translates to a $\sim$3-4% increase in uncertainties in the reconstructed energy spectrum and event multiplicity. The reason behind this is because the radioactive calibration source we used are fairly strong compared to the low γ-ray background rates as a results of the comprehensive passive shielding installed surrounding the detector. This also means that the increased uncertainties in the reconstructed energy spectrum and event multiplicity by $\sim$3-4% can be easily mitigated by using a strong source in PROSPECT-II calibration.

The final concern we want to address is the cross-talk between the neighbor segments, introduced by the acrylic window designed to separates the PMT housings and the active liquid scintillator volume. The new acrylic window eliminated the possibilities of PMT housing base corroded by liquid scintillator, thus ensuring the long-term stability of the PROSPECT-II detector performance. The design change was based on the gradual PMT failures over the course of the data-taking observed in the PROSPECT-I detector, leaving detector performance degraded with less neutrino statistics and weaker background rejection capabilities. However, as we stated above, the acrylic window also introduces inter-segments cross-talks. Estimated with optical MC simulations and benchtop testing, the acrylic window introduces $\sim$0.5% cross-talk between adjacent segments and $\sim$0.01% cross-talk diagonal segments. In Figure 8.12 In order to investigate the impact of the cross-talk on the calibration performance, we need to introduce artificial cross-talk to the PROSPECT-I calibration data and

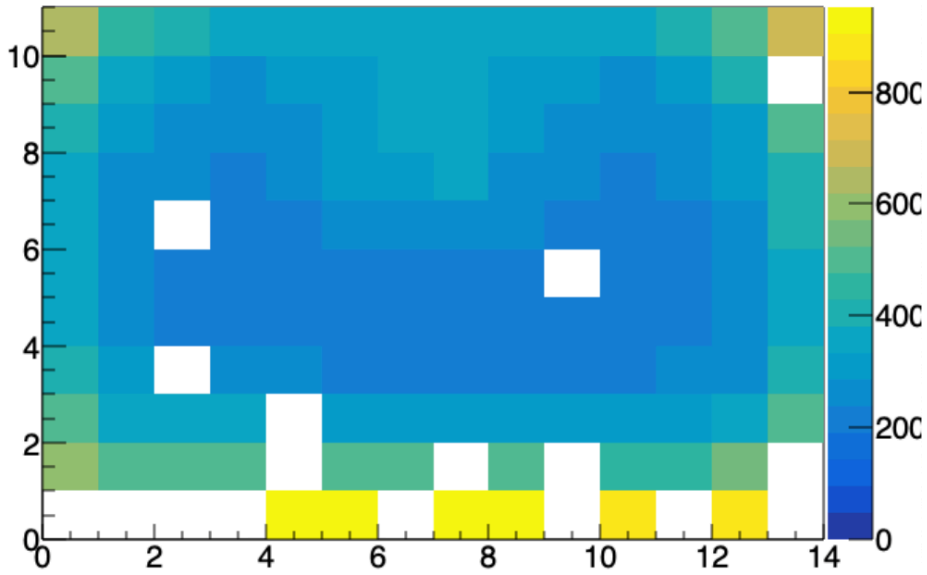


Figure 8.11: The color represents the γ-ray events rates as a function of segments. Approximately a factor of four is observed as a ratio of γ-ray rates in the edge segments over the inner segments.

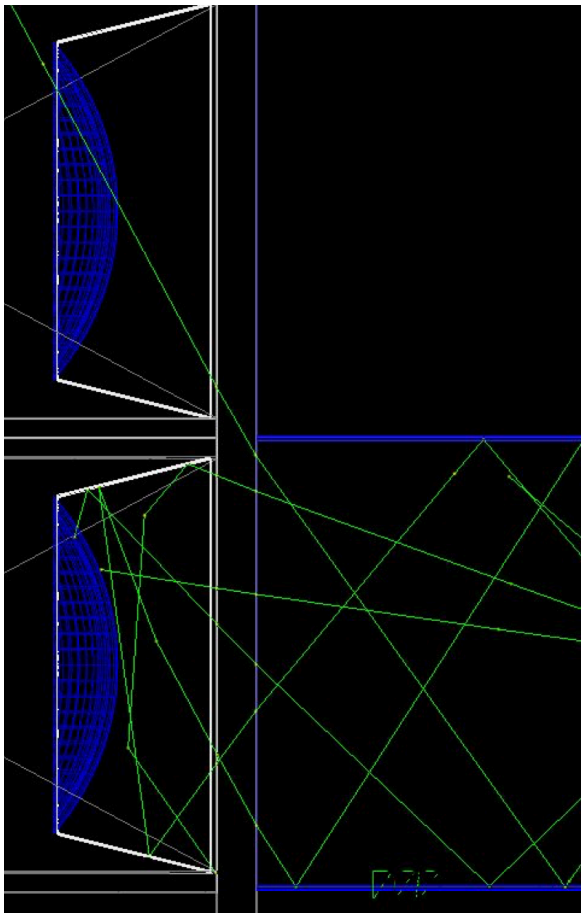


Figure 8.12: MC simulations of neighbor cross-talk introduced by the acrylic window. The γ-ray tracks are illustrated in green, two neighbor PMT surfaces are located on the left. The acrylic window was the middle piece with 1/4 inches thickness. Source:[117]

as well as simulations, and the whole energy scale calibration analysis is repeated. The implementation of the artificial cross-talk also takes into account the non-uniform longitudinal dependence along the segment based on the optical simulations. The magnitude of the cross-talk varies non-linearly by about 80% as the γ-ray source moves from the center to both ends of the segments. This cross-talk re-analysis can be done in either the internal setup or the external with similar results. Using the internal calibration method, the effective energy scale models obtained with $\sim$2% cross-talk shows no significant differences in the energy scale model parameters, as shown in Table 8.4. Note the 2% cross-talk corresponds to the total cross-talk level with $\sim$0.5% cross-talk between adjacent segments mentioned above. Another concern needs to be addressed that the level of the cross-talk will not be exactly known for the simulations and *in-situ* measurements. Thus, we investigated the required precision by applying different levels of cross-talk to the data and simulations. For example, we obtain a similar effective energy scale model using an artificial cross-talk of 2% applied to data and 2.5% applied to simulation, as shown in Table 8.4. Note that a small increase in the A parameter is also observed, compensating for more light lost to neighboring segments in the data and simulation. The light loss is due to the fact that the cross-talk events are very low energy and fall below the per-segment detection threshold. We deem the precision of up to 0.5% is adequate for cross-talk measurement precision. With the artificial cross-talk analysis setup ready for PROSPECT-II detector, further precision investigation can be done if 0.5% cross-talk measurement precision is not adequate. The energy scale model with various cross-talk levels are summarized in Table 8.4, and good agreement in energy spectrum and event multiplicity is also observed.

To summarize, we demonstrated that an external source calibration strategy for P-II is feasible, by using PROSPECT-I data and a well-benchmarked MC. We plan to include an AmBe neutron source in the external calibration setup in order to obtain required performance and precision. The estimated systematic uncertainty from the external energy scale model is also shown to meet the physics goals of the

program. We also performed additional studies on topics specific to the PROSPECT-II detector, providing design guidance on detector-source stand-off distance, increased γ-ray backgrounds at external calibration locations, and inter-segment crosstalk. The findings we found may have values for other segmented reactor antineutrino detectors for basic science or applications.

Table 8.4: Effective energy scale model parameters in the presence of inter-segment cross-talk for an internal calibration setup. External calibration with cross-talk yield similar results.

Configuration	**A**	$\mathbf{k_B}$ **(cm/MeV)**	$\mathbf{k_C}$
No cross-talk	1.0080 ± 0.0020	0.1723 ± 0.0038	0.3772 ± 0.0338
2 % sim & 2 % data	1.0100 ± 0.0020	0.1734 ± 0.0037	0.3783 ± 0.0357
2.5 % sim & 2 % data	1.0130 ± 0.0010	0.1744 ± 0.0036	0.3720 ± 0.0350

Chapter 9

Liquid scintillator calibration using DT generators

In the previous chapter, we looked into using external and intrinsic sources to calibrate the PROSPECT AD or the liquid scintillator in a non-intrusive way. Given the physics of the PROSPECT detector in its root is neutron physics, we explore another different complementary calibration approach using external compact commercial neutron source that fit in the footprint of detector's top space or the side, as illustrated in Figure 9.1. The on-demand mono-energetic neutron source can benefit the detector position and PSD calibrations, detector stability monitoring, and flux analysis, which requires determination of neutron tagging efficiency. By relating the associated α-particle to the position of the neutron recoil events inside the detector, the neutron deposited energy in the liquid scintillator follows $\cos\theta$ kinetic distributions, allowing for determinations of the detector neutron response in the liquid scintillator over a wide range of deposited energy.

We first present the basic physics of DT neutron generators and describe possible application and benefits. We also performed simulation studies based on the **PROSPECT-G4** packages programmed for PROSPECT-I.

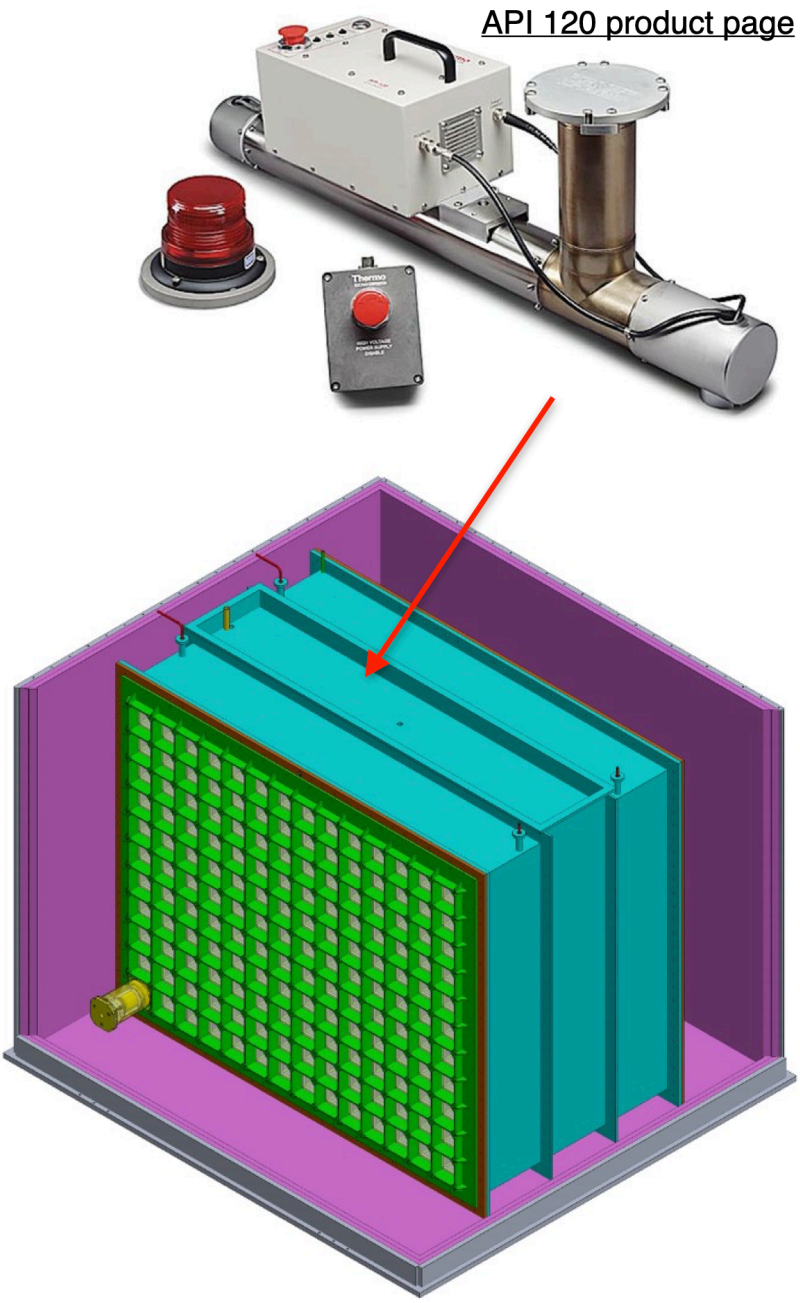


Figure 9.1: Illustrations of the DT neutron generator installed on top the PROSPECT-II detector. Portable API 120 commercial neutron generator [128] is displayed as an example.

9.1 Physics of DT neutron generator

Neutron generators are on-demand neutron source devices that contain typically a compact linear particle accelerator and a target loaded with deuterium or tritium. The ions of deuterium or tritium are accelerated into the target, creating fusion reactions of either a pair of deuterium atoms (D+D) or a deuterium and a tritium (D+T),

$$\mathrm{D} + \mathrm{T} \rightarrow n + {}^{4}\mathrm{He} \tag{9.1}$$

$$\mathrm{D} + \mathrm{D} \rightarrow n + {}^{3}\mathrm{He} \tag{9.2}$$

The neutron energy of the two primary reactions are 2.5 MeV and 14.1 MeV for DD and DT, respectively. The DT reactions are more widely used in neutron generators than the DD reaction because the yield of the DT reaction is much higher than that of the DD reaction, as illustrated in Figure 9.2. The neutrons produced in the two primary reactions are emitted anisotropically from the target point. For DT neutron generators, the neutron beam can be "collimated" by detecting and correlating the outgoing neutron particle and associated 3.5 MeV alpha particle in space and time with the neutron.

One of the commercially available DT neutron generators with low profile is the API 120 Neutron Generator [128] from Thermo Scientific company, as shown in Figure 9.1. This DT generator is very compact and portable with the weight below 15 kg. The DT generator is also equipped with a built-in alpha detector for the identification of alpha-neutron time and space correlation. The power consumption of the device is well below 50 watts, and the device can produce a directional neutron flux of 10^7 n/s with a lifetime of 550 days' of continuous operation, enough for the two years' operation of the PROSPECT-II detector.

Compared to the common neutron sources for detector calibrations, such as ^{252}Cf used in the calibration campaign, DT generators can provide higher rates of

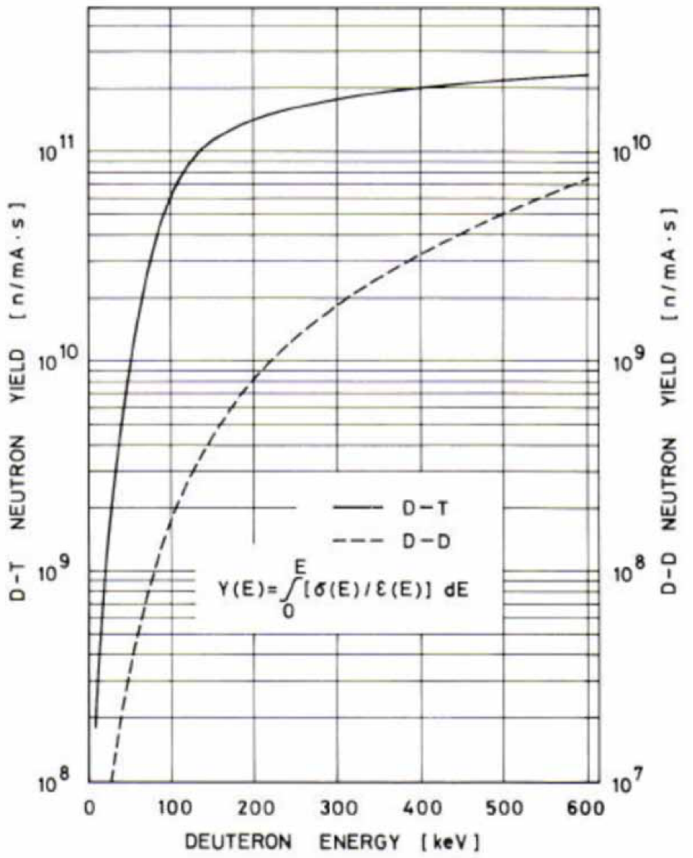


Figure 9.2: Comparison of the neutron yield as a function of deuteron energy for DD and DT reactions. Source:[129]

directional and more penetrating mono-energetic neutrons. As mentioned before, the neutrons emitted from DT generators allow for correlation based cut analysis for reduced background events compared to ^{252}Cf in a highly neutron rich reactor experimental hall.

9.2 Complementary calibration using external DT generators

In addition to the aforementioned benefits for low level detector position and PSD calibration, stability monitoring and absolute flux analysis, the inclusion of high energetic neutron generator would also greatly benefit the energy scale calibration. In PROSPECT-I calibration campaigns, a variety of gamma sources were used, as was discussed in Chapters 5. The energy of those gamma sources were mostly in the lower energy regions, with the only high energy calibration up to 14 MeV from the intrinsic ^{12}B electronic events. The electronic detector response is well characterized in Chapter 5. And if we can also characterize the detector response to nuclear recoil events, it would allow us to use neutron recoil calibrations to continuously monitor the response of the detector, provide more nH capture gamma for energy scale calibration events, even lead to better understanding of the dominant fast neutron backgrounds in the reactor vicinity.

The characterization of the detector response to neutron recoils up to 14 MeV can be achieved by time-of-flight method [130]. Typically, the experimental setup requires a neutron detector placed at various angles θ from the liquid scintillator, as illustrated in Figure 9.3. The scattered neutron energy can be expressed as a function of the incident energy E_n and the angle θ, assuming neutron elastic scattering,

$$E_{n'} = E_n \cos^2 \theta, \tag{9.3}$$

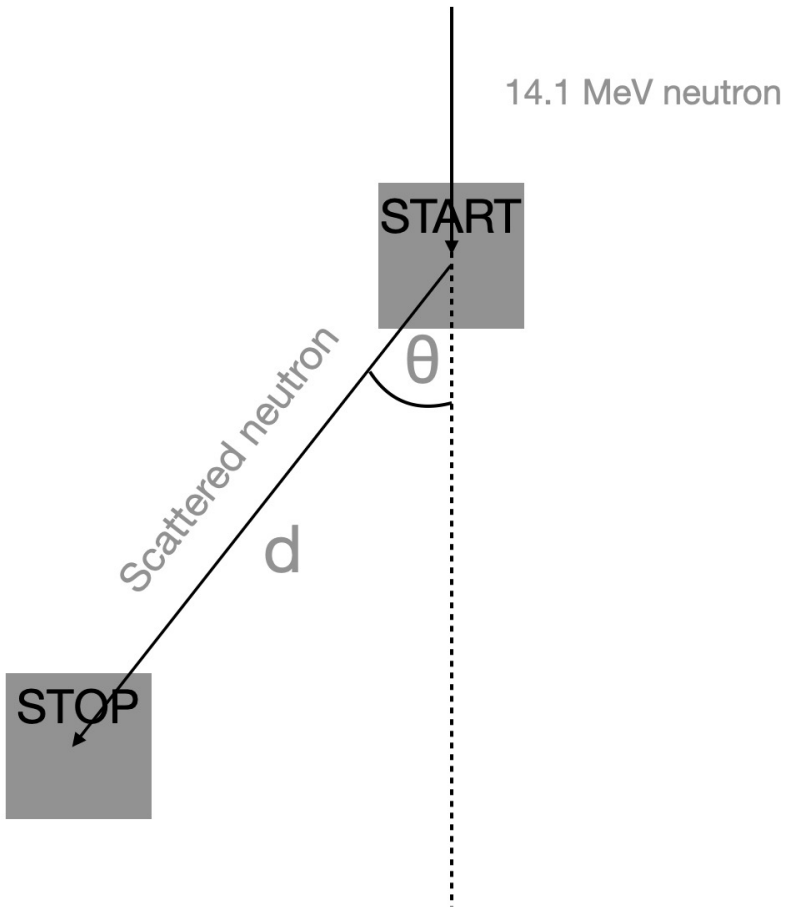


Figure 9.3: Schematics of the experimental setup of liquid scintillator neutron response. The START is the liquid scintillator and the STOP is the neutron detector placed at d distance that provides both timing and angle information.

$E_{n'}$ can be also expressed using the time-of-flight method, assuming the kinematics are non-relativistic.

$$E_{n'} = \frac{1}{2}(d/t)^2 m_n, \tag{9.4}$$

where d is the distance between the two detectors, t is the time-of-flight, and m_n is the mass of the neutron. The deposited recoil energy in the liquid scintillator is expressed as the energy difference between the same incident and recoil neutron,

$$E_r = E_n - E_{n'}, \tag{9.5}$$

By adjusting the position of the STOP neutron detector relative to the liquid scintillator, a wide range of deposited recoil energy can be achieved. This idea can be applied to the PROSPECT detector extremely easily using an externally deployed DT neutron generator by noting the PROSPECT detector is highly segmented. A schematic is depicted in Figure 9.4.

The free choice of the STOP segment in the PROSPECT detector relative to the incident entry segment allows for a wide range of scattering angles. The energetic mono-energy neutrons from the DT generator are more penetrating than those from a ^{252}Cf source. The high penetration of the DT neutrons provides a wider choice of angle θ and enables studies of neutron transport in the detector.

9.3 MC simulation results and future works

This section will present the results of the neutron detector response using existing **PROSPECT-G4** packages. Mono-energetic neutron source is placed above the PROSPECT AD detector along the $z = 0$ plane and emits vertically downward with 14.1 MeV energy. The definition of the scattering angle θ needs to be modified to reflect the 3D geometry, accounting for the additional z dimension. Additionally, we have to assume the neutron recoil happens at the center of each segment, which in turn would reduce the energy resolution of the scattered neutron. We define the

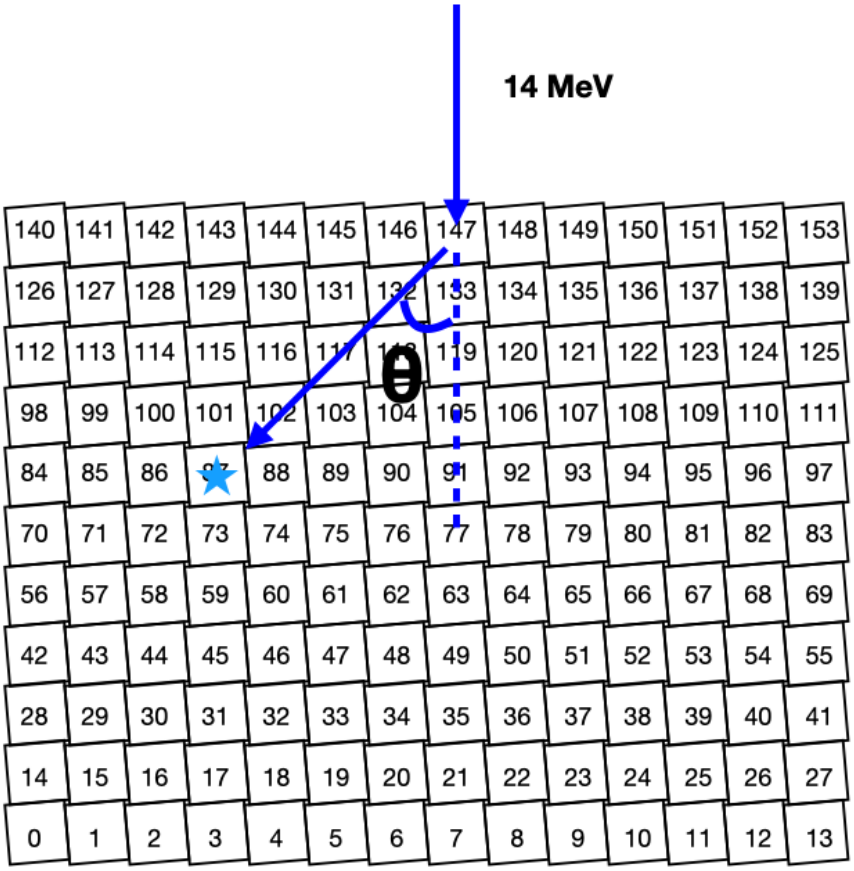


Figure 9.4: Schematic of neutron scattering in the highly segmented PROSPECT detector. Mono-energetic neutrons from the DT generator are incident from the top of the detector. The neutron scatters off the entry segment 147 and subsequently on segment 87, with a scattering angle θ. The star represents the STOP segment used for determination of the scattering angle.

vertical y-axis and horizontal x-axis in Figure 9.4. The z-axis is defined into the page. The relative distance to the entry segment is defined as $\Delta|x|$, $\Delta|y|$, $\Delta|z|$, leading the full definition of the scattering angle θ as follows,

$$\theta = \arctan \frac{\sqrt{\Delta|x|^2 + \Delta|z|^2}}{\Delta|y|}, \tag{9.6}$$

The energy of the scatter neutron energy $E_{n'}$ follows directly from Equation 9.3. The recoil energy deposited in the PROSPECT liquid scintillator E_r is defined as,

$$E_r = 14.1 \times (1 - \cos^2\theta)\text{MeV}, \tag{9.7}$$

A preliminary relation between the scintillation light and recoil energy is depicted in Figure 9.5. This relation only applies to the high PSD proton recoil events in Figure 6.2, not the higher PSD band that was caused by recoils of heavier charged particles such as alpha particles or carbon. The recoil events are selected by choosing the first recoil event at the entry segment and subsequent scattering at the final segment with relative angle θ and their PSD values residing in the proton recoil band. The determined relation between the recoil energy and the scintillation light could potentially offer complementary detector energy scale calibration on-demand or continuously. The author of the work [131] fitted the Birks constant using the neutron response for a specific detector setup and material. Furthermore, it was also suggested in the work [132] that the Birks constant is independent of the ionizing particle type, allowing for extrapolation of the liquid scintillator response to other types of heavier particles. Future works includes refining the current study in terms of simulation and analysis cuts, extrapolating the Birks constant from the fitted detector neutron response as done in reference work [131], and possibly obtaining LS response to other ionizing particles. To summarize, DT neutron generators are compact devices that provide large flux of high penetrating neutrons. The compactness, mobility, and relative low cost of neutron generators make them great complementary devices

for on-demand position and PSD calibrations, continuous detector monitoring, or determination of neutron tagging efficiency. We also simulated detector recoil neutron response using mono-energetic 14.1 MeV neutron source. The scintillation light from the neutron recoils could be used in determination of detector energy scale calibration over a wider range of visible energy up to 10 MeV.

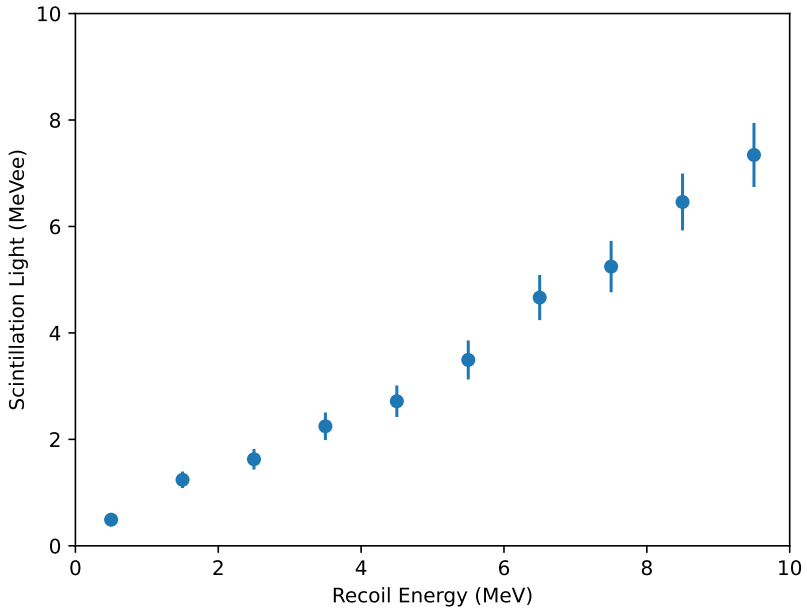


Figure 9.5: Scintillation light as a function of recoil energy. The recoil energy is calculated in Equation 9.7.

Chapter 10

Conclusion

PROSPECT is a world-leading short baseline neutrino experiment that was designed to make high precision measurement of the ^{235}U antineutrino energy spectrum and model-independent searches for eV-scale sterile neutrino oscillation channels from the HEU research reactor at High Flux Isotope Reactor. The first two hours of reactor-on data-taking confirmed the observation of reactor antineutrinos from the reactor at 5σ statistical significance. The early sterile neutrino oscillation analysis disfavored the best-fit of the Reactor Antineutrino Anomaly at 2.2σ confidence level, rejecting the hypothesis of a hypothetical sterile neutrino, and the energy spectrum analysis of ^{235}U antineutrino showed consistency with the spectral bump in the neutrino energy region of 5-7 MeV observed in LEU power reactor based experiments. These results were further improved by a subsequent complete analysis of the whole PROSPECT dataset collected over the course of less than a year, with reported statistics of over 50,000 neutrino interactions observed. Recently, a final data analysis reported double effective statistics compared to the previous PROSPECT results, thanks to the efforts to make use of multi-period divisions of the dataset and inclusion of single-end event reconstruction to minimize the statistical impact introduced by the increasing number of PMT failures over the course of data-taking.

This dissertation reflects my contributions to the analysis and development of the PROSPECT experiment, including the discussed optimization of IBD event selection cuts and a performance and feasibility demonstration of an alternative energy scale calibration strategy for the upgraded detector PROSPECT-II. The implementation and optimization of event selection rules enabled energy spectral analysis of ^{235}U antineutrino and sterile neutrino oscillation searches by mitigating the challenging on-surface and reactor related backgrounds. The optimization maximized the statistical power of the PROSPECT dataset, yielding an antineutrino spectrum with over 50,000 neutrino interactions. With the conclusion of the final analysis of the whole PROSPECT dataset, an upgraded PROSPECT-II detector is planned by the collaboration to further expand the physics capability of the experiment. The upgrades will leverage existing experiment investments and expertise, resolve technical issues causing the PMT failures, and introduce detector design changes to improve detector long-term stability. One of the main design changes in the PROSPECT-II detector, i.e. the separation of the PMT modules and the liquid scintillator volume by an acrylic window, necessitates an external calibration scheme. This dissertation demonstrates the feasibility of the external calibration strategy for PROSPECT-II, using only existing PROSPECT-I calibration dataset and well-benchmarked simulation packages. The estimated systematic uncertainty from the external energy scale model is shown to meet the physics goals of the program. The new external calibration strategy requires an additional energetic gamma calibration point, provided by the AmBe neutron source , which was not fully utilized in previous analysis. This dissertation also investigates additional topics specific to the detector upgrade changes, providing design guidance on detector-source stand-off distance, increased γ-ray backgrounds at external calibration locations, and inter-segment crosstalk.

The inclusion of a DT neutron generator in PROSPECT-II detector is proposed. The deployment of such high energetic neutron source from a low profile DT generator provides means of continuous monitoring of the detector time stability, offers dataset

for possible determination of neutron detection efficiency for absolution flux analysis and understanding of the neutron transport in the detector, and complementary liquid scintillator calibrations such as position and PSD. MC simulation results of the detector neutron response are obtained using fast neutron scatting method.

Bibliography

[1] M. Andriamirado et al. Calibration strategy of the PROSPECT-II detector with external and intrinsic sources. *JINST*, 18(06):P06010, 2023. 3

[2] J Chadwick. Intensitätsverteilung im magnetischen Spectrum der β-Strahlen von radium B + C. *Verhandl. Dtsc. Phys. Ges.*, 16:383, 1914. 4

[3] Charles Drummond Ellis and W. A. Wooster. The average energy of disintegration of radium e. *Proceedings of The Royal Society A: Mathematical, Physical and Engineering Sciences*, 117:109–123, 1927. 4, 5

[4] E. Fermi. An attempt of a theory of beta radiation. 1. *Z. Phys.*, 88:161–177, 1934. 6

[5] H. Bethe and R. Peierls. The 'neutrino'. *Nature*, 133:532, 1934. 6

[6] F. Reines, C. L. Cowan, F. B. Harrison, A. D. McGuire, and H. W. Kruse. Detection of the free anti-neutrino. *Phys. Rev.*, 117:159–173, 1960. 7, 8

[7] G. Danby, J. M. Gaillard, Konstantin A. Goulianos, L. M. Lederman, Nari B. Mistry, M. Schwartz, and J. Steinberger. Observation of High-Energy Neutrino Reactions and the Existence of Two Kinds of Neutrinos. *Phys. Rev. Lett.*, 9:36–44, 1962. 7

[8] K. Kodama et al. Observation of tau neutrino interactions. *Phys. Lett. B*, 504:218–224, 2001. 7

[9] Y. Fukuda et al. Evidence for oscillation of atmospheric neutrinos. *Phys. Rev. Lett.*, 81:1562–1567, 1998. 9, 10, 11, 25, 26

[10] Q. R. Ahmad et al. Measurement of the rate of $\nu_e + d \rightarrow p + p + e^-$ interactions produced by ^{8}B solar neutrinos at the Sudbury Neutrino Observatory. *Phys. Rev. Lett.*, 87:071301, 2001. 9, 12

[11] Rabindra N. Mohapatra and Goran Senjanovic. Neutrino Mass and Spontaneous Parity Nonconservation. *Phys. Rev. Lett.*, 44:912, 1980. 10

[12] G. Adhikari et al. nEXO: neutrinoless double beta decay search beyond 10^{28} year half-life sensitivity. *J. Phys. G*, 49(1):015104, 2022. 10

[13] N. Abgrall et al. The Large Enriched Germanium Experiment for Neutrinoless Double Beta Decay (LEGEND). *AIP Conf. Proc.*, 1894(1):020027, 2017. 10

[14] Raymond Davis, Jr., Don S. Harmer, and Kenneth C. Hoffman. Search for neutrinos from the sun. *Phys. Rev. Lett.*, 20:1205–1209, 1968. 10

[15] W. Hampel et al. GALLEX solar neutrino observations: Results for GALLEX IV. *Phys. Lett. B*, 447:127–133, 1999. 10

[16] J. N. Abdurashitov et al. Results from SAGE. *Phys. Lett. B*, 328:234–248, 1994. 10

[17] Y. Fukuda et al. Solar neutrino data covering solar cycle 22. *Phys. Rev. Lett.*, 77:1683–1686, 1996. 10

[18] Masayuki Nakahata et al. Atmospheric Neutrino Background and Pion Nuclear Effect for Kamioka Nucleon Decay Experiment. *J. Phys. Soc. Jap.*, 55:3786, 1986. 10

[19] D. Casper et al. Measurement of atmospheric neutrino composition with IMB-3. *Phys. Rev. Lett.*, 66:2561–2564, 1991. 10

[20] Ziro Maki, Masami Nakagawa, and Shoichi Sakata. Remarks on the unified model of elementary particles. *Prog. Theor. Phys.*, 28:870–880, 1962. 12

[21] V. N. Gribov and B. Pontecorvo. Neutrino astronomy and lepton charge. *Phys. Lett. B*, 28:493, 1969. 12

[22] R. L. Workman et al. Review of Particle Physics. *PTEP*, 2022:083C01, 2022. 14, 15

[23] N. S. Bowden. PROSPECT – A precision reactor oscillation and spectrum experiment. *Int. J. Mod. Phys. Conf. Ser.*, 50:2060001, 2020. 14

[24] N. Allemandou et al. The STEREO Experiment. *JINST*, 13(07):P07009, 2018. 14, 32

[25] A. C. Hayes and Petr Vogel. Reactor Neutrino Spectra. *Ann. Rev. Nucl. Part. Sci.*, 66:219–244, 2016. 18, 117

[26] D. A. Brown et al. ENDF/B-VIII.0: The 8th Major Release of the Nuclear Reaction Data Library with CIELO-project Cross Sections, New Standards and Thermal Scattering Data. *Nucl. Data Sheets*, 148:1–142, 2018. 18

[27] M. R. Bhat. Evaluated nuclear structure data file (ensdf). In Syed M. Qaim, editor, *Nuclear Data for Science and Technology*, pages 817–821, Berlin, Heidelberg, 1992. Springer Berlin Heidelberg. 18

[28] Xin Qian and Jen-Chieh Peng. Physics with Reactor Neutrinos. *Rept. Prog. Phys.*, 82(3):036201, 2019. 19

[29] F. Von Feilitzsch, A. A. Hahn, and K. Schreckenbach. EXPERIMENTAL BETA SPECTRA FROM PU-239 AND U-235 THERMAL NEUTRON FISSION PRODUCTS AND THEIR CORRELATED ANTI-NEUTRINOS SPECTRA. *Phys. Lett. B*, 118:162–166, 1982. 20

[30] K. Schreckenbach, G. Colvin, W. Gelletly, and F. Von Feilitzsch. DETERMINATION OF THE ANTI-NEUTRINO SPECTRUM FROM U-235 THERMAL NEUTRON FISSION PRODUCTS UP TO 9.5-MEV. *Phys. Lett. B*, 160:325–330, 1985. 20, 21

[31] A. A. Hahn, K. Schreckenbach, G. Colvin, B. Krusche, W. Gelletly, and F. Von Feilitzsch. Anti-neutrino Spectra From ^{241}Pu and ^{239}Pu Thermal Neutron Fission Products. *Phys. Lett. B*, 218:365–368, 1989. 20

[32] N. Haag, A. Gütlein, M. Hofmann, L. Oberauer, W. Potzel, K. Schreckenbach, and F. M. Wagner. Experimental Determination of the Antineutrino Spectrum of the Fission Products of ^{238}U. *Phys. Rev. Lett.*, 112(12):122501, 2014. 20

[33] A. C. Hayes, J. L. Friar, G. T. Garvey, Gerard Jungman, and Guy Jonkmans. Systematic Uncertainties in the Analysis of the Reactor Neutrino Anomaly. *Phys. Rev. Lett.*, 112:202501, 2014. 20

[34] Patrick Huber. On the determination of anti-neutrino spectra from nuclear reactors. *Phys. Rev. C*, 84:024617, 2011. [Erratum: Phys.Rev.C 85, 029901 (2012)]. 20

[35] Th. A. Mueller et al. Improved Predictions of Reactor Antineutrino Spectra. *Phys. Rev. C*, 83:054615, 2011. 20

[36] P. Vogel and John F. Beacom. Angular distribution of neutron inverse beta decay, anti-neutrino(e) + p —> e+ + n. *Phys. Rev. D*, 60:053003, 1999. 22

[37] Glenn R. Jocher, Daniel A. Bondy, Brian M. Dobbs, Stephen T. Dye, James A. Georges, John G. Learned, Christopher L. Mulliss, and Shawn Usman. Theoretical antineutrino detection, direction and ranging at long distances. *Phys. Rept.*, 527:131–204, 2013. 24

[38] F. Reines, H. W. Sobel, and E. Pasierb. Evidence for Neutrino Instability. *Phys. Rev. Lett.*, 45:1307, 1980. 25

[39] H. Kwon, F. Boehm, A. A. Hahn, H. E. Henrikson, J. L. Vuilleumier, J. F. Cavaignac, D. H. Koang, B. Vignon, F. Von Feilitzsch, and R. L. Mossbauer. Search for Neutrino Oscillations at a Fission Reactor. *Phys. Rev. D*, 24:1097–1111, 1981. 25

[40] Y. Declais et al. Search for neutrino oscillations at 15-meters, 40-meters, and 95-meters from a nuclear power reactor at Bugey. *Nucl. Phys. B*, 434:503–534, 1995. 25

[41] M Abbes et al. The Bugey-3 neutrino detector. *Nucl. Instrum. Meth. A*, 374:164–187, 1996. 25

[42] J. L. Vuilleumier et al. New Limits on Oscillation Parameters for Electron Anti-neutrinos. *Phys. Lett. B*, 114:298, 1982. 25

[43] K. Gabathuler, F. Boehm, F. von Feilitzsch, J. L. Gimlett, H. Kwon, R. L. Mossbauer, J. L. Vuilleumier, G. Zacek, and V. Zacek. A Search for Neutrino Oscillations by Measurement of the $\bar{\nu}_e$ Spectra at Two Distances From a Nuclear Reactor. *Phys. Lett. B*, 138:449–453, 1984. 25

[44] G. Zacek et al. Neutrino Oscillation Experiments at the Gosgen Nuclear Power Reactor. *Phys. Rev. D*, 34:2621–2636, 1986. 25

[45] A. I. Afonin, A. A. Borovoi, Yu. L. Dobrynin, S. N. Ketov, V. I. Kopeikin, L. A. Mikaelyan, M. D. Skorokhvatov, S. V. Tolokonnikov, and A. N. Kheruvimov. NEUTRINO EXPERIMENT IN THE REACTOR OF THE ROVNO ATOMIC POWER PLANT: CROSS-SECTION FOR INVERSE BETA DECAY. *JETP Lett.*, 41:435–438, 1985. 25

[46] A. I. Afonin et al. $\bar{\nu}_e$ Spectra at Two Distances From the Reactor of the Rovno Nuclear Power Plant: Search for Oscillations. *JETP Lett.*, 45:247–251, 1987. 25

[47] A. A. Kuvshinnikov, L. A. Mikaelyan, S. V. Nikolaev, M. D. Skorokhvatov, and A. V. Etenko. Measuring the anti-electron-neutrino + p —> n + e+ cross-section and beta decay axial constant in a new experiment at Rovno NPP reactor. (In Russian). *Yad. Fiz.*, 52:472–479, 1990. 25

[48] G. S. Vidyakin et al. Limitations on the characteristics of neutrino oscillations. *JETP Lett.*, 59:390–393, 1994. 25

[49] K. S. Hirata et al. Experimental Study of the Atmospheric Neutrino Flux. *Phys. Lett. B*, 205:416, 1988. 25

[50] S. Hatakeyama et al. Measurement of the flux and zenith angle distribution of upward through going muons in Kamiokande II + III. *Phys. Rev. Lett.*, 81:2016–2019, 1998. 25

[51] M. Apollonio et al. Initial results from the CHOOZ long baseline reactor neutrino oscillation experiment. *Phys. Lett. B*, 420:397–404, 1998. 25

[52] M. Apollonio et al. Limits on neutrino oscillations from the CHOOZ experiment. *Phys. Lett. B*, 466:415–430, 1999. 25

[53] M. Apollonio et al. Search for neutrino oscillations on a long baseline at the CHOOZ nuclear power station. *Eur. Phys. J. C*, 27:331–374, 2003. 25

[54] F. Boehm et al. Final results from the Palo Verde neutrino oscillation experiment. *Phys. Rev. D*, 64:112001, 2001. 25

[55] F. Boehm et al. Search for neutrino oscillations at the Palo Verde nuclear reactors. *Phys. Rev. Lett.*, 84:3764–3767, 2000. 25

[56] F. Boehm et al. Results from the Palo Verde neutrino oscillation experiment. *Phys. Rev. D*, 62:072002, 2000. 25

[57] K. Eguchi et al. First results from KamLAND: Evidence for reactor anti-neutrino disappearance. *Phys. Rev. Lett.*, 90:021802, 2003. 26

[58] Feng Peng An et al. Improved Measurement of the Reactor Antineutrino Flux and Spectrum at Daya Bay. *Chin. Phys. C*, 41(1):013002, 2017. 26, 27, 29

[59] Y. Abe et al. Improved measurements of the neutrino mixing angle θ_{13} with the Double Chooz detector. *JHEP*, 10:086, 2014. [Erratum: JHEP 02, 074 (2015)]. 26, 27, 30

[60] Soo-Bong Kim. Measurement of neutrino mixing angle Θ_{13} and mass difference Δm^2_{ee} from reactor antineutrino disappearance in the RENO experiment. *Nucl. Phys. B*, 908:94–115, 2016. 26, 27, 30

[61] G. Mention, M. Fechner, Th. Lasserre, Th. A. Mueller, D. Lhuillier, M. Cribier, and A. Letourneau. The Reactor Antineutrino Anomaly. *Phys. Rev. D*, 83:073006, 2011. 27, 28

[62] A. Aguilar et al. Evidence for neutrino oscillations from the observation of $\bar{\nu}_e$ appearance in a $\bar{\nu}_\mu$ beam. *Phys. Rev. D*, 64:112007, 2001. 27

[63] A. A. Aguilar-Arevalo et al. A Search for Electron Neutrino Appearance at the $\Delta m^2 \sim 1eV^2$ Scale. *Phys. Rev. Lett.*, 98:231801, 2007. 27

[64] W. Hampel et al. Final results of the Cr-51 neutrino source experiments in GALLEX. *Phys. Lett. B*, 420:114–126, 1998. 27

[65] J. N. Abdurashitov et al. Measurement of the response of a Ga solar neutrino experiment to neutrinos from an Ar-37 source. *Phys. Rev. C*, 73:045805, 2006. 27

[66] F. P. An et al. Evolution of the Reactor Antineutrino Flux and Spectrum at Daya Bay. *Phys. Rev. Lett.*, 118(25):251801, 2017. 27

[67] G. Bak et al. Fuel-composition dependent reactor antineutrino yield at RENO. *Phys. Rev. Lett.*, 122(23):232501, 2019. 27

[68] I Alekseev et al. Search for sterile neutrinos at the DANSS experiment. *Phys. Lett. B*, 787:56–63, 2018. 32, 126

[69] I. Alekseev et al. DANSS: Detector of the reactor AntiNeutrino based on Solid Scintillator. *JINST*, 11(11):P11011, 2016. 32

[70] Y. J. Ko et al. Sterile Neutrino Search at the NEOS Experiment. *Phys. Rev. Lett.*, 118(12):121802, 2017. 32, 126

[71] A. P. Serebrov et al. NEUTRINO4 experiment: preparations for search for sterile neutrino at 100 MW Reactor SM-3 at 6-12 Meters. 5 2012. 32

[72] A. P. Serebrov. Experiment NEUTRINO-4 Search for Sterile Neutrino. In *3rd Large Hadron Collider Physics Conference*, pages 748–753, Gatchina, 2016. Kurchatov Institute. 32

[73] Andi S. Cucoanes. Status of the Nucifer experiment. *J. Phys. Conf. Ser.*, 375:042063, 2012. 32

[74] G. Boireau et al. Online Monitoring of the Osiris Reactor with the Nucifer Neutrino Detector. *Phys. Rev. D*, 93(11):112006, 2016. 32

[75] J. Ashenfelter et al. The PROSPECT Physics Program. *J. Phys. G*, 43(11):113001, 2016. 32

[76] J. Ashenfelter et al. The PROSPECT Reactor Antineutrino Experiment. *Nucl. Instrum. Meth. A*, 922:287–309, 2019. 32, 33, 34, 36, 38, 44, 46, 49, 51, 86, 88

[77] Luis Manzanillas. STEREO: Search for sterile neutrinos at the ILL. *PoS*, NOW2016:033, 2017. 32

[78] Y. Abreu et al. A novel segmented-scintillator antineutrino detector. *JINST*, 12(04):P04024, 2017. 32

[79] Y. Abreu et al. Performance of a full scale prototype detector at the BR2 reactor for the SoLid experiment. *JINST*, 13(05):P05005, 2018. 32

[80] J. Ashenfelter et al. Background Radiation Measurements at High Power Research Reactors. *Nucl. Instrum. Meth. A*, 806:401–419, 2016. 35

[81] Blaine Alexander Heffron. *Neutrino Physics at a Research Reactor: Backgrounds and Analysis*. Phd dissertation, University of Tennessee, June 2023. 35

[82] J. Ashenfelter et al. Lithium-loaded Liquid Scintillator Production for the PROSPECT experiment. *JINST*, 14(03):P03026, 2019. 35, 37, 39

[83] Ej-309. *https://eljentechnology.com/products/liquid-scintillators/ej-301-ej-309*. 37

[84] J. Ashenfelter et al. Performance of a segmented ^{6}Li-loaded liquid scintillator detector for the PROSPECT experiment. *JINST*, 13(06):P06023, 2018. 38, 40

[85] Weber, Stover, Gilbert, Nevitt, and Ouderkirk. Giant birefringent optics in multilayer polymer mirrors. *Science*, 287 5462:2451–6, 2000. 38

[86] J. Ashenfelter et al. A Low Mass Optical Grid for the PROSPECT Reactor Antineutrino Detector. *JINST*, 14(04):P04014, 2019. 41, 43

[87] arduino micro-controller. *https://www.arduino.cc/*. 45

[88] J. Ashenfelter et al. The radioactive source calibration system of the PROSPECT reactor antineutrino detector. *Nucl. Instrum. Meth. A*, 944:162465, 2019. 47, 49

[89] Caen v1725. *https://www.caen.it/products/v1725/*. 50

[90] 757 nim logic fan-in/fan-out. *http://www.phillipsscientific.com/pdf/757ds.pdf*. 50

[91] Internal analysis. *https://docdb.wlab.yale.edu/prospect/ShowDocument?docid=3492*. 51

[92] M. Andriamirado et al. Improved short-baseline neutrino oscillation search and energy spectrum measurement with the PROSPECT experiment at HFIR. *Phys. Rev. D*, 103(3):032001, 2021. 59, 65, 66, 68, 73, 78, 79, 81, 103, 109, 110, 111, 112, 114, 115, 116, 117, 118, 123, 141, 143, 149

[93] J. B. Birks. Scintillations from Organic Crystals: Specific Fluorescence and Relative Response to Different Radiations. *Proc. Phys. Soc. A*, 64:874–877, 1951. 61, 141

[94] C. Aberle, C. Buck, F. X. Hartmann, S. Schonert, and S. Wagner. Light output of Double Chooz scintillators for low energy electrons. *JINST*, 6:P11006, 2011. 61

[95] C. N. Chou. The Nature of the Saturation Effect of Fluorescent Scintillators. *Phys. Rev.*, 87(5):904–905, 1952. 61

[96] G. T. Wright. Scintillation response of organic phosphors. *Phys. Rev.*, 91:1282–1283, Sep 1953. 61

[97] Voltz, R. and Laustriat, G. *J. Phys. France*, (2). 61

[98] P. A. Cherenkov. Visible luminescence of pure liquids under the influence of γ-radiation. *Dokl. Akad. Nauk SSSR*, 2(8):451–454, 1934. 61

[99] Prospect2x analysis. *https://github.com/PROSPECT-collaboration/PROSPECT2x_Analysis*. 62

[100] Internal analysis 2314. *https://docdb.wlab.yale.edu/prospect/ShowDocument?docid=2314*. 66, 70

[101] Internal analysis 2254. *https://docdb.wlab.yale.edu/prospect/ShowDocument?docid=2254*. 68

[102] X Zhang. Energy Scale Study for PROSPECT's Measurement of the Antineutrino Spectrum of 235U. *ProQuest Dissertations and Theses*, page 176, 2019. 72, 140

[103] Olga Kyzylova. *Characterization of Time-Varying Backgrounds in the PROSPECT Experiment*. Phd dissertation, Drexel University, March 2021. 98

[104] A. B. Balantekin et al. Nonfuel antineutrino contributions in the ORNL High Flux Isotope Reactor (HFIR). *Phys. Rev. C*, 101(5):054605, 2020. 108

[105] X. Qian, A. Tan, J. J. Ling, Y. Nakajima, and C. Zhang. The Gaussian CL_s method for searches of new physics. *Nucl. Instrum. Meth. A*, 827:63–78, 2016. 113

[106] Gary J. Feldman and Robert D. Cousins. A Unified approach to the classical statistical analysis of small signals. *Phys. Rev. D*, 57:3873–3889, 1998. 113

[107] B. C. Rasco et al. *Decays of the Three Top Contributors to the Reactor $V^{-}e$ High-Energy Spectrum, 92Rb, 96gsY, and 142Cs, Studied with Total Absorption Spectroscopy*, pages 423–424. 2017. 117

[108] L. Hayen, J. Kostensalo, N. Severijns, and J. Suhonen. First-forbidden transitions in the reactor anomaly. *Phys. Rev. C*, 100(5):054323, 2019. 117

[109] H. Almazán et al. Improved sterile neutrino constraints from the STEREO experiment with 179 days of reactor-on data. *Phys. Rev. D*, 102(5):052002, 2020. 117, 126

[110] M. Estienne et al. Updated Summation Model: An Improved Agreement with the Daya Bay Antineutrino Fluxes. *Phys. Rev. Lett.*, 123(2):022502, 2019. 117

[111] V. Kopeikin, M. Skorokhvatov, and O. Titov. Reevaluating reactor antineutrino spectra with new measurements of the ratio between U235 and Pu239 β spectra. *Phys. Rev. D*, 104(7):L071301, 2021. 117

[112] C. Giunti, Y. F. Li, C. A. Ternes, and Z. Xin. Reactor antineutrino anomaly in light of recent flux model refinements. *Phys. Lett. B*, 829:137054, 2022. 117

[113] A. P. Serebrov et al. Search for sterile neutrinos with the Neutrino-4 experiment and measurement results. *Phys. Rev. D*, 104(3):032003, 2021. 117

[114] C. Giunti, Y. F. Li, C. A. Ternes, and Y. Y. Zhang. Neutrino-4 anomaly: oscillations or fluctuations? *Phys. Lett. B*, 816:136214, 2021. 117, 125

[115] M. Andriamirado et al. Final Measurement of the U235 Antineutrino Energy Spectrum with the PROSPECT-I Detector at HFIR. 12 2022. 119

[116] Diego Venegas Vargas. *Expected 2024*. Phd dissertation, University of Tennessee, 2024. 119

[117] M. Andriamirado et al. PROSPECT-II physics opportunities. *J. Phys. G*, 49(7):070501, 2022. 124, 126, 127, 128, 131, 132, 158

[118] A. P. Serebrov et al. First Observation of the Oscillation Effect in the Neutrino-4 Experiment on the Search for the Sterile Neutrino. *Pisma Zh. Eksp. Teor. Fiz.*, 109(4):209–218, 2019. 125, 126

[119] A. P. Serebrov and R. M. Samoilov. A Comment on the note arXiv:2006.13147 on arXiv:2005.05301, "Preparation of the Neutrino-4 experiment on search for sterile neutrino and the obtained results of measurements". 6 2020. 125

[120] F. P. An et al. Search for a Light Sterile Neutrino at Daya Bay. *Phys. Rev. Lett.*, 113:141802, 2014. 125, 127

[121] M. Aker et al. Bound on 3+1 Active-Sterile Neutrino Mixing from the First Four-Week Science Run of KATRIN. *Phys. Rev. Lett.*, 126(9):091803, 2021. 125, 127

[122] Debajyoti Dutta, Raj Gandhi, Boris Kayser, Mehedi Masud, and Suprabh Prakash. Capabilities of long-baseline experiments in the presence of a sterile neutrino. *JHEP*, 11:122, 2016. 125, 127

[123] H. Almazán et al. Accurate Measurement of the Electron Antineutrino Yield of ^{235}U Fissions from the STEREO Experiment with 119 Days of Reactor-On Data. *Phys. Rev. Lett.*, 125(20):201801, 2020. 129

[124] Adam Bernstein, Nathaniel Bowden, Bethany L. Goldblum, Patrick Huber, Igor Jovanovic, and John Mattingly. *Colloquium*: Neutrino detectors as tools for nuclear security. *Rev. Mod. Phys.*, 92:011003, 2020. 135

[125] D. Horn, G. C. Ball, A. Galindo-Uribarri, E. Hagberg, R. B. Walker, R. Laforest, and J. Pouliot. The Mass dependence of CsI(Tl) scintillation response to heavy ions. *Nucl. Instrum. Meth. A*, 320:273–276, 1992. 135

[126] S. Agostinelli et al. GEANT4–a simulation toolkit. *Nucl. Instrum. Meth. A*, 506:250–303, 2003. 136

[127] N. D. Gagunashvili. Comparison of weighted and unweighted histograms. *PoS*, ACAT:054, 2007. 143

[128] Api 120 dt generator. *https://www.thermofisher.com/order/catalog/product/151762A#/151762A*. 163, 164

[129] Iaea radiation technology reports series no. 1. *https://www-pub.iaea.org/MTCD/Publications/PDF/P1535_web.pdf*. 165

[130] J. Iwanowska, L. Swiderski, T. Krakowski, M. Moszynski, T. Szczesniak, and G. Pausch. The time-of-flight method for characterizing the neutron response

of liquid organic scintillators. *Nuclear Instruments and Methods in Physics Research Section A: Accelerators, Spectrometers, Detectors and Associated Equipment*, 781:44–49, 2015. 166

[131] G. Bruno. Light output response of the LVD liquid scintillator to neutron-induced nuclear recoils. *JINST*, 8:T05004, 2013. 170

[132] V. I. Tretyak. Semi-empirical calculation of quenching factors for scintillators: new results. *EPJ Web Conf.*, 65:02002, 2014. 170

Vita

Xiaobin Lu was born in Shangyu, Zhejiang Province, China. He completed his high school education in Chunhui High School, and entered Zhejiang University in Zhejiang Province to continue his undergraduate study in Physics. After obtaining his degree of Bachelor of Science in June 2012, he devoted his efforts in education industry in Qiyang Education. After several years work experience in education, he continued his graduate study at the Graduate School of The University of Tennessee, Knoxville in September, 2016.